České vysoké učení technické v Praze
Fakulta jaderná a fyzikálně inženýrská

Katedra fyziky
Obor: Experimentální jaderná a částicová fyzika

Studium rovnováhy půvabných mezonů v relativistických srážkách těžkých iontů pomocí Monte Carlo generátoru HYDJET++

DIPLOMOVÁ PRÁCE

Autor:	Bc. Jaroslav Štorek
Vedoucí:	prof. Larissa Bravina
	doc. Mgr. Jaroslav Bielčík, Ph.D.
Rok:	2021

Czech Technical University in Prague
Faculty of Nuclear Sciences and Physical Engineering

Physics Department

Branch: Experimental Nuclear and Particle Physics

Study of equilibration of charm mesons in relativistic heavy ion collisions within Monte Carlo generator HYDJET++

MASTER'S THESIS

Author: Bc. Jaroslav Štorek

Supervisor: Prof. Larissa Bravina

                Assoc. Prof. Jaroslav Bielčík

Year: 2021

Katedra: fyziky   *Akademický rok:*   2020/2021

ZADÁNÍ DIPLOMOVÉ PRÁCE

Student: Bc. Jaroslav Štorek

Studijní program: Aplikace přírodních věd

Obor: Experimentální jaderná a částicová fyzika

Název práce:
(česky)   Studium rovnováhy půvabných mezonů v relativistických srážkách těžkých iontů pomocí Monte Carlo generátoru HYDJET++

Název práce:
(anglicky)   Study of equilibration of charm mesons in relativistic heavy ion collisions within Monte Carlo generator HYDJET++

Pokyny pro vypracování:

1) Fázový diagram jaderné hmoty
2) HYDJET++ model
3) Simulace Au+Au a Pb+Pb srážek pomocí HYDJET++ modelu
4) Vyčíslení nasimulovaných výtěžků částic
5) Porovnání výsledků simulací s experimentálními daty
6) Diskuse výsledků a shrnutí

Doporučená literatura:

[1] B. I. Abelev, et al. (STAR Collaboration): Systematic measurements of identifed particle spectra in pp, d+Au and Au+Au collisions from STAR, Phys. Rev. C 79, 034909 (2009)

[2] M. Bleicher, el al.: Relativistic Hadron-Hadron Collisions in the Ultra-Relativistic Quantum Molecular Dynamics Model, J. Phys. G25 1859-1896 (1999)

[3] N. Xu: Exploration of the QCD Phase Diagram at Finite Baryon Density Region: Recent Results from RHIC Beam Energy Scan-I, Springer Proc.Phys. 203 (2018) 1-5

[4] I. P. Lokhtin, et al.: HYDJET++ heavy ion event generator and its applications for RHIC and LHC, PoS(High-pT physics09)023, 2009

Jméno a pracoviště vedoucího diplomové práce:

doc. Mgr. Jaroslav Bielčík, Ph. D.

Katedra fyziky, Fakulta jaderná a fyzikálně inženýrská ČVUT v Praze

prof. Larissa Bravina (University of Oslo)

Datum zadání diplomové práce: 23.10.2020

Termín odevzdání diplomové práce: 03.05.2021

Doba platnosti zadání je dva roky od data zadání.

....
garant oboru

....
vedoucí katedry

....
děkan

V Praze dne   23.10.2020

Prohlášení

Prohlašuji, že jsem svou diplomovou práci vypracoval samostatně a použil jsem pouze podklady (literaturu, projekty, SW atd.) uvedené v přiloženém seznamu.

Nemám závažný důvod proti použití tohoto školního díla ve smyslu § 60 Zákona č. 121/2000 Sb., o právu autorském, o právech souvisejících s právem autorským a o změně některých zákonů (autorský zákon).

V Praze dne ....
                                                          Bc. Jaroslav Štorek

Acknowledgement

Název práce:

Studium rovnováhy půvabných mezonů v relativistických srážkách těžkých iontů pomocí Monte Carlo generátoru HYDJET++

Autor:	Bc. Jaroslav Štorek

Studijní program:	Aplikace přírodních věd
Obor:	Experimentální jaderná a částicová fyzika
Druh práce:	Diplomová práce

Vedoucí práce:	prof. Larissa Bravina, katedra fyziky, Fakulta matematiky a přírodních věd, Univerzita v Oslo
	doc. Mgr. Jaroslav Bielčík, Ph.D., katedra fyziky, Fakulta jaderná a fyzikálně inženýrská, České vysoké učení technické v Praze

Abstrakt: Ve srážkách ultrarelativisticých těžkých iontů vzniká kvark-gluonové plazma (QGP), stav hmoty, ve kterém kvarky a gluony nejsou vázány do hadronů. Simulacemi takových srážek pomocí např. HYDJET++ Monte Carlo generátoru můžeme lépe porozumět vlastnostem QGP. V této práci jsou popsány základy jádro-jaderných srážek a pomocí modelu HYDJET++ verze 2.4 byla nasimulována produkce nabitých a půvabných částic ve srážkách Pb+Pb při energiích $\sqrt{s_{\mathrm{NN}}} = 2.76$ a 5.02 TeV a srážkách Au+Au při $\sqrt{s_{\mathrm{NN}}} = 200$ GeV. Simulované výtěžky částic a jejich kolektivní tok jsou porovnány s experimentálními daty a ze srovnání vyplývá, že model dobře popisuje data v nejcentrálnějších srážkách napříč energiemi. Výsledky ukazují, že teplota kinetického vymrznutí D mesonů se při zvýšení energie srážky z $\sqrt{s_{\mathrm{NN}}} = 200$ GeV na 2.76 TeV a 5.02 TeV sníží z $T_{th} = 165$ MeV na $T_{th} = 105$ MeV. $T_{th} = 105$ MeV je shodná pro energie $\sqrt{s_{\mathrm{NN}}} = 2.76$ a 5.02 TeV.

Klíčová slova:	Srážky těžkých iontů, půvabné mezony, kvark-gluonové plazma, HYDJET++

Title:

Study of equilibration of charm mesons in relativistic heavy ion collisions within Monte Carlo generator HYDJET++

Author:	Bc. Jaroslav Štorek

Abstract: In ultra-relativistic collisions of heavy nuclei, medium composed of deconfined quarks and gluons, quark-gluon plasma (QGP), can be created. Reproducing experimental results by the HYDJET++ Monte Carlo event generator can help scientific community to better understand properties of QGP and nature of the underlying processes. In the thesis, basics of nuclei collisions are introduced and simulations of charged and charm particles with HYDJET++ model version 2.4 in Pb+Pb collisions at $\sqrt{s_{\mathrm{NN}}} = 2.76$ and 5.02 TeV and in Au+Au collisions at $\sqrt{s_{\mathrm{NN}}} = 200$ GeV energies are presented. Simulated particle yields and collective flow coefficients are compared to the experimental data and a good agreement between the simulations and the data is observed in the most central collisions at all studied energies. The results show that the thermal freeze-out temperature of D mesons decreases from $T_{th} = 165$ MeV in Au+Au at $\sqrt{s_{\mathrm{NN}}} = 200$ GeV to $T_{th} = 105$ MeV in Pb+Pb at $\sqrt{s_{\mathrm{NN}}} = 2.76$ and 5.02 TeV.

Key words:	Heavy-ion collisions, charm mesons, quark-gluon plasma, HYDJET++

Contents

Introduction

The Standard Model is one of the most successful particle physics theories. According to the Standard Model, the world around us is made from elementary particles which interact between each other by fundamental interactions. Atomic nuclei can be recognized to consist of protons and neutrons which are found to be made of quarks. Force that holds quarks together is strong interaction and its mediators are called gluons. However, right after the Big Bang, temperature of all the matter was too high for strong interaction to hold quarks together. It is believed that the matter was in the so called quark-gluon plasma (QGP) state of quasi-free quarks and gluons. Nowadays, such conditions of matter with high energy densities can be reproduced in particle colliders by colliding heavy ions at ultra-relativistic energies. Understanding of the QGP behavior allows one to model evolution of the early Universe and currently it is a field of very intense theoretical and experimental studies.

Many models try to explain what happens with the matter in such extreme conditions and predict outcome of the experiment. Match between the model and experimental data may indicate that the main physical processes have been correctly understood. One of such models is HYDJET++ which combines blast wave model used for low transverse momentum particles with PYTHIA 6.4 generated modified jet events which are applied in high transverse momentum region. An interesting feature of this model based on basic assumptions is possibility to disentangle contributions of different effects into the final distributions. In this thesis, HYDJET++ simulated distributions of charged and charm particles are compared to the experimental data in three different collision setups and conclusions of the particle specie thermalization are made.

In the beginning of the thesis, nuclear matter phase diagram and time evolution of the ultra-relativistic heavy ion collisions are explained. Next, several QGP signatures are introduced. The main part of the thesis is dedicated to HYDJET++ model and simulation results of Au+Au collisions at $\sqrt{s_{\mathrm{NN}}} = 200$ GeV and Pb+Pb collisions at $\sqrt{s_{\mathrm{NN}}} = 2.76$ and 5.02 TeV. Finally, relevant observations are summarized in the conclusion.

Chapter 1

Ultra-relativistic Nucleus-nucleus Collisions

Nuclei are composed of protons and neutrons which consist of elementary particles, quarks. The Standard Model describes the behavior of elementary particles interacting through three fundamental forces between each other. All the elementary particles and force carriers can be seen in Fig. 1.1. Boxes in the scheme distinguish groups of particles which interact by the particular force. The Standard Model interactions are governed by charges. Overview of all interactions[1] and their relative strength is summarized in Tab. 1.1. As can be seen from the scheme, quarks can interact via all the forces. No other particles except of the strong force mediators can interact by the strong force.

Theory of the strong interaction, quantum chromodynamics (QCD), has got its origin in the 1970s [2]. Interaction of color charged quarks is described by interchange of color charged gluons. Important feature of QCD is that the color charged gluons can interact between each other. Quarks and gluons (altogether called partons) are under normal conditions bound into colorless hadrons. However, at early times of the Universe the energy density of partons was too high to form bound states such as protons or neutrons [3]. To study systems of deconfined nuclear matter and get better understanding of QCD theory, high energy density needs to be reached. One of the ways how to achieve such conditions are heavy ion collisions at relativistic energies.

Interaction	Force carrier	Source	Range [m]	Relative strength
strong	g	color charge	$\leq 10^{-15}$	1
electromagnetic	γ	electric charge	∞	10^{-2}
weak	$W^{\pm}$, Z^0	weak charge	10^{-18}	10^{-7}
gravitational	graviton	mass	∞	10^{-39}

Table 1.1: Summary of four interactions and their properties [4].

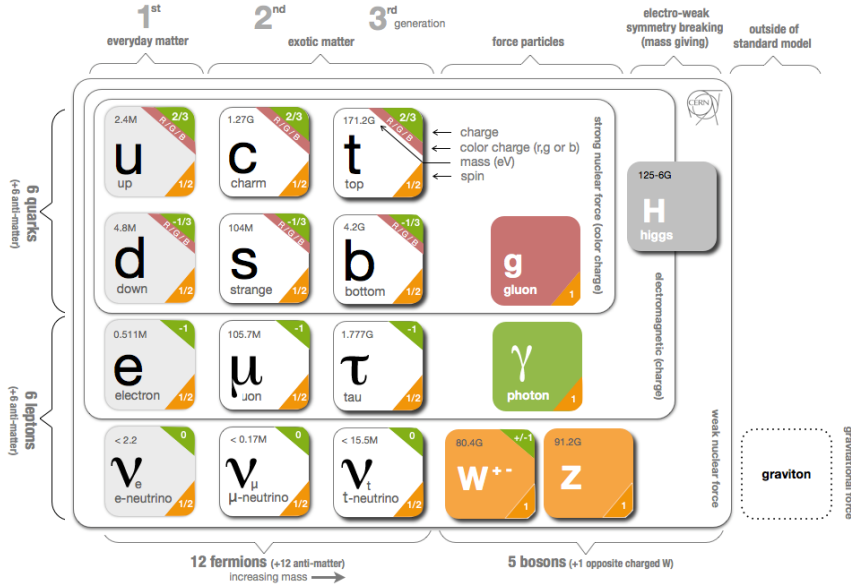[1]Note that gravity is not part of the Standard Model.

Figure 1.1: Standard model scheme [1].

1.1 Nuclear Matter Phase Diagram

One of the key tasks of heavy ion physics research is to investigate nuclear matter phase diagram. It is known from lattice QCD calculations that the nuclear matter can exist in deconfined phase which implies a phase transition between confined and deconfined phase occurring at a critical temperature T_c. This critical temperature has been computed even before establishment of QCD by Hagedorn who estimated "boiling point of hadronic matter" at vicinity of $T_c = 160$ MeV [5]. Later lattice QCD calculations yielding $T_c = (156.5 \pm 1.5)$ MeV agree with this result [6] and it has become a great experimental challenge to confront these predictions with reality. Note that both mentioned predictions are based on vanishing net baryon density assumption where number of baryons is equal to number of antibaryons.

Schematic picture of QCD phase diagram in terms of temperature T and chemical baryon potential[2] μ_B can be seen in Fig. 1.2. Baryon chemical potential μ_B corresponds to net baryon number density, i.e. difference between baryons and antibaryons, and it is lowest for early universe conditions as well as in ultra-relativistic heavy ion collisions. The critical temperature mentioned above is labeled here at $T_c = 155$ MeV and is calculated for zero baryon chemical potential $\mu_B = 0$. At this point, white curve denoting phase transition from quark-gluon plasma (QGP), state of deconfined matter, where quarks and gluons are not bound into hadrons and can freely move within the medium, to hadron gas[3] begins and continues along

---

[2]Baryon chemical potential is in thermodynamics defined as change in initial energy U when number of baryons N_B is changed while entropy S and volume V remain constant $\mu_B = \frac{\partial U}{\partial N_B}\big|_{S,V}$ [7].

[3]There is a sharp change in degrees of freedom at phase boundary between quark-gluon plasma
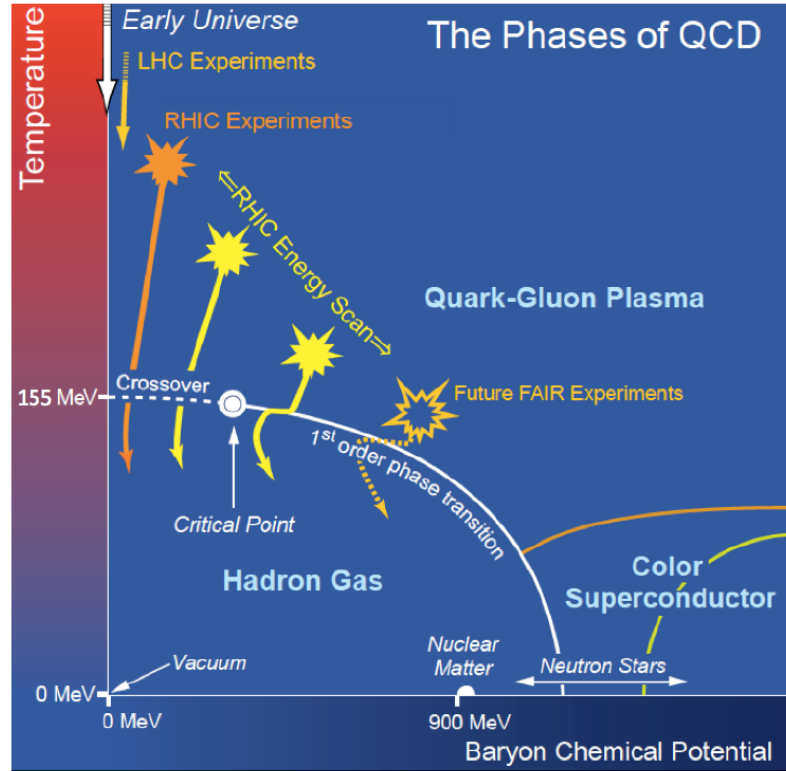
Figure 1.2: A sketch illustrating the experimental and theoretical exploration of the QCD phase diagram [10].

points with decreasing temperature and increasing μ_B. Following the white phase transition curve, two distinct regions can be distinguished split by a critical point: crossover and the first order phase transition. Critical point is location in a phase diagram where the boundary between the phases disappears. At the first order phase transition phases coexist together while at the crossover region there is smooth change of phases [8]. The location of the critical point has been narrowed down to $T_{cp} < 135 - 140$ MeV and $\mu_B^{cp} > 300$ MeV by recent lattice QCD calculations [9].

Experiments focusing on phase transition line studies are also depicted in the graph. It is namely the Large Hadron Collider (LHC) at CERN[4] in Geneva, Switzerland [11], the Relativistic Heavy Ion Collider (RHIC) at the Brookhaven national laboratory in New York, USA [12], and the Facility for Antiproton and Ion Research in Europe (FAIR) at Darmstadt, Germany [13]. One can see that with increasing energy of an experiment smaller μ_B and higher T points of the graph are covered. The LHC is the most powerful machine and can reach center of mass energies up to $\sqrt{s_{\mathrm{NN}}} = 5.02$ TeV in Pb+Pb collisions[5]. Net baryon densities close to zero can also be achieved in Au+Au collisions at $\sqrt{s_{\mathrm{NN}}} = 200$ GeV energies at RHIC. An important feature of RHIC is that energies down to $\sqrt{s_{\mathrm{NN}}} = 7$ GeV can be studied where critical point of the nuclear matter is expected to be located. High net baryon densities are about to be investigated by the Compressed Baryonic Matter (CBM) experiment at FAIR

---

and hadron gas. Phase is a region with particular number of degrees of freedom.

[4]CERN is an abbreviation of European Center for Particle Physics.

[5]$\sqrt{s_{\mathrm{NN}}}$ is center-of-mass energy per nucleon pair.

in gold beams collisions on a fixed target at energies up to $\sqrt{s_{\mathrm{NN}}} = 4.9$ GeV [14].

To intuitively understand two points of the phase diagram – phase transition along temperature axis ($\mu_B = 0$) and along chemical potential axis ($T = 0$) –, the MIT bag model described in the next section can be used.

1.1.1   MIT Bag Model

The Bag Model developed at MIT (Massachusetts Institute of Technology) is a simple model describing a hadron as a bag confining non-interacting quarks in it [15]. It provides a good theoretical example which illustrates the possibility of a transition from hadron gas to quark-gluon plasma.

In this model, quarks are held in a hadron by the bag pressure B. B points inwards to the center of the hadron and compensates pressure of quarks caused by their kinetic motion. The value of the bag pressure $B^{\frac{1}{4}}$ for the confinement radius 0.8 fm and a 3 quark system in a baryon is equal to $B^{\frac{1}{4}} = 206$ MeV [16]. If pressure caused by kinetic motion overwhelms B, quarks expand and are no longer confined inside the bag. Thanks to this intuitive thermodynamic model it is easy to imagine, how this pressure excess can happen: either pressure of partons is too high (corresponds to high temperature) or too many partons try to fit in a very small area (large baryon number density).

In high temperature regime, let noninteracting and massless quarks and gluons be in thermal equilibrium at large temperature T in volume V and assume an equal number of quarks and antiquarks, so the net baryon density and the baryon chemical potential are equal to zero, $\mu_B = 0$. From sum of pressures of quarks, antiquarks and gluons, critical temperature T_c, at which outward pointing pressure P equals the bag pressure B, can be inferred. Pressure $B = P$ can be expressed as [16]

$$B = P = g\frac{\pi^2}{90}T_c^4, \tag{1.1}$$

where $g = 37$ is number of degrees of freedom considering only two quark flavors. For $B^{\frac{1}{4}} = 206$ MeV T_c yields 144 MeV [16]. Temperatures of the medium exceeding T_c cause breaking of the bag and quarks and gluons are deconfined in the state of quark-gluon plasma.

The bag pressure can be exceeded also by high baryon density in the bag. To avoid thermal contribution, $T = 0$ is assumed for this calculation. Pauli exclusion principle restricts filling the same states for fermions, therefore increasing the number of quarks results in occupation of different momentum states and increase of the pressure.

Critical baryon number density at bag pressure B can be expressed as [16]

$$n_{B,c} = \frac{1}{3}n_{q,c} = \frac{4}{3}\Big(\frac{g_q}{24\pi^2}\Big)^{\frac{1}{4}}B^{\frac{3}{4}} \quad , \tag{1.2}$$

where g_q is quark degeneracy factor. Inserting values $g_q = 12$ (two flavors, two spins and three colors) and $B^{\frac{1}{4}} = 206$ MeV, the critical baryon number density $n_{B,c}$, at which the compressed hadron matter becomes the quark-gluon plasma with a high baryon content at $T = 0$, equals $n_{B,c} = 0.72/\text{fm}^3$. Because this value is 3 times higher than that of the nuclear matter under normal conditions[6], this state of matter can be imagined as compressed form of regular matter.

The MIT Bag Model serves especially as a guide and helps to illustrate reasons why transition into the deconfined state of matter can happen. Prediction of the deconfinement can be extracted directly from the first principle calculations using lattice QCD techniques.

1.2 Time Evolution of Nuclear Collision

Time evolution of nuclear collision in an inelastic scattering can be seen in Fig. 1.3. Here, the z-axis represents space coordinate along the beam direction, the y-axis is time t and $\tau = \sqrt{t^2 - z^2}$ is the Lorentz invariant proper time of the collision. Using proper time τ, three different space-time areas can be recognized: space-like ($\tau < 0$), light-like ($\tau = 0$) and time-like ($\tau > 0$). Massless particles (e.g. photons) follow light-like path, while other particles fall into the time-like region. In the space-like region no particles can be found. In the figure, two possible cases of a collision time evolution are drawn. Left half ($z < 0$) describes evolution of a collision without sufficient energy density to create QGP while the right one ($z > 0$) that with QGP creation. Only the case with QGP creation will be discussed.

The collision happens at $t = \tau = 0$. Right after the collision, before the medium reaches equilibrium, interaction of strong fields of nuclei partons is assumed and can be described by Color Glass Condensate effective field theory [18]. Due to rapid interactions between constituents, the medium is assumed to reach local thermal equilibrium at proper time $\tau_0 \leq 1$ fm/c and to create quark-gluon plasma. The system collectively expands and description by relativistic hydrodynamics can be used. While expanding, medium cools down below the critical temperature for QGP formation T_c and mixed phase of QGP can be formed after which the matter takes the form of hadron gas. At chemical freeze-out temperature $T_{ch} \approx 160 - 175$ MeV [19, 20, 21], hadronization from quarks and gluons finishes. Particles do not undergo inelastic collisions anymore and particle species are set. After cooling down below kinetic (thermal) freeze-out temperature $T_{fo} \approx 90 - 130$ MeV [22], elastic interactions also stop, resonances decay and momenta of outgoing hadrons are fixed.

Evolution of the quark-gluon plasma can be successfully described by relativistic hydrodynamics explained in the next section.

---

[6]Baryon number density of the nuclear matter under normal conditions $n_B = 0.25/\text{fm}^3$ can be obtained from mean nuclear radius $R = R_0 A^{1/3}$, where $R_0 = 1.2$ fm is a constant and A is the nuclear number [17].
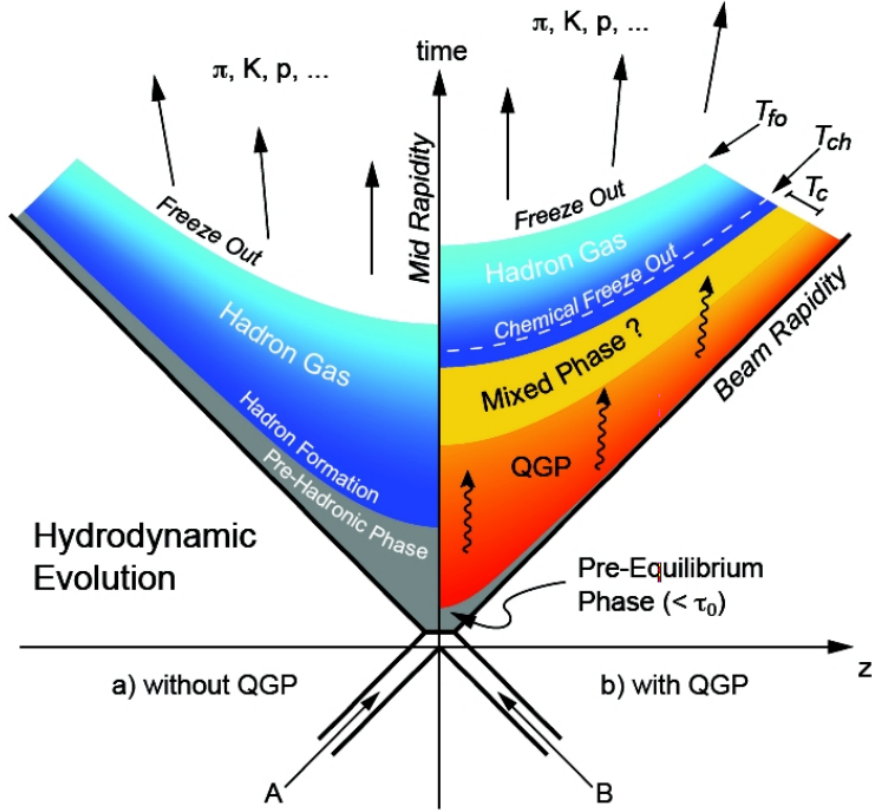
Figure 1.3: Diagram representing two possible scenarios of a collision evolution in space (z) and time coordinates without (left, $z < 0$) and with (right, $z > 0$) the QGP [23].

1.2.1 Hydrodynamics

Hydrodynamics of QGP can be described by energy density field ϵ, pressure field p, baryon charge density n and the 4-velocity field $u^\mu = dx^\mu/d\tau$ at every space time point x using energy-momentum tensor $T^{\mu\nu}$ and baryon number current N^μ [16]. Classical energy-momentum tensor is defined as [24]

$$T^{\mu\nu}(x) = \int \frac{d^3p}{E} p^\mu p^\nu f(x,p), \qquad (1.3)$$

where $f(x,p)$ is a distribution function and $p^\mu = (E, \vec{p})$ where E is energy and $\vec{p}$ is momentum vector. $T^{00}(x)$ is the energy density, $\frac{1}{c}T^{i0}$ describes i-th component of momentum density and cT^{0i} i-th component of energy flow ($i = 1, 2, 3$) where c is the speed of light [25]. Baryon number current is defined as

$$N^\mu = \int \frac{d^3p}{E} p^\mu f(x,p). \qquad (1.4)$$

The basic hydrodynamical equations are energy and momentum conservation law

$$\frac{\partial T^{\mu\nu}}{\partial x^\mu} = 0 \tag{1.5}$$

and the current conservation [26], in this case baryon number conservation,

$$\frac{\partial N^\mu}{\partial x^\mu} = 0. \tag{1.6}$$

If the particle distribution $f(x, p)$ is a known function, $T^{\mu\nu}$ and N^μ can be computed and static matter properties hydrostatic pressure p and energy density ϵ as well as transport properties viscous stress tensor $\Pi^{\mu\nu}$ and heat flow I_q^μ can be extracted using equations shown below [25]. In case of a small deviation from the static equilibrium, transport properties can be approximated by linear dependence on the flow velocity and the temperature, and shear viscosity η, bulk viscosity ζ and heat conductivity κ transport coefficients are introduced. Note that medium in relativistic heavy ion collision is not static macroscopically but microscopically. Local static equilibrium can still be achieved as the microscopic interaction are much faster than the expansion of the fluid cell.

There are two essential components entering $T^{\mu\nu}$: reversible $T^{\mu\nu\,(r)}$ component and irreversible $T^{\mu\nu\,(i)}$ component,

$$T^{\mu\nu} = T^{\mu\nu\,(r)} + T^{\mu\nu\,(i)}. \tag{1.7}$$

Reversible component applies for ideal fluid when medium is in the static equilibrium. Irreversible part is dissipative part which distorts the equilibrium. From dissipative part shear and bulk viscosity variables come out.

In special case, when fluid element is at rest[7] (marked by asterisk), reversible part of $T^{\mu\nu}$ can be expressed as $T^{*\mu\nu\,(r)} = diag(\epsilon, p, p, p)$. When the fluid element is moving with 4-velocity u^μ, $T^{\mu\nu\,(r)}$ can be obtained from $T^{*\mu\nu\,(r)}$ by the law of transformation of tensors [27]. $T^{\mu\nu\,(r)}$ is then be expressed as

$$T^{\mu\nu\,(r)} = (\epsilon + p)u^\mu u^\nu - g^{\mu\nu} p, \tag{1.8}$$

where $g^{\mu\nu} = diag(1, -1, -1, -1)$ is the Minkowski space metric tensor and $T^{\mu\nu\,(i)}$ can be expressed as [25]

$$T^{\mu\nu\,(i)} = \left(I_q^\mu + \frac{\epsilon + p}{N^\rho u_\rho} N^\sigma \Delta_\sigma^\mu\right) u^\nu + \left(I_q^\nu + \frac{\epsilon + p}{N^\rho u_\rho} N^\sigma \Delta_\sigma^\nu\right) u^\mu + \Pi^{\mu\nu}, \tag{1.9}$$

where I_q^μ is the heat flow, $N^\rho = \int \frac{d^3 p}{E} p^\rho f(x, p)$ is the particle 4-flow, $\Delta_\sigma^\mu = \delta_\sigma^\mu - \frac{u^\mu u_\sigma}{u_\sigma u^\sigma}$ where δ_σ^μ is the Kronecker delta and $\Pi^{\mu\nu}$ is the viscous stress tensor. Baryon number

---

[7]$(u^{*0}, u^{*1}, u^{*2}, u^{*3}) = (1, 0, 0, 0)$

current can also be decomposed into reversible $N^{\mu\,(r)}$ and irreversible $N^{\mu\,(i)}$ part, $N^{\mu} = N^{\mu\,(r)} + N^{\mu\,(i)}$, where

$$N^{\mu\,(r)} = nu^{\mu} \quad \text{and} \tag{1.10}$$

$$N^{\mu\,(i)} = -\frac{n}{\epsilon + p}I_q^{\mu}. \tag{1.11}$$

From relations shown above it is clear that one ends up with five equations from conservation laws and six variables - energy density ϵ, pressure p, velocity $\vec{u}$ and baryon number density n. Therefore equation of state (EoS) connecting the pressure, the energy density and the charge density has to be added to obtain unambiguous solution. Ideally, one would use EoS from lattice QCD calculations, practically ideal relativistic gas EoS for the QGP phase and resonance ideal gas EoS for the hadron phase can be used.

Assumptions of the hydrodynamic model are that the medium is in local thermal equilibrium and that the mean free path of the particles is much smaller than the typical size of the system. As a result, hydrodynamic predictions deviate from the data for transverse momenta $p_T \gtrsim 2-3$ GeV/c [8] [29]. In Fig. 1.4, comparison of (3+1)D viscous hydrodynamic model CLVis calculations to the experimental data of π^+ and D^0 particles in Au+Au collisions at $\sqrt{s_{\mathrm{NN}}} = 200$ GeV energy can be seen as an example.

As a part of any hydrodynamic simulation, initial conditions have to be taken from other models (e.g. Color Glass Condensate model [18]) or be set from physical assumptions. Finally, prescription of hadronization is needed to obtain invariant particle spectra. One can employ Cooper-Frye formula [30] or hadronic cascade model. More details of the hydrodynamic simulation procedure and the currently used methods can be found in Ref. [31].

1.3 Centrality determination

Quark-gluon plasma is studied in heavy ion collisions because they offer sufficiently high energy density after a collision. Energy density of a collision is directly proportional to the centrality of the collision. Centrality of a collision corresponds to the nuclei overlap and can be expressed in terms the impact parameter b that connects centers of the colliding nuclei as it is depicted in Fig. 1.5. Impact parameter b equals zero for a head-on collision.

In an experiment, impact parameter can not be measured and centrality of a collision is usually extracted from the number of charged particles coming out of a collision. Relationship between the impact parameter b, number of the collision participants N_{part}, centrality of the collision and the number of charged particles N_{ch} can be seen

---

[8]Defining a fourvector $p^{\mu} = (\frac{E}{c}, p_x, p_y, p_z)$, rapidity y and transverse momentum p_T are defined as $y = \frac{1}{2}\ln\left(\frac{E+p_z}{E-p_z}\right)^2$ and $p_T = \sqrt{p_x^2 + p_y^2}$ [28].
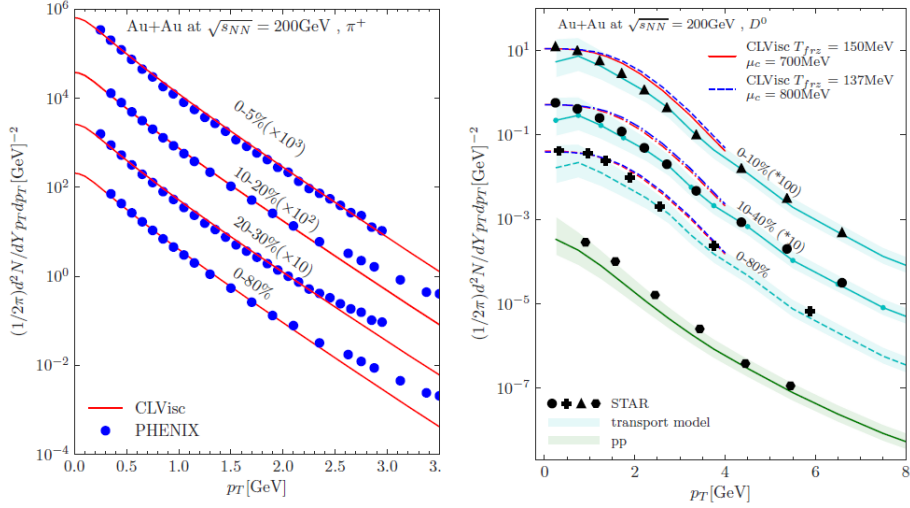
Figure 1.4: Comparison of the hydrodynamic model CLVisc calculations of p_T yield spectra of π^+ (left) and D mesons (right) to the PHENIX and STAR experimental data. Graphs have been taken from Ref. [32].

in Fig. 1.6. Central collisions feature more collision participants and more charged particles is produced than in the peripheral ones. Also, central collisions are very rare.

Determination of the impact parameter is model dependent and usually the Glauber model, which connects the number of participants to the impact parameter, is used [33]. Mapping between the experimentally measured charged particle multiplicity distribution and the Glauber calculations is needed and centrality bins are defined as a specific fractions of the total integral of the measured multiplicity distribution [34].

Central collisions refer usually to 0-10% of the most central collisions, semi-central collisions to 10-30% of the most central collisions and peripheral collisions to 30-60% of the most central collisions.
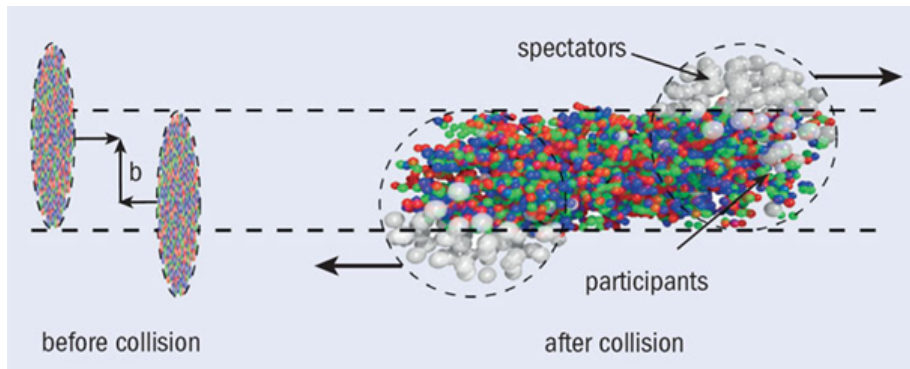
Figure 1.5: Illustration of impact parameter in a collision [35].
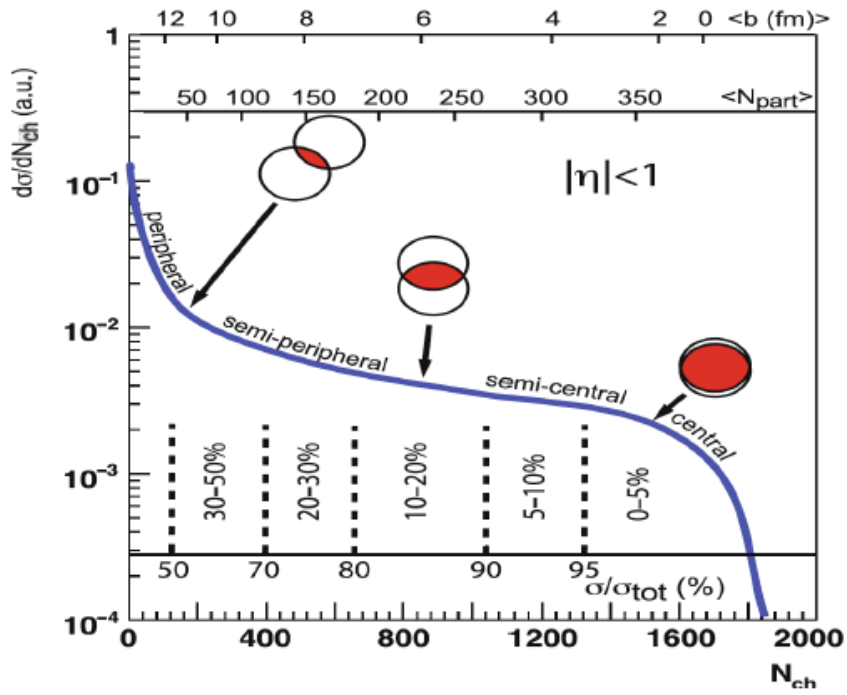
Figure 1.6: Illustrative graph of dependence of probability of type of a collision $\frac{d\sigma}{dN_{\text{ch}}}$, impact parameter b and number of participants N_{part} on the number of charged particles N_{ch} [36].

Chapter 2

QGP Signatures

In 1982 it has been proposed that enhancement of strange particle production in nuclear collisions would indicate presence of QGP [37]. It is because strange quark is created early in the collision, it is sensitive to the local color charge deconfinement and it is dependent on the gluon degree of freedom [38]. The enhancement of the strange quark production is caused by abundance of gluons which transform into the strange quarks via $g + g \rightarrow s + \bar{s}$ reaction. This phenomenon has eventually been observed in experiments conducted on Super Proton Synchrotron (SPS) and experimental results can be seen in Fig. 2.1a (open symbols) showing more pronounced enhancement for multi-strange baryons Ξ and Ω. Together with other proposed QGP signatures[1], observation of the QGP has been declared in February 2000 in CERN lead beam programme assessment [39]. The SPS results have been confirmed by RHIC results at tenfold higher energy few years later (solid markers in Fig. 2.1a). Since that time, QGP properties are under thorough investigation which continues also at LHC. In this chapter the main experimental QGP tools are discussed.

To quantify QGP effects, results from nuclei collisions are compared to p+p collisions where QGP has not been created and medium effects can be deduced. For this purpose modification factor R_{AB} is used. R_{AB} is a ratio of the yield of a particle of interest in A+B collision, N^{AB}, with respect to that in p+p collision, N^{pp}, scaled by the mean number of binary collisions $\langle N_{coll} \rangle$ and can be defined in dependence on chosen variable, usually transverse momentum p_T or number of participants N_{part}, as [44]

$$R_{AB}(p_T) = \frac{dN^{AB}/dp_T}{\langle N_{coll} \rangle dN^{pp}/dp_T} = \frac{dN^{AB}/dp_T}{T_{AB} d\sigma^{pp}/dp_T} \quad , \tag{2.1}$$

where σ^{pp} is the cross section of charged particles in p+p collisions and T_{AB} is nuclear overlap function from the Glauber model. Instead of using $\langle N_{coll} \rangle$, R_{AB} can be expressed in terms of nuclear overlap function T_{AB} and total inelastic cross section in

---

[1]Other signatures supporting the QGP creation were charmonia suppression, fireball expansion inferred from momentum distributions and from two-particle correlations and broadening of the ρ's spectral function.
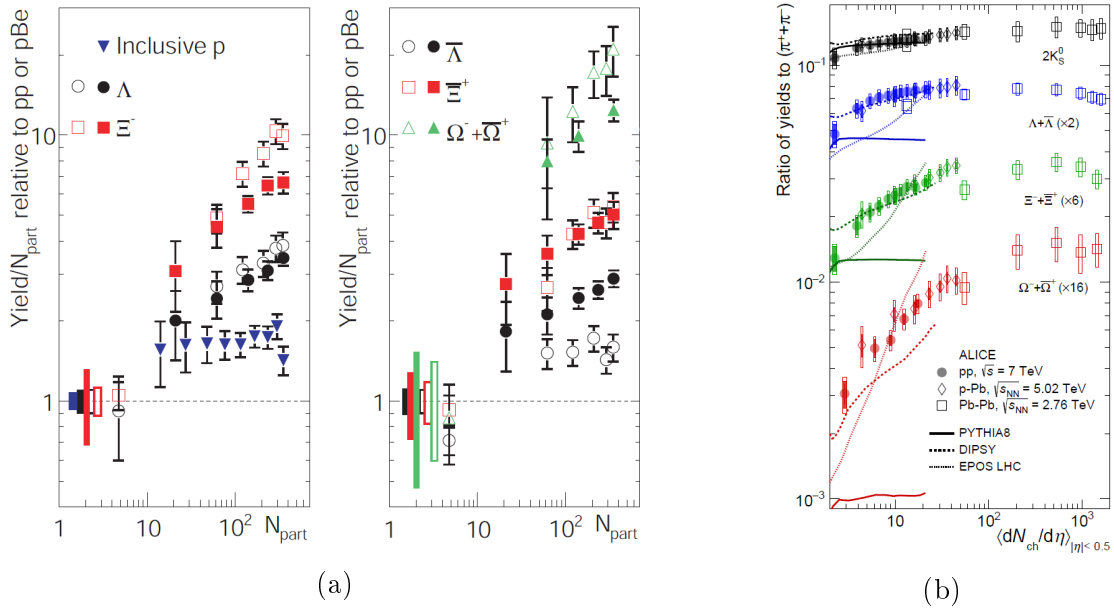
Figure 2.1: (a) Mid-rapidity yield enhancement as a function of the number of participants N_{part} for strange particles [40]. The solid markers are for Au+Au at $\sqrt{s_{NN}} = 200$ GeV and the open symbols for Pb+Pb ($|y|<0.5$) at $\sqrt{s_{NN}} = 17.3$ GeV [41, 42]. (b) ALICE experiment p_T-integrated yield ratios of different particles to pions as a function of the charged particle multiplicity density $\langle N_{part}/d\eta \rangle$ measured in $|y| < 0.5$ region [43].

p+p collision σ_{inel}^{pp}, $T_{AB} = \langle N_{coll} \rangle / \sigma_{inel}^{pp}$. Notation of A+B can represent two identical nuclei (A+A) or collision of a nucleus and a proton (p+A) or a deuteron (d+A). Example of R_{AB} dependence on transverse momentum p_T in ALICE experimental data can be seen in Fig. 2.2. Taking into account only hard processes $p_T > 4$ GeV, substantial suppression of particle production with respect to p+p collisions is observed in Pb+Pb collisions while for p+Pb collisions the data are consistent with no suppression. This allows one to study cold nuclear effects in p+Pb which are not connected to QGP.

It is important to note that effects similar to that in ion collisions have been observed also in p+p collisions at LHC which might point to QGP creation even in p+p collisions. It is for example continuous strangeness enhancement shown in Fig. 2.1b or ridge effect and collective flow effects described in following sections.

2.1 Collective Flow

Flow as a collective motion of particles produced in a collision appears to be an important effect. As the medium expands with time, momentum distribution of the outgoing particles can be studied in azimuthal angle in transverse plane. Because the flow properties depend on initial conditions of a collision, information about dynamics of the early collision system and the degree of thermalization of the medium can be extracted [46].
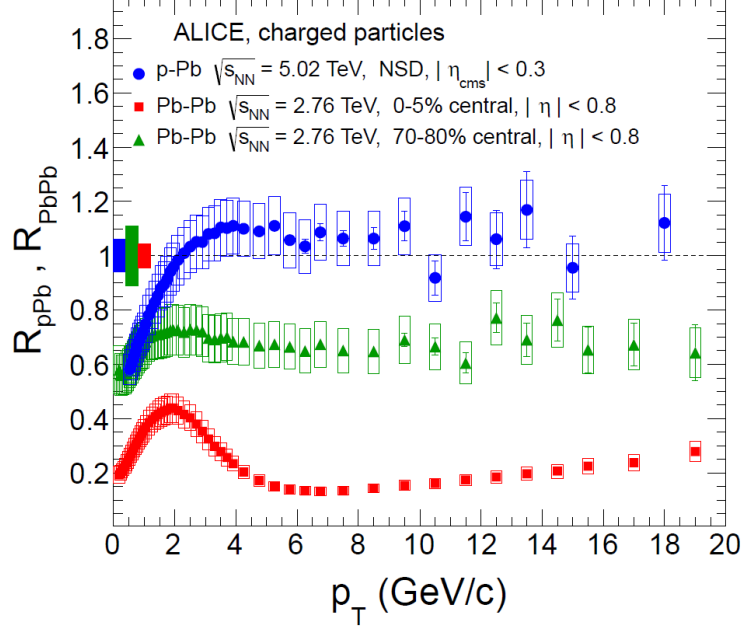
Figure 2.2: The nuclear modification factor of charged particles as a function of transverse momentum in minimum bias (NSD) p+Pb and Pb+Pb central 0-5% and peripheral 70-80% collisions at ALICE [45].

After a non-central collision, medium forms an almond-like shape in the transverse plane which results in azimuthal momentum anisotropy because of anisotropic pressure gradients. The azimuthal transverse momentum distribution $\frac{dN}{d\varphi} = r(\varphi)$ of azimuthal angle φ is a periodic function and can be expanded into a Fourier series

$$\frac{dN}{d\varphi} = r(\varphi) = \frac{x_0}{2\pi} + \frac{1}{\pi} \sum_{n=1}^{\infty} [x_n \cos(n\varphi) + y_n \sin(n\varphi)], \qquad (2.2)$$

where

$$x_n = \int_0^{2\pi} r(\varphi) \cos(n\varphi) d\varphi, \quad y_n = \int_0^{2\pi} r(\varphi) \sin(n\varphi) d\varphi. \qquad (2.3)$$

Defining $x_n = v_n \cos(n\psi_n)$ and $y_n = v_n \sin(n\psi_n)$ $(v_n \equiv \sqrt{x_n^2 + y_n^2})$ where ψ_n is angle between x-axis and reaction plane[2], normalizing $v_0 = \int_0^{2\pi} r(\varphi) d\varphi = 1$ and using trigonometrical identity $\cos(a - b) = \cos(a) \cos(b) + \sin(a) \sin(b)$, formula

$$\frac{dN}{d\varphi} = \frac{1}{2\pi} \left(1 + 2 \sum_{n=1}^{\infty} v_n \cos[n(\varphi - \psi_n)] \right) \qquad (2.4)$$

---

[2]Reaction plane is defined by the impact parameter $\vec{b}$ and the z-axis which is parallel to beamline.

can be obtained. In symmetric nuclear collisions, v_n averaged over all particles in all events can be expressed as $v_n = \langle \cos[n(\varphi - \psi_n)] \rangle$ [47]. In an experiment, Fourier coefficients can be corrected for the event plane resolution [48].

Fourier coefficients v_1, v_2 and v_3 are called directed, elliptic and triangular flow respectively. Higher v_n coefficients also contribute but their importance is not so significant. Unity in equation (2.4) stands for radial flow which is the isotropic component of the flow. Schematic picture of how the elliptic and triangular flow can appear from spatial overlap of the nuclei in a collision is shown in Fig. 2.3. Participant plane Ψ_{PP} is calculated for the particles contributing to the flow. Due to different pressure gradients after the collision, the area of the hot medium changes its shape and spatial anisotropy is transformed into momentum anisotropy. Time evolution of energy density in the transverse plane for elliptic flow can be seen in Fig. 2.4. The graph shows that almond-like shape disappears with time and the system becomes spatially isotropic.

It has also been observed that for $\sqrt{s_{\mathrm{NN}}} > 2$ GeV collision energies the magnitude of elliptic flow increases with $\sqrt{s_{\mathrm{NN}}}$ (Fig. 2.5). More importantly, v_2 changes its sign around $\sqrt{s_{\mathrm{NN}}} \sim 4$ GeV. Because elliptic flow can be expressed as (let $\psi_2 = 0$)

$$v_2 = \langle \cos(2\varphi) \rangle = \langle \cos^2(\varphi) - \sin^2(\varphi) \rangle = \left\langle \left(\frac{p_x}{p_T} \right)^2 - \left(\frac{p_y}{p_T} \right)^2 \right\rangle, \qquad (2.5)$$

sign change of v_2 is directly connected to v_2 shape in x-y plane. It is believed that at low energies, where $v_2 < 0$, the matter is not Lorentz contracted and v_2 is created by nucleons while for $v_2 > 0$ region more quarks and gluons is involved in the collision.
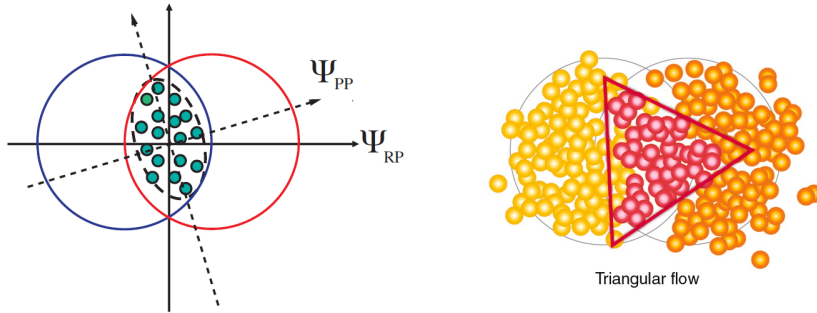

Figure 2.3: Figure illustrates from transverse plane point of view how initial conditions of a collision can contribute to elliptic (left) [49] and triangular (right) [50] flow. Ψ_{RP} identifies reaction plane and Ψ_{PP} participant plane.

2.1.1 Mass Ordering and Constituent Quark Scaling

Two phenomenons regarding elliptic flow have been observed. It has been found that heavy particles such as protons experience different elliptic flow p_T dependence than light particles as pions. This phenomenon is called mass ordering. Up to $p_T < 2$
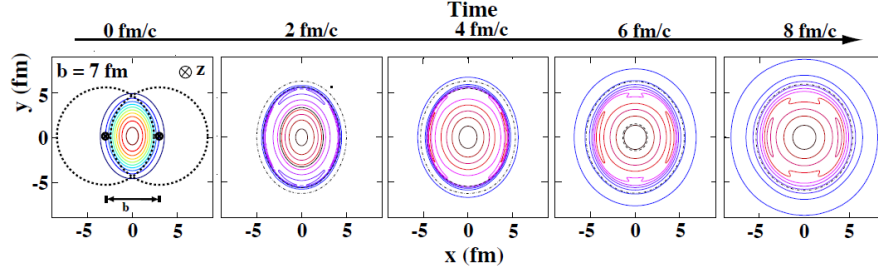
Figure 2.4: Series of graphs shows time dependence of created initial transverse energy density for a non-central heavy-ion collision [49].
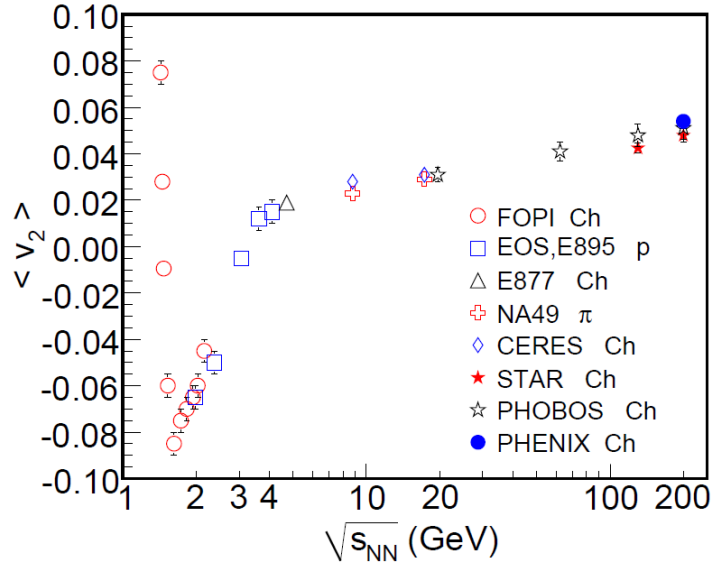

Figure 2.5: Average elliptic flow $\langle v_2 \rangle$ as a function of beam energy $\sqrt{s_{NN}}$ [51].

GeV/c for RHIC and $p_T < 2.5$ GeV/c for LHC heavier particles show smaller v_2 then the light ones while for higher p_T the mass ordering breaks and v_2 shows stronger dependence on particle's quark composition [52]. Mass ordering of v_2 can be seen for RHIC and LHC data in Fig. 2.6a and Fig. 2.7a respectively. Characteristic mass dependence can be explained by interplay between anisotropic elliptic and azimuthally symmetric radial flow [53].

Breaking of the mass ordering in the $2 < p_T < 4$ GeV/c region hints the other phenomenon called constituent quark scaling. At RHIC energies it has been observed that, when elliptic flow and p_T is scaled by the number of constituent quarks n of the particle, all particles follow the same curve. To more pronounce this scaling, variable $KE_T = m_T - m_0$ considering relativistic effects is used, where $m_T = \sqrt{p_T^2 + m_0^2}$ is transverse mass and m_0 is rest mass of the particle. Quark scaling of v_2 at RHIC can be seen in Fig. 2.6b. However, deviations from quark scaling have been observed at LHC energies (Fig. 2.7b). One of the reasons might be abundance of jets [54]. From constituent quark scaling it can be concluded that the elliptic flow is created during pre-hadronic stage [55] and that flow at the constituent quark level strongly

supports quark-like degrees of freedom [52].

Interestingly, elliptic flow mass ordering has been observed also in high multiplicity p+p collision which hints medium creation even in p+p collisions. Fig. 2.8 shows $v_2(p_T)$ distributions extracted from long-range two-particle correlations in p+p collisions at $\sqrt{s} = 13$ TeV energy together with that in p+Pb and Pb+Pb collisions. Graphs are labeled by reconstructed track multiplicity $N_{\text{trk}}^{\text{offline}}$ and particle pairs are formed by associating each charged trigger particle originating from the primary vertex within a given p_T^{trig} range with the remaining charged primary tracks in specified p_T^{assoc} interval.
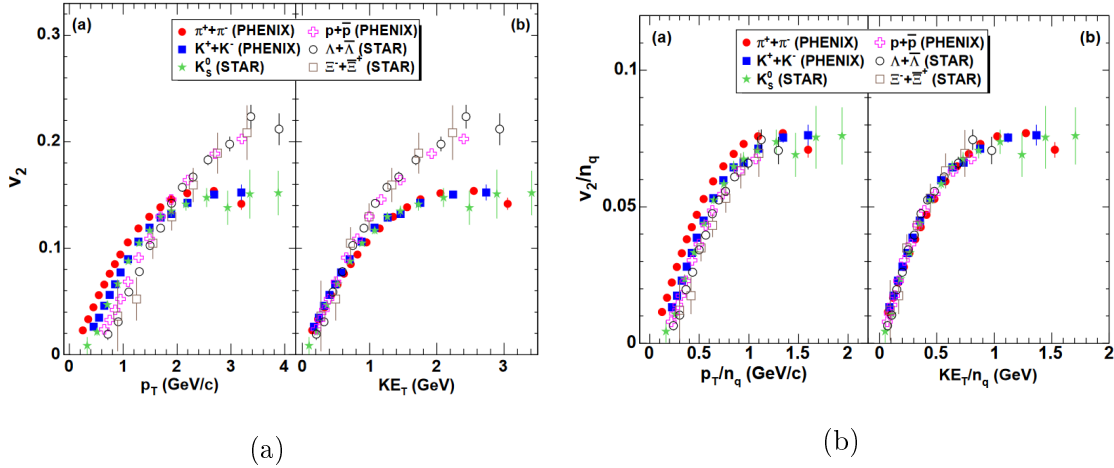
Figure 2.6: Elliptic flow v_2 dependence of different particle species on p_T and KE_T in minimum bias Au+Au at $\sqrt{s_{\text{NN}}} = 200$ GeV [52]. In the right graph (b) constituent quark scaling has been performed. Data points have been obtained from Au+Au and Cu+Cu collisions.

2.1.2 η/s Determination Using Collective Flow

By comparing collective flow results to relativistic viscous hydrodynamic simulations, information about the medium shear viscosity to entropy density ratio η/s can be inferred. Comparison in Fig. 2.9 shows that QGP can be treated as an almost perfect fluid[3] with minimal viscosity. Under a rough approximation of η/s being independent on temperature, values $\eta/s = 0.12$ for RHIC energy and $\eta/s = 0.2$ for LHC energy describe the data very well. Simulation considering temperature dependence using HH-HQ parametrization[4] with a minimum $\eta/s(T) = 0.08$ at $T_c = 180$ MeV [58] is also considered and for RHIC gives worse description of the data which implies that the correct temperature dependence has not been extracted yet. The lower bound $\eta/s = 0.08 = \frac{1}{4\pi}$ is set because of $\eta/s \geq \frac{1}{4\pi}$ condition coming from gauge theories in the strong coupling limit [59].

---

[3]Perfect fluid has no shear viscosity.

[4]HH-HQ parametrization uses different $\eta/s(T)$ dependencies for both hadron gas and QGP phase.
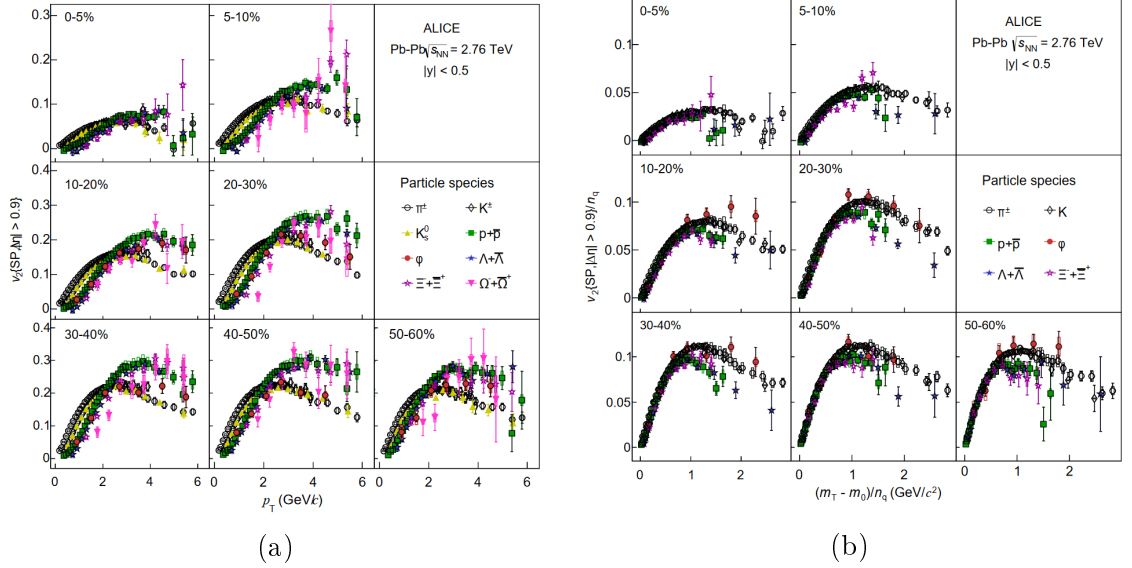
Figure 2.7: Elliptic flow scalar product (SP) v_2 dependence of different particle species on p_T and KE_T at LHC energy $\sqrt{s_{NN}} = 2.76$ TeV [53]. In the right graph (b) constituent quark scaling has been performed.
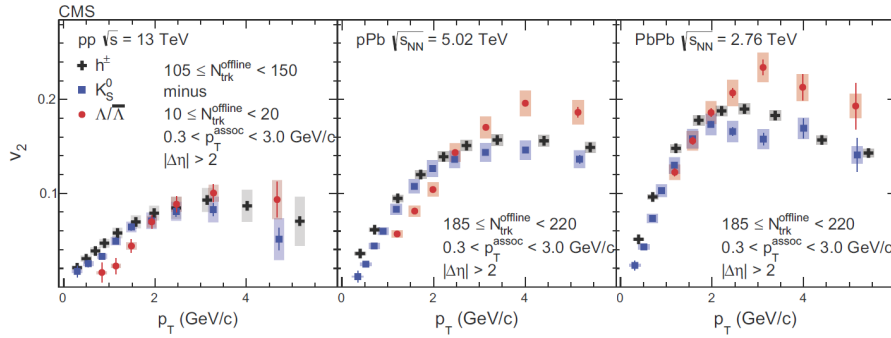

Figure 2.8: Elliptic flow $v_2(p_T)$ of inclusive charged particles, K_S^0 and $\Lambda/\bar{\Lambda}$ particles in p+p [56], p+Pb and Pb+Pb [57] collisions at CMS experiment.

Temperature dependent $\eta/s(T)$ results of lattice QCD have also been computed and are shown in Fig. 2.10. In $T/T_c \sim 1-3$ region, lattice QCD results $0.08 < \eta/s < 0.3$ are close to that from hydrodynamics.

2.2 Jet Quenching

At high energies $\sqrt{s_{NN}} > 40$ GeV, high transverse momentum partons with $p_T \gtrsim 2$ GeV/c can be used to study properties of the created medium. Firstly, because they originate from partonic scatterings with large momentum transfer Q^2, and secondly, because they are produced in short timescales $\tau \sim 1/p_T \leq 0.1$ fm/c and propagate through the medium [36].

Evolution of a hard parton scattering can be seen in Fig. 2.11. Outgoing scattered
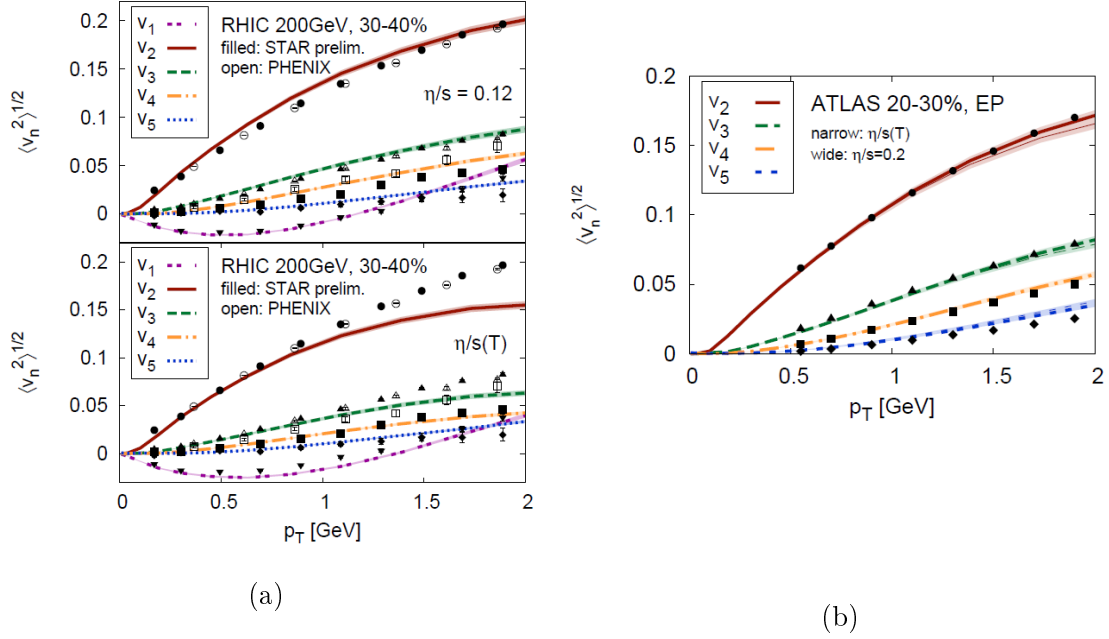
Figure 2.9: (a) Comparison of $v_n(p_T)$ at RHIC using $\eta/s = 0.12$ and temperature dependent $\eta/s(T)$ with data from PHENIX and STAR experiments in 30-40% centrality region. (b) Comparison of $v_n(p_T)$ at LHC using $\eta/s = 0.2$ and temperature dependent $\eta/s(T)$ with data from ATLAS experiment in 20-30% centrality region. Bands indicate statistical errors. Both graphs are taken from Ref. [60].
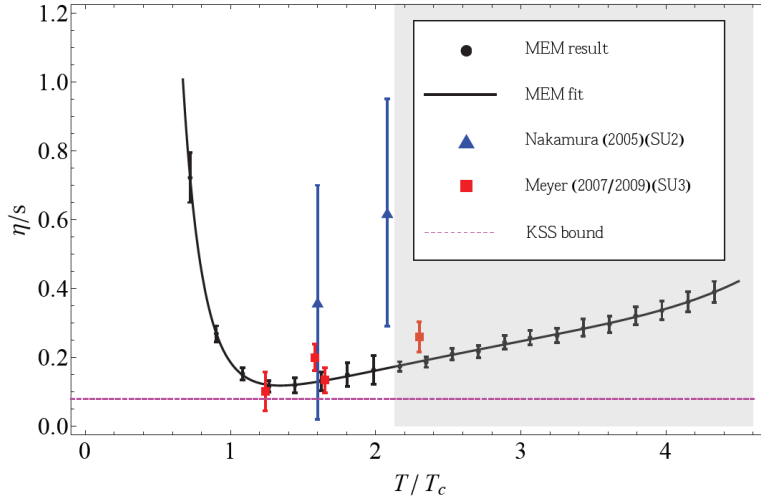

Figure 2.10: η/s lattice QCD results with displayed lower bound $\eta/s = 0.08$ [61].

partons radiate gluons which split into $q\bar{q}$ pairs and finally hadronize. Outgoing collimated spray of hadrons resulting from the fragmentation of an outgoing parton is called a jet. Due to energy loss in the medium, attenuation or disappearance of a jet can be observed. Such phenomenon is called jet quenching.

Both collisional and radiative energy loss ΔE_{coll} and ΔE_{rad} contribute to the total energy loss ΔE. Collisional energy loss comes from elastic scatterings with medium
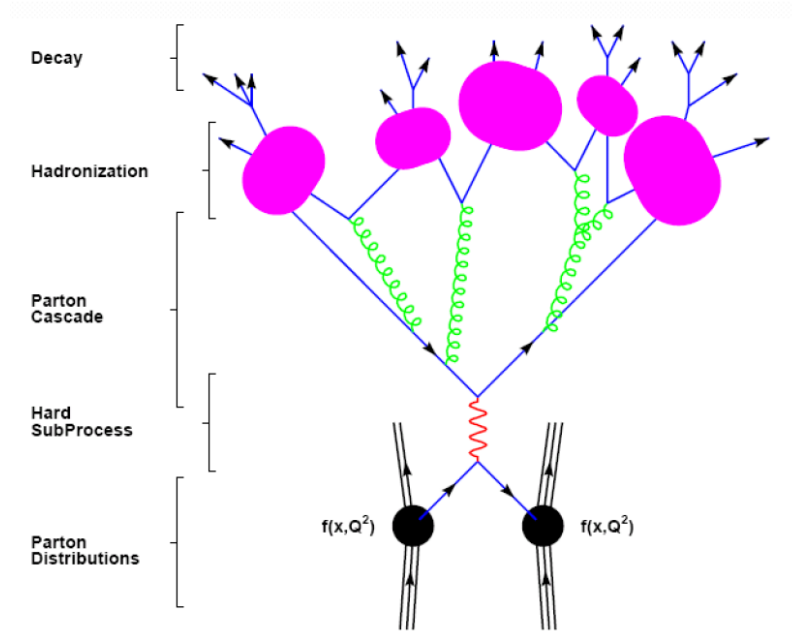
Figure 2.11: Schematic evolution of a hard parton scattering [62].

constituents and dominates at low particle momenta while radiative energy loss is caused by inelastic scatterings such as photon or gluon bremsstrahlung and affects particles with high momenta. Feynmann diagrams of both processes can be seen in Fig. 2.12. Radiative losses are proportional to the strong coupling constant α_s, color charge C_R, medium thickness L and transport coefficient $\hat{q}$ in which the medium modifications are encoded, $\Delta E_{rad} \sim \alpha_s C_R \hat{q} L^2$ [36]. They are also mass dependent and the heavier quark the less energy it loses by radiation. Effect of the small-angle $\theta < \frac{M}{E}$ radiation suppression where M is mass of the quark and E its energy is called "dead cone" effect [63].
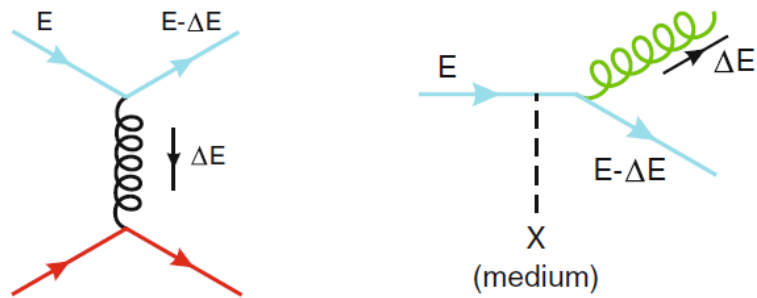
Figure 2.12: Feynmann diagrams for collisional (left) and radiative (right) energy loss of a quark of energy E traversing a quark–gluon medium [36].

In order to study QGP properties by hard partons, their perturbative production cross section and modification by propagation through the strongly interacting medium have to be known. Application of perturbative QCD is justified because

the running strong coupling constant α_s goes to zero with rising momentum transfer Q^2. Calculation of the perturbative cross section $d\sigma_{AB\to h}^{\text{hard}}$ that hadron h is produced in collision of A and B nuclei can be performed in the factorization approach [36]

$$d\sigma_{AB\to h}^{\text{hard}} = f_{a/A}(x_1, Q^2) \otimes f_{b/B}(x_2, Q^2) \otimes d\sigma_{ab\to c}^{\text{hard}}(x_1, x_2, Q^2) \otimes D_{c\to h}(z, Q^2), \quad (2.6)$$

where

- $f_{a/A}(x_1, Q^2)$ is the probability of finding a parton of flavor a and momentum fraction $x_1 = \frac{p_{\text{parton}}}{p_{\text{nucleus}}}$ inside the nucleus A, i.e. the parton distribution function (PDF) ,

- $f_{b/B}(x_2, Q^2)$ is the PDF for a parton of flavor b and nucleus B,

- $D_{c\to h}(z, Q^2)$ is the probability that the parton c fragments into the hadron h with fractional momentum $z = \frac{p_{\text{hadron}}}{p_{\text{parton}}}$, i.e. the fragmentation function (FF), which can be determined from $e^{\pm}A$ or e^+e^- collisions and

- $d\sigma_{ab\to c}^{hard}(x_1, x_2, Q^2)$ is the perturbative partonic cross section computable up to a given order of α_s.

The factorization approach is based on the assumption that characteristic time of a hard parton-parton interaction is much shorter than any long distance interaction occurring before or after the hard collision. Therefore, partons can be considered "frozen" during the hard scattering and nucleus' PDF $f_{a/A}(x, Q^2)$ can be approximated by PDF of a nucleon N, $f_{a/N}(x, Q^2)$, multiplied by number of nucleons A, $f_{a/A}(x, Q^2) = A f_{a/N}(x, Q^2)$. Deviation of a nuclear collision from proton+proton collision is studied by the nuclear modification factor.

In many jet quenching models the factorization theorem is employed and modification by propagation through strongly interacting medium is taken into account by modifying the parton fragmentation function $D_{c\to h}(z)$ by neglecting the Q^2 dependence. Final hadronization is assumed to happen in vacuum after the parton escapes the medium.

In experiment, jet quenching can be observed by suppression of high-p_T leading hadron spectra or by unbalanced $\frac{dN}{d(\Delta\phi)}$ spectra in heavy ion collisions. In the left graph in Fig. 2.13, clear suppression of π^0 production in Au+Au can be seen in $p_T > 5$ GeV/c region with respect to that in p+p. In the right graph in Fig. 2.13, two particle azimuthal distributions for p+p, p+Au and central Au+Au collisions are compared. In Au+Au $\frac{dN}{d(\Delta\phi)}$ spectra, the opposite jet is fully stopped by the medium at $\Delta\phi = \pi$ while this effect is not observed in d+Au or p+p collisions. In the two particle correlations, trigger particles are defined as all charged particles originating from the primary vertex and hadron pairs are formed by associating the remaining charged particles with every trigger particle. There may be more trigger particles in an event and various transverse momentum ranges can be studied for both trigger (p_T^{trig}) and associated (p_T^{assoc}) particles. In this case, the trigger particles were chosen

from $4 < p_T^{\text{trig}} < 6$ GeV/c range and associated particles from $2 < p_T^{\text{assoc}} < p_T^{\text{trig}}$ range. Observed suppression at $\Delta\phi = \pi$ for Au+Au collisions means significant suppression of events in the studied p_T^{assoc} range caused by the medium.
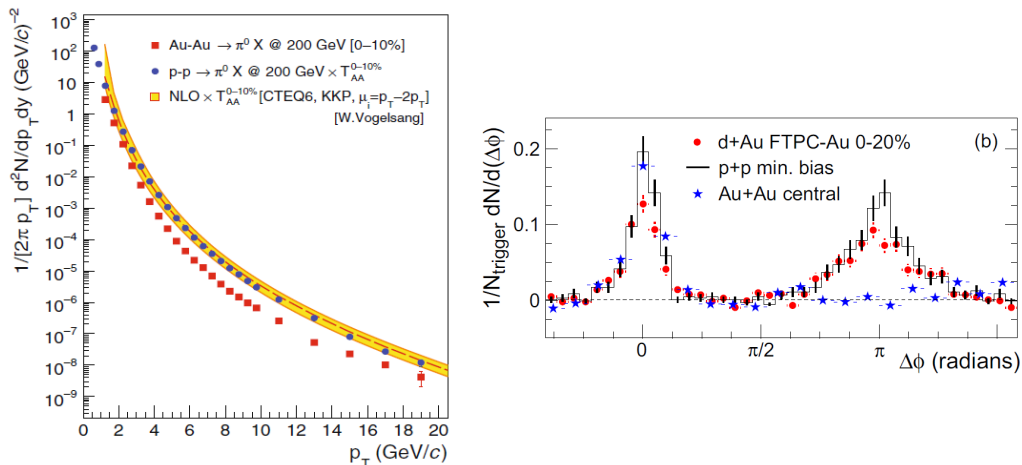

Figure 2.13: Left: Observed suppression of π^0 yield in Au+Au with respect to p+p collisons at PHENIX [36] (data taken from [64, 65]). Right: Comparison of two-particle azimuthal distributions for the 0-20% most central d+Au collisions to those in p+p and central Au+Au collisions at STAR [66]. Shortcut FTPC-Au denotes Forward Time Projection Chamber in the Au beam direction.

Azimuthal spectra can also be studied together with pseudorapidity correlation. In these two-particle $(\Delta\phi, \Delta\eta)$ correlations a so called ridge effect has been observed. Ridge manifests as a clear collective (involving nearly all particles in the event) long-range correlation in relative pseudorapidity $(\Delta\eta)$ which extends over many pseudorapidity units in the $\Delta\phi \approx 0$ and $|\Delta\eta| \gtrsim 2$ region [67]. This effect can be theoretically explained as a sum of collective flow Fourier harmonics [68]. As Fig. 2.14 shows, the ridge effect can be observed in Pb+Pb, p+Pb and p+p collisions. While in Pb+Pb the ridge is attributed to final state interaction in the QGP medium, in p+p collisions this effect can rise also from initial-state geometry.

Strong suppression of high p_T jets is observed to be dependent on centrality and weakly dependent on collision energy at two highest LHC collision energies in Fig. 2.15a. In Fig. 2.15b, R_{AA} dependence of the prompt D mesons[5] and that originating from b quark is shown. A clear stronger suppression of the prompt D mesons (corresponding to c quark) in the area of the green circle, $6 < p_T < 14$ GeV/c, supports the radiative loss quark mass dependence between c and b quarks, $\Delta E_{rad}(c) > \Delta E_{rad}(b)$.

2.3 Quarkonia Production Modification

Quarkonia are bound states of quark and antiquark of the same flavor and heavy quarkonia are composed of heavy quarks - J/ψ ($c\bar{c}$) and Υ ($b\bar{b}$). Advantage of the heavy quarkonia is the fact that they are created at early stages of the collision and

---

[5]D mesons contain one charm quark or antiquark.
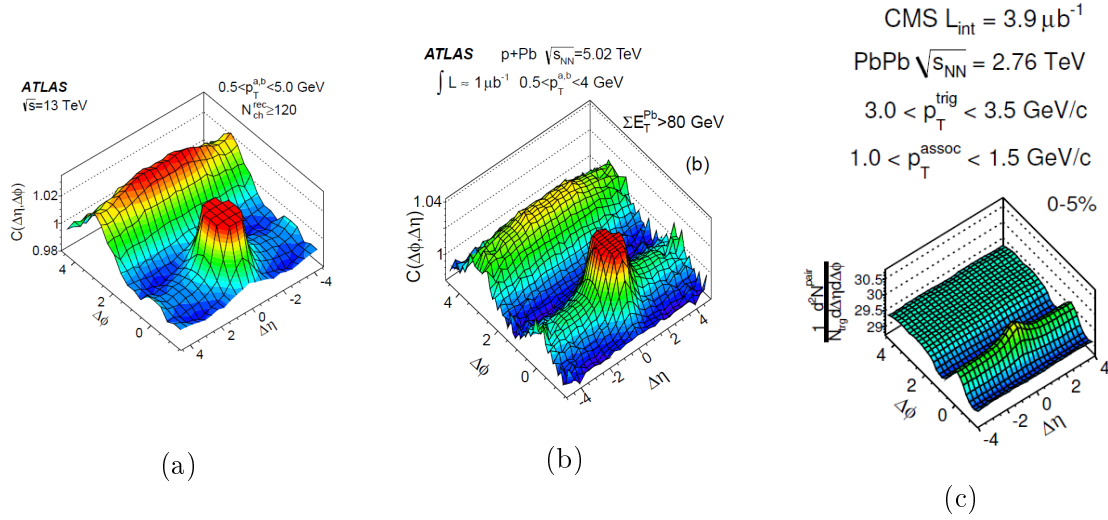
(a)   (b)   (c)

Figure 2.14: Two-particle correlation function $C(\Delta\phi, \Delta\eta)$ for p+p (a) and p+Pb (b) collisions from ATLAS [69, 70] and Pb+Pb (c) collisions from CMS experiment [71]. Peaks at $(\Delta\phi, \Delta\eta) = (0,0)$ have been truncated for p+p and p+Pb collisions graphs.
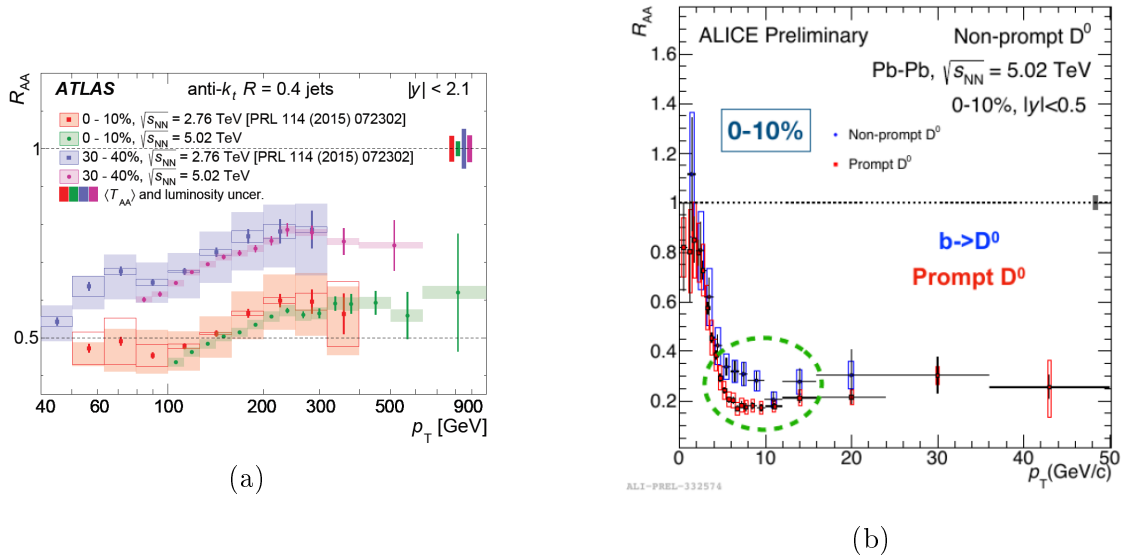

(a)   (b)

Figure 2.15: (a) Nuclear modification factor R_{AA} as a function of jet p_T for jets with $|y| < 2.1$ in $0 - 10\%$ and $30 - 40\%$ centrality intervals for two energies $\sqrt{s_{\mathrm{NN}}} = 2.76$ and 5.02 TeV [72]. (b) Nuclear modification factor R_{AA} p_T dependence for prompt and non-prompt D mesons in 0-10% central Pb+Pb collisions at $\sqrt{s_{\mathrm{NN}}} = 5.02$ TeV [73].

experience the QGP stage. Despite different content of heavy quarkonia, both of them follow qualitatively the same (quantitatively different because of the different masses) production modification effects due to QGP.

In 1986, Matsui and Satz [74] proposed J/ψ suppression as a signature of formation of the high temperature QGP. They came with an idea of color charge screening.

36

Because of the high temperature in the medium, color charge that binds quarkonia together is screened by color charges of quarks and gluons in the medium. This causes the quarkonia to dissociate.

state	J/Ψ	$\chi_c(1P)$	$\Psi(2S)$	$\Upsilon(1S)$	$\Upsilon(2S)$	$\Upsilon(3S)$
mass [GeV/c^2]	3.10	3.53	3.68	9.46	10.02	10.36
radius [fm]	0.25	0.36	0.45	0.14	0.28	0.39

Table 2.1: Masses and radii for charmonia and bottomonia [75].

The limit of the anomalous quarkonium dissociation can be expressed by Debye screening length r_D which is inversely proportional to the temperature T, $r_D \sim 1/T$. When r_D becomes small, all states with radii larger than r_D ($r > r_D$) dissociate. Thanks to various radii of quarkonia (see Tab. 2.1), it is possible to indirectly measure the temperature of the medium by observing a quarkonia sequential suppression [76]. Dependence of the J/ψ survival probability on the energy density of the medium can be seen in Fig. 2.16a. The higher the energy density the more tightly bound quarkonia dissociate. The stronger suppression of exited states $\Upsilon(2S)$ and $\Upsilon(3S)$ can be clearly observed also in Fig. 2.16b where the measured nuclear modification factor R_{AA} for ground Upsilon state $\Upsilon(1S)$ and its excited states $\Upsilon(2S)$ and $\Upsilon(3S)$ is shown.

Fig. 2.17 shows that J/ψ quarkonia are more suppressed in central collisions ($N_{\text{part}} \sim 350$) than in peripheral collisions (small N_{part}). In central collisions higher energy densities are reached and quarkonia are therefore more suppressed. Also, no difference in the suppression is observed between Au+Au collisions at $\sqrt{s_{\text{NN}}} = 200$ GeV and Pb+Pb collisions at $\sqrt{s_{\text{NN}}} = 2.76$ TeV.
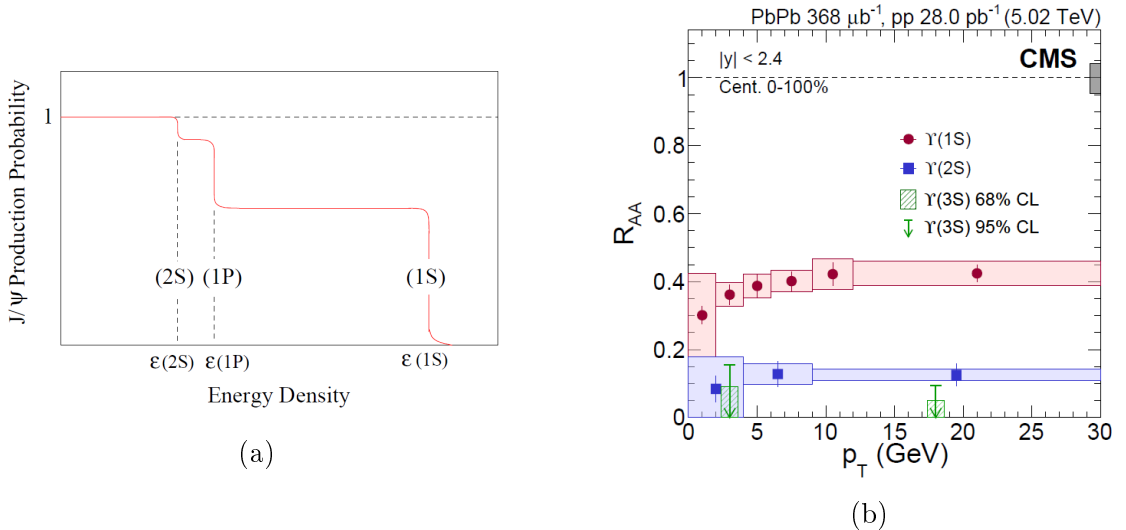

(a)

(b)

Figure 2.16: (a) Illustrative graph of sequential J/ψ suppression by color screening [77]. (b) Nuclear modification factor R_{AA} dependence on p_T for $\Upsilon(1S)$, $\Upsilon(2S)$, $\Upsilon(3S)$ quarkonia in 0-100% central Pb+Pb collisions at $\sqrt{s_{\text{NN}}} = 5.02$ TeV[78].
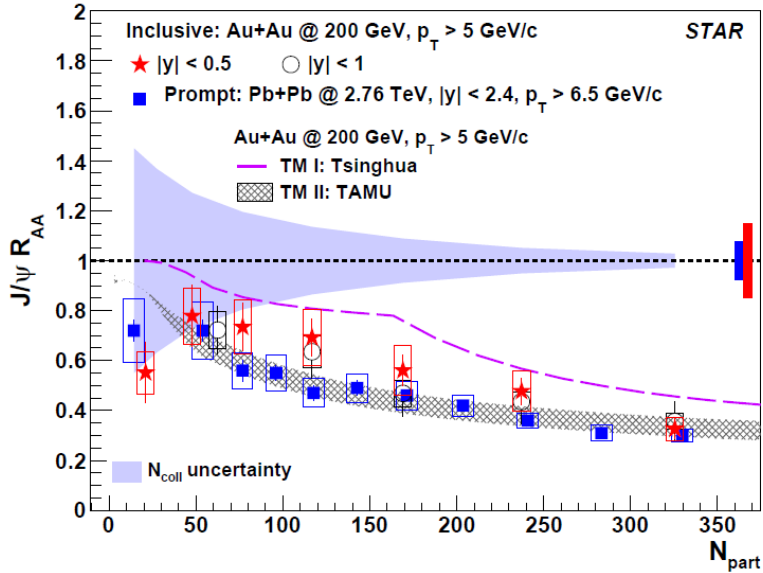
Figure 2.17: Nuclear modification factor R_{AA} dependence on the number of participants N_{part} for J/ψ in mid-rapidity Au+Au collisions at $\sqrt{s_{\text{NN}}} = 200$ GeV and in Pb+Pb collisions at $\sqrt{s_{\text{NN}}} = 2.76$ TeV [79].

However, not only suppression effects contribute to the production modifications. There is also enhancement by recombination caused by coalescence of nearby quarks of the same flavor. Next, the so called feed-down effect and the cold nuclear matter effects contribute and will be discussed in next subsections.

2.3.1 Feed-down and Other Effects

In an experiment, where quarkonia are reconstructed, only inclusive quarkonia are observed and the ground state is usually the most abundant one. This is partially caused by contributions from deexcitation of the excited states, so called feed-down effect. The contribution of J/ψ feed-down from $\psi(2S)$ is 8% and from $\chi_c(1P)$ 25% [80]. The deexcitation is realized by hadronic decays for S states and radiative ones for P states. Scheme of J/ψ excited states can be seen in Fig. 2.18. Labeled thresholds show the dominant decay channel.

2.3.2 Cold Nuclear Matter Effects

In order to describe the observed suppression, Cold Nuclear Matter (CNM) effects have to be accounted for in the quarkonium production modification models. Assumption of insufficient energy density for QGP creation in p+A or d+A collisions allows one to study CNM effects in that collisions. The CNM effects include shadowing, Cronin effect and nuclear absorption with comover interaction.

Modification of the effective partonic luminosity in colliding nuclei with respect to that in proton collisions is one of the CNM effects. Distribution of partons in protons
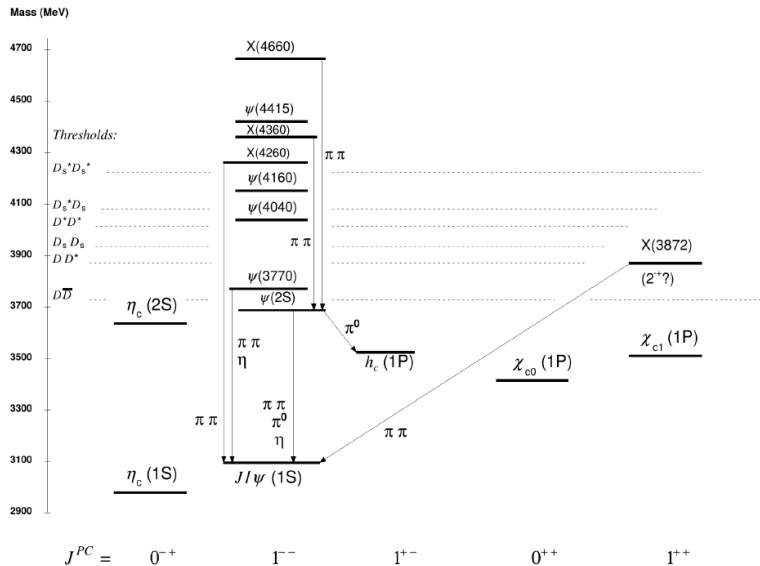
Figure 2.18: Scheme of J/ψ excited states with their masses and hadronic decay channels [81]. Radiative decay channels are omitted.

are described by parton distribution function (PDF). But partons in a single proton behave according to different dynamics than that in nuclei. The latter are influenced by partons from surrounding nucleons and their PDF is modified with respect to a free nucleon. For nuclear-modified PDF shortcut nPDF is used. Quantitatively, the difference can be expressed by ratio R_i of nPDF to PDF [82]

$$R_i(x, Q^2) = \frac{\text{nPDF}_i(x, Q^2)}{\text{PDF}_i(x, Q^2)} \quad , \tag{2.7}$$

where index i denotes flavor of a parton. Parton distribution functions depend on Bjorken x, which is a fraction of the nucleon momentum carried by a parton, and square of four-momentum transfer Q^2.

In Fig. 2.19a, an example shape of R_i can be seen. In region $x \lesssim 10^{-2}$, PDF dominates in (2.7) ($R_i < 1$). The effect is called shadowing and is related to phase-space saturation. Possible enhancement ($R_i > 1$) in area $10^{-2} \lesssim x \lesssim 10^{-1}$ refers to anti-shadowing. Last two effects comprise Fermi motion and yet unexplained EMC effect [85].

Cronin effect and nuclear absorption are also counted among CNM effects. Cronin effect describes enhancement of the nuclear modification factor R_{pA} at high p_T by multiple subsequent scatterings of proton partons on partons of nuclei [86]. By this scattering, partons get transverse momentum impulse and shift into the higher p_T. Therefore with the enhancement comes also suppression in lower p_T. Modeled R_{dAu} dependence on p_T at RHIC energy is shown in Fig. 2.19b and comparison of nuclear modification factors for Pb+Pb and p+Pb collisions can be seen in Fig. 2.2 in the beginning of this chapter. The Cronin effect at RHIC is expected in $2 < p_T < 4$ GeV/c region while at LHC energy is observed in the $3 < p_T < 5$ GeV/c region.
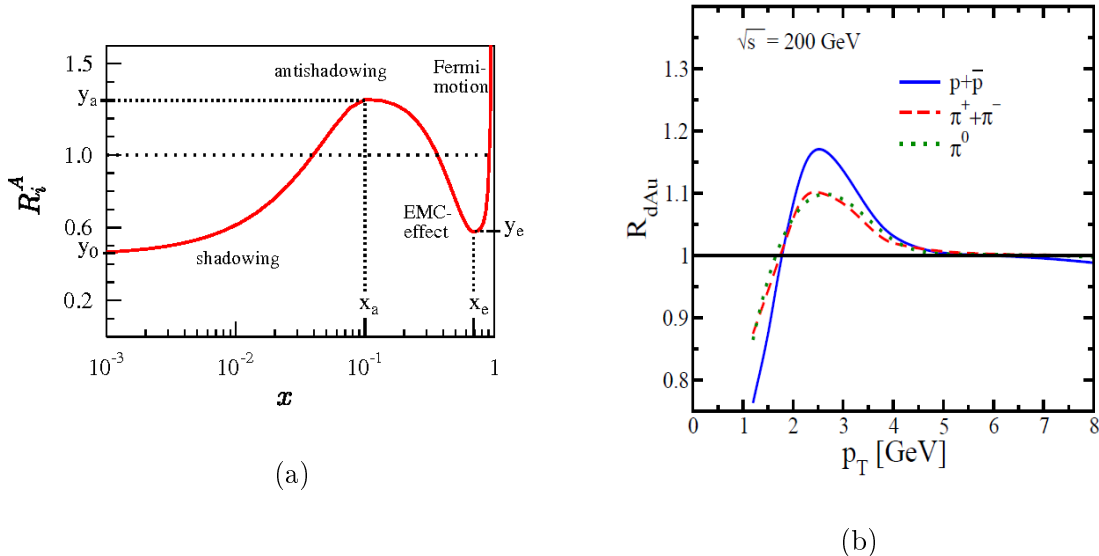
39

Figure 2.19: (a) An illustration of R_i behavior dependent on Bjorken x [83].
(b) Modeled R_{dAu} dependence on p_T for protons and pions in midrapidity for RHIC
[84].

Nuclear absorption explains another addition to quarkonium production suppression. Here, quarkonia dissociate due to interaction with the nucleus [87].

Next, quarkonia can also interact with comoving hadrons which is covered in the comover interaction model. Because of the inelastic scattering with comoving hadrons, quarkonium dissociates which contributes to quarkonium suppression.

2.4   Other Signatures

Other QGP effects such as dilepton and photon production are briefly discussed because they are not directly related to the thesis topic.

By anihilation of quark and antiquark in the QGP, $q\bar{q} \rightarrow l^-l^+$, dilepton pair can be created. Thanks to relative weakness of electromagnetic interaction, produced leptons do not interact with any matter before they reach the detector and therefore carry information about QGP medium. Their production rate and momentum distributions are governed by the thermodynamic condition of the plasma [16] which can be reconstructed, such as initial temperature T_0. However, there are other processes resulting in l^-l^+ pair, such as the Drell-Yan[6] process and hadron ($\pi^\pm$) and resonance decays, which are dominant and have to be carefully analyzed.

Very similar probe as dileptons are photons created in processes $gq \rightarrow \gamma q$ and $q\bar{q} \rightarrow \gamma g$ [16]. After γ is created by interaction of QGP quarks and gluons, it does not interact until it reaches a detector because of weakness of electromagnetic

---

[6]In Drell-Yan process, annihilation of a quark from one nucleon with a sea antiquark from the other nucleon forms dilepton pair, $q\bar{q} \xrightarrow{\gamma} l^-l^+$. Quark and antiquark can be considered independent because they come from different nucleons [16].

interaction and information about the medium can be extracted. Nevertheless, significant contamination by γ from hadron decays and from interactions of colliding or created matter occurs which makes this method very challenging.

Chapter 3

HYDJET++

HYDJET++ is a Monte Carlo (MC) generator for simulation of symmetric relativistic heavy ion collisions. It includes a detailed treatment of soft hadron production and hard multi-parton production [88]. Main part of the HYDJET++ is written in the object-oriented C++ language under the CERN ROOT environment [89]. Hard production in a single nucleon-nucleon collision is obtained as modified jet event from the Fortran-based PYTHIA 6.4 generator [90]. The soft hadronic states of the HYDJET++ model are generated on the chemical and thermal freeze-out hypersurfaces obtained from hydro-inspired blast-wave parameterization with given freeze-out conditions as the boundary conditions. The longitudinal, radial and elliptic flow effects and the decays of hadronic resonances belong to the soft hadron production part which is dominant at transverse momenta $p_T \lesssim 2 - 3$ GeV/c.

HYDJET++ is applicable only to symmetric A+A collisions of heavy ($A \gtrsim 40$) ions at high energies ($\sqrt{s_{\mathrm{NN}}} \gtrsim 10$ GeV) and description of the peripheral ($b \sim 2R_A$[1]) collisions might not be accurate[2]. Model also can deviate from experimental data in very froward rapidities where other effects than flow or jet effects apply. Main aspects of the soft and the hard part of the model are described in the following sections, more details can be found in [88]. Overview of the HYDJET++ accomplishments closes this chapter.

3.1 Hard Multi-jet Production

Description of a multiple scattering of hard partons in dense QCD matter such as QGP is based on the energy loss ΔE of a particle traversing the medium. Basic energy loss can be expressed as a function of energy E and length L [88]

$$\Delta E(E, L) = \int_0^L dl \frac{dP(l)}{dl} \lambda(l) \frac{dE(E, l)}{dl}, \quad \frac{dP(l)}{dl} = \frac{1}{\lambda(l)} \exp\left(\frac{-l}{\lambda(l)}\right), \qquad (3.1)$$

---

[1] b denotes impact parameter and R_A radius of the nuclei.

[2] In peripheral collisions or at lower energies the assumption of the local thermal equilibrium of the system might not be fulfilled.

where l is the current transverse coordinate of a parton, $\frac{dP}{dl}$ is the scattering probability density, $\frac{dE}{dl}$ is the energy loss per unit length, $\lambda = \frac{1}{\sigma\rho}$ is the in-medium mean free path, $\rho \propto T^3$ is the medium density at the temperature T and σ is the integral cross-section for the parton interaction in the medium. Both collisional and radiative energy loss E^{coll} and E^{rad} contribute to the total energy loss ΔE

3.1.1 Radiative Loss

Energy loss of a high energy quark or gluon due to medium stimulated gluon radiation is treated in terms of the Baier-Dokshitzer-Mueller-Schiff (BDMS) model [91, 92]. It has been observed that for the hot matter the QED and QCD problems are mathematically equivalent if one identifies the emission angle of radiated photons in the QED case with the transverse momentum of radiated gluons in the QCD case [93]. Radiative energy loss of a high energy charged particle as it passes through matter in QED has been studied by Landau, Pomeranchuk and Migdal (LPM) [94, 95]. In the BDMS approach, the strength of multiple scattering is characterized by the transport coefficient $\hat{q} = \mu_D^2/\lambda_g$ (μ_D is Debye mass that characterizes the lowest momentum exchanges with the medium and λ_g is the gluon mean free path), which is related to the elastic scattering cross section. In the HYDJET++, this strength is regulated mainly by the initial QGP temperature T_0. Radiative energy loss for massless partons in HYDJET++ is treated as [91, 92]

$$\frac{dE^{\mathrm{rad}}}{dl} = \frac{2\alpha_s(\mu_D^2)C_R}{\pi L} \int_{\omega_{min}}^{E} d\omega \left[1 - y + \frac{y^2}{2}\right] \ln(|\cos(\omega_1\tau_1)|), \qquad (3.2)$$

where

$$\omega_1 = \sqrt{i\left(-y + \frac{C_R}{3}y^2\right)\bar{\kappa}\ln\frac{16}{\bar{\kappa}}}, \quad \bar{\kappa} = \frac{\mu_D^2\lambda_g}{\omega(1-y)}, \qquad (3.3)$$

$\tau_1 = \frac{L}{2\lambda_g}$, $y = \omega/E$ is the fraction of the parton energy carried away by the radiated gluon, E is the initial parton energy, $\omega_{\min} = \mu_D^2\lambda_g$ and C_R is the color factor. In case of heavy quarks with mass m_q, the "dead-cone" approximation has been used [63]:

$$\frac{dE}{dld\omega}\bigg|_{m_q \neq 0} = \frac{1}{(1 + (\beta\omega)^{3/2})^2} \frac{dE}{dld\omega}\bigg|_{m_q = 0}, \quad \beta = \left(\frac{\lambda}{\mu_D^2}\right)^{1/3}\left(\frac{m_q}{E}\right)^{4/3}. \qquad (3.4)$$

Effects of double parton scattering and thermal gluon absorption have not been included.

The medium, where partonic rescattering occurs, is treated as a boost-invariant longitudinally expanding quark–gluon fluid with partons being produced on a hypersurface of equal proper times τ. For simplicity, the Bjorken model [96] for a temperature T and energy density ε of QGP at $T > T_c \sim 200$ MeV has been used. For

angular spectrum of the in-medium gluon radiation, the "small-angle" parameterization of the gluon distribution over the emission angle θ

$$\frac{dN^g}{d\theta} \propto \sin\theta \exp\Big(-\frac{(\theta-\theta_0)^2}{2\theta_0^2}\Big) \tag{3.5}$$

has been used with $\theta_0 \sim 5°$ as a typical angle of the coherent gluon radiation according to Ref. [97].

The model for the single hard nucleon–nucleon subcollision takes input from PYTHIA 6.4 and is called PYQUEN [98]. Procedure goes as follows:

1. Initial parton spectra and production vertices at given impact parameter are generated with PYTHIA.

2. Rescattering-by-rescattering of the parton path in a dense zone and its radiative and collisional energy loss is simulated.

3. Final hadronization with the Lund string model [99] for hard partons and in-medium emitted gluons is performed.

Then the PYQUEN multi-jets generated according to the binomial distribution are included in the hard part of the event. The mean number of jets produced in A+A events at a given impact parameter b is given by the formula

$$\overline{N_{AA}^{\text{jet}}}(b,\sqrt{s},p_T^{\min}) =$$
$$\int_{p_T^{\min}} dp_T^2 \int dy \frac{d\sigma_{NN}^{\text{hard}}(p_T,\sqrt{s})}{dp_T^2 dy} \int_0^{2\pi} d\psi \int_0^\infty r dr T_A(r_1) T_A(r_2) S(r_1,r_2,p_T,y), \tag{3.6}$$

where $\frac{d\sigma_{NN}^{\text{hard}}(p_T,\sqrt{s})}{dp_T^2 dy}$ is differential cross-section of the corresponding hard process in nucleon-nucleon collisions (at c.m.s. energy $\sqrt{s}$ of colliding beams) with the minimum transverse momentum transfer $p_T^{\min}$, T_A is the nuclear thickness function, $r_{1,2}$ are the transverse distances between the centers of colliding nuclei and the jet production vertex, y is rapidity and factor $S = S_A(x_1,Q^2,r_1)S_A(x_2,Q^2,r_2) \leq 1$ takes into account nuclear shadowing. Here, S_A is parameterization of the ratio of the nucleon structure functions in the nucleus A and that of a free nucleon obtained within Glauber–Gribov theory [100], $x_{1,2}$ are momentum fractions of initial partons of the nucleons involved in the hard process with the momentum transfer $Q^2 = x_1 x_2 s$. Because of the $r_{1,2}$ dependence, nuclear shadowing coefficient depends on the impact parameter and it increases with the more central collisions. By increasing x and Q^2 in the structure functions the nuclear shadowing effect decreases and at a sufficiently high p_T S becomes close to unity.

Partons produced with the momentum transfer lower than $p_T^{\min}$ are considered to be "thermalized" so their hadronization products are included in the soft part of the event.

3.1.2 Collisional Loss

The next part of the energy loss caused by collisions with other particles in form of elastic scatterings is treated in high momentum transfer limit. For the scattering of a hard parton with energy E and mass m_p off the "thermal" parton with energy (or effective mass) $m_0 \sim 3T \ll E$, the energy loss can be expressed as [101, 102]

$$\frac{dE^{\mathrm{col}}}{dl} = \frac{1}{4T\lambda\sigma} \int_{\mu_D^2}^{t_{\max}} dt \frac{d\sigma}{dt} t, \tag{3.7}$$

where the dominant contribution to the differential scattering cross-section is

$$\frac{d\sigma}{dt} \cong C \frac{2\pi\alpha_s(t)}{t^2} \frac{E^2}{E^2 - m_p^2} \quad \text{with} \quad \alpha_s = \frac{12\pi}{(33 - 2N_f)\ln(t/\Lambda_{\mathrm{QCD}})} \tag{3.8}$$

where t is the momentum transfer, $C = 9/4, 1, 4/9$ for gg, gq and qq scatterings, respectively, α_s is the QCD running coupling constant for N_f active quark flavors, Λ_{QCD} is the QCD scale parameter which is of the order of the critical temperature of quark–hadron phase transition, $\Lambda_{\mathrm{QCD}} \simeq T_c \simeq 200$ MeV, $t_{\max} = [s - (m_p + m_0)^2][s - (m_p - m_0)^2]/s$ with $s = 2m_0 E + m_0^2 + m_p^2$, λ is the mean free path and the integrated cross section σ is regularized by the Debye screening mass squared $\mu_D^2(T) \simeq 4\pi\alpha_s T^2(1 + N_f/6)$. Collisional energy loss is due to scatterings with low momentum transfer not considered in HYDJET++ because of the negligible contribution. Another model assumption is that the collisional loss represents the incoherent sum over all scatterings.

3.2 Soft Hadron Production

In the soft part of the HYDJET++, the hadronic states are generated on the chemical and thermal freeze-out hypersurfaces obtained from the Bjorken-like[3] blast-wave parameterization with preset freeze-out conditions [88]. Soft hadron production is based on fast Monte Carlo generator developed in Ref. [103, 104]. It is assumed that a hydrodynamic expansion of the fireball ends by an instantaneous breakup of the whole volume into hadrons at a given constant temperature T^{ch} and chemical potentials μ for baryon number, strangeness, charmness and electric charge. If a consistent description of the data can be achieved by a specific set of parameters, it is meaningful to assume that the parameters characterize the true physical quantities [105].

The momentum distribution of the produced hadrons retains the thermal character of the (partially) equilibrated Lorentz invariant distribution function in the fluid

---

[3]Coordinates t, z are substituted by the Bjorken ones $\tau = \sqrt{t^2 - z^2}, \eta = \frac{1}{2} \ln \frac{t+z}{t-z}$.

element rest frame [106, 107]:

$$f_i^{\text{eq}}(E^*; T^{\text{ch}}, \mu_i, \gamma_s) = \frac{g_i}{\gamma_s^{-n_i^s} \exp\left(\frac{E^* - \mu_i}{T^{\text{ch}}}\right) \pm 1}, \tag{3.9}$$

where E^* is the hadron energy in the fluid element rest frame, $g_i = 2J_i + 1$ is the spin degeneracy factor, $\gamma_s \leq 1$ is the (optional) strangeness suppression factor and n_i^s is the number of strange quarks and antiquarks in a hadron i. Plus and minus sign in the denominator correspond to the Fermi-Dirac and Bose-Einstein statistics, respectively.

If a common chemical and thermal freeze-out temperatures are assumed, the mean number of each particle and resonance species at chemical freeze-out can be determined from temperature T and one of the chemical potentials per unit charge $\tilde{\mu}_i$ while other chemical potentials are fixed (i represents baryon, strangeness, electric charge, charmness and other potentials). However, more complicated scenario with different chemical and thermal freeze-out temperatures T^{ch} and T^{th} is implemented in the HYDJET++. In chemically frozen evolution, particle numbers are assumed to be conserved. To determine particle densities $n_i^{\text{eq}}(T^{\text{th}}, \mu_i^{\text{th}})$ at temperature of the thermal freeze-out $T^{\text{th}} \leq T^{\text{ch}}$, conservation of the particle fractions from the chemical to thermal freeze-out is supposed.

Multiplicity of simulated event follows Poisson distribution with mean value at mean multiplicity $\overline{N_i}$. The mean multiplicity of a hadron species i is computed using effective thermal volume approximation [103, 108, 109]

$$\overline{N_i} = n_i^{\text{eq}}(T, \mu_i) V_{\text{eff}}, \tag{3.10}$$

where $n_i^{\text{eq}}(T, \mu_i) = \frac{g_i}{2\pi^2} m_i T \sum_{k=1}^{\infty} \frac{(\mp)^{k+1}}{k} \exp\left(\frac{k\mu_i}{T}\right) K_2\left(\frac{km_i}{T}\right)$ (K_2 is the modified Bessel function of the second order, m_i is the particle mass, g_i is the degeneracy factor) is the particle number density[4] and V_{eff} is effective thermal volume which can be expressed as

$$\begin{aligned} V_{\text{eff}} = &\tau \int_0^{2\pi} d\phi \int_0^{R(b,\phi)} \sqrt{1 + \delta(b) \tanh^2 \tilde{\rho}_u(r, b) \cos(2\phi)} \\ &\cosh \tilde{\rho}_u(r, b) r dr \int_{\eta_{\min}}^{\eta_{\max}} f(\eta) d\eta \end{aligned} \tag{3.11}$$

where τ is the proper time, $R(b, \phi)$ is the fireball transverse radius for impact parameter b in the azimuthal direction ϕ, $\delta(b)$ is momentum anisotropy parameter, $\tilde{\rho}_u(r, b) = \frac{r}{R_f(b)} \rho_u^{\max}(b = 0)$ and $f(\eta)$ are transverse (linear) and longitudinal (Gaussian) fluid flow rapidity profiles, respectively, where $R_f(b)$ is the mean-square radius

---

[4]The particle number density $n_i^{\text{eq}}(T, \mu_i) = \int d^3\vec{p}^* f_i^{\text{eq}}(E^*; T^{\text{ch}}, \mu_i)$ is expressed in the fluid element rest frame (marked by asterisk) using expansion $f_i^{\text{eq}}(E^*; T^{\text{ch}}, \mu_i) = \frac{g_i}{(2\pi)^3} \sum_{k=1}^{\infty} (\mp)^{k+1} \exp(k\frac{\mu_i - E_i^*}{T})$ [103].

of the hadron emission angle, $\rho_u^{\max}(b = 0)$ is the maximal transverse fluid flow rapidity for central collisions and η is pseudorapidity. In the HYDJET++, V_{eff} is calculated only for $b = 0$ and for other values of the impact parameter it is calculated from the mean number of participants. The mean multiplicity $\overline{N_i}$ is proportional to the number of participating nucleons at a given impact parameter of a nuclei collision [88].

Spatial momentum anisotropy ε and momentum anisotropy δ parameters govern simulation of the collective flow[5]. Transverse radius of the fireball is elliptically modified and can be expressed as [110]

$$R_{\text{ell}}(b, \phi = R_f(b)\frac{\sqrt{1 - \varepsilon_2^2(b)}}{\sqrt{1 + \varepsilon(b)\cos 2\varphi}}, \tag{3.12}$$

where $R_f(b) = R_0\sqrt{1 - \varepsilon_2(b)}$ and R_0 is the freeze-out transverse radius in the case of absolutely central collision, $b = 0$. Momentum anisotropy is utilized as correlation of particle azimuthal angle ϕ and azimuthal angle of the fluid cell φ_{cell}

$$\tan\varphi_{\text{cell}} = \sqrt{\frac{1 - \delta_2(b)}{1 + \delta_2(b)}}\tan\varphi. \tag{3.13}$$

Both $\varepsilon_2(b)$ and $\delta(b)$ can be treated as independent parameters or can be related to each other by hydrodynamical expression [111]

$$v_2(\varepsilon_2, \delta_2) \propto \frac{2(\delta_2 - \varepsilon_2)}{(1 - \delta_2^2)(1 - \varepsilon_2^2)}. \tag{3.14}$$

Triangular flow modulation is introduced with randomly oriented triangular flow event plane angle $\Psi_{\text{EP},3}$ and modifies $R(b, \varphi)$ as

$$R(b, \varphi) = R_{\text{ell}}(b)[1 + \varepsilon_3(b)\cos[3(\varphi - \Psi_{\text{EP},3})]]. \tag{3.15}$$

Triangular momentum anisotropy is corrected by modulation of the maximal transverse flow rapidity $\rho_u^{\max}$ using anisotropy parameter $\rho_3(b)$

$$\rho_u^{\max} = \rho_u^{\max}(0)(1 + \rho_3(b)\cos[3(\varphi - \Psi_{\text{EP},3})]), \tag{3.16}$$

where u is the 4-velocity of the fluid cell. No higher harmonics (v_4, v_5) are intrinsically built in HYDJET++.

Characteristic bump shape of the anisotropic flow p_T distribution is caused by the interplay of the soft and hard HYDJET++ parts. Unlike hydrodynamic models, dissipative processes such as shear viscosity do not need to be implemented in HYDJET++.

---

[5]Subscript 2 and 3 denotes elliptic and triangular flow respectively.

Mean multiplicity of charm mesons can be controlled by γ_c enhancement factor. Multiplicities of thermalized open charm mesons (D mesons), N_D^{th}, and hidden charm meson J/ψ, $N_{J/\psi}^{\text{th}}$, computed from effective thermal volume approximation are scaled by γ_c:

$$N_D = \gamma_c N_D^{\text{th}}, \quad N_{J/\psi} = \gamma_c^2 N_{J/\psi}^{\text{th}}. \tag{3.17}$$

Possibility of γ_c computation from statistical model charm balance equation has also been implemented in HYDJET++ [112].

The fast soft hadron simulation procedure includes the five following steps:

1. Generation of the 4-momentum of a hadron in the rest frame of a liquid element in accordance with the equilibrium distribution function.

2. Generation of the spatial position of a liquid element and its local 4-velocity in accordance with phase space and the character of motion of the fluid.

3. The standard von Neumann rejection/acceptance [113] procedure to account for the difference between the true and generated probabilities.

4. Boost of the hadron 4-momentum into the center mass frame of the event.

5. The two- and three-body decays of resonances with branching ratios taken from the SHARE particle decay table [114].

3.3   Selected Main HYDJET++ Results

HYDJET++ has been developed in 2009 and since that time it has managed to describe many experimental features and phenomenons. One of the key abilities of the HYDJET++ is that different processes can by switched on and off and their impact on the final distributions can be separately examined. Also jet (hard) or thermal (soft) origin of the effect can be easily deduced. Overview of the main results is offered in this section.

HYDJET++ can very well describe charged particles' p_T and η distributions of various observables over wide range of centralities and energies. Multiplicity dependence and p_T distribution in Pb+Pb collisions at $\sqrt{s_{\text{NN}}} = 2.76$ TeV can be seen in Fig 3.1. Here extraction of the soft and the hard component is shown. It has been found that contribution of the hard component to the total multiplicity is about 25% and that soft processes are dominant in small p_T.

Next, elliptic and triangular flow of charged particles can be remarkably described by the HYDJET++. In Fig. 3.2, $v_2(p_T)$ dependence of charged hadrons can be seen in 6 centrality bins in 10-40% range with decomposed soft and hard part. Constituent quark scaling and mass ordering can also be reproduced by the HYDJET++ in Au+Au collisions at $\sqrt{s_{\text{NN}}} = 200$ GeV and in Pb+Pb at $\sqrt{s_{\text{NN}}} = 2.76$ TeV [54, 116]. It has been observed that soft processes follow the constituent quark scaling up to
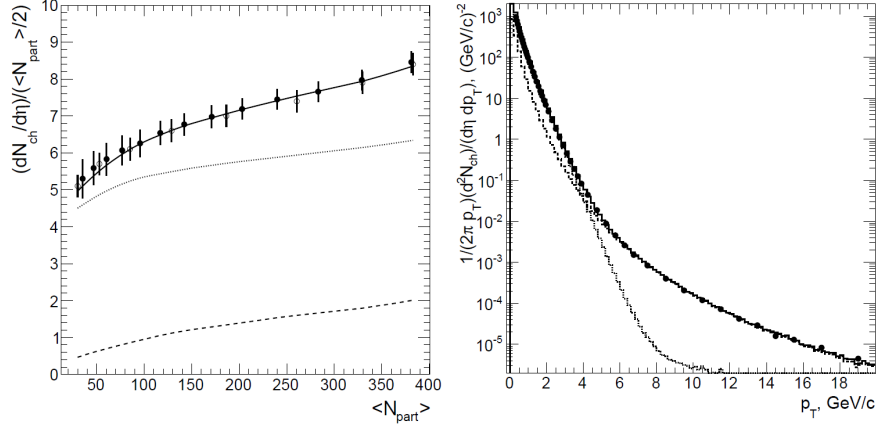
Figure 3.1: Multiplicity density dependence on the mean number of participants $\langle N_{\mathrm{part}} \rangle$ for charged particles (left) and p_T distribution of charged particles for the 0-5% most central collisions (right) compared to experimental data. Graphs show Pb+Pb collisions at energy $\sqrt{s_{\mathrm{NN}}} = 2.76$ TeV. Solid curve is the total result, dashed curve is the hard component and dotted curve is the soft component. Figure is taken from Ref. [115].
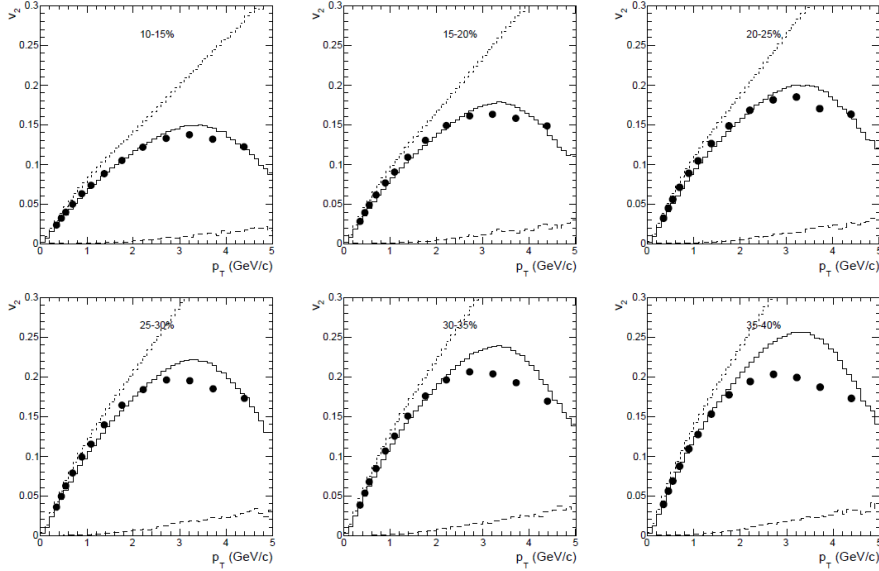
Figure 3.2: Elliptic flow $v_2(p_T)$ dependence of charged hadrons at $|\eta| < 0.8$ for different centralities in Pb+Pb collisions at $\sqrt{s_{\mathrm{NN}}} = 2.76$ TeV compared to CMS experimental data. Solid curve is the total result, dashed curve is the hard component and dotted curve is the soft component. Graphs are taken from Ref. [115].

$kE_T/n_{\mathrm{q}} = 2$ GeV while the hard processes break this scaling around $kE_T/n_{\mathrm{q}} = 1$ GeV for triangular flow (Fig. 3.3). If only direct processes are studied, the breaking of the quark scaling happens already at $kE_T/n_{\mathrm{q}} = 0.5$ GeV for the elliptic flow [54]. The HYDJET++ can reproduce all the v_2, v_3 and v_4 flow coefficients in Pb+Pb collisions at $\sqrt{s_{\mathrm{NN}}} = 2.76$ TeV in 10-40% centrality range. Higher order harmonics v_5 and v_6 trends can also be described [117]. Next, HYDJET++ results in Pb+Pb collisions at $\sqrt{s_{\mathrm{NN}}} = 2.76$ TeV support the idea that hexagonal flow v_6 can be

understood as a superposition of v_2 and v_3, $v_6 \sim \frac{1}{6}v_2^3 + \frac{1}{3}v_3^2$ [118]. Using superposition of only v_2 and v_3 flow harmonics, observed ridge structures can be reproduced by the HYDJET++ in mid-central Pb+Pb collisions [119]. The HYDJET++ $(\Delta\eta, \Delta\varphi)$ two particle correlation function in 0-5% centrality interval and comparison of the $\Delta\varphi$ variable to the experimental data in $2 < \Delta\eta < 4$ from central to peripheral collisions in Pb+Pb at $\sqrt{s_{\mathrm{NN}}} = 2.76$ TeV energy can be seen in Fig. 3.4.
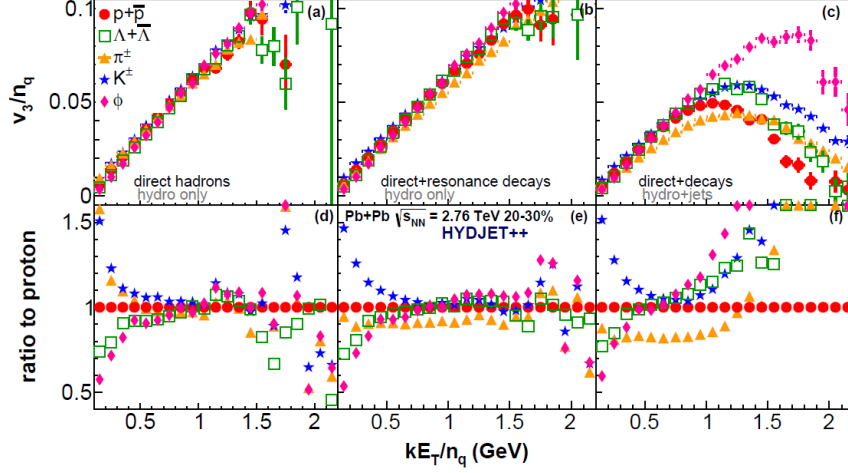
Figure 3.3: The HYDJET++ modeled kE_T/n_q quark scaling dependence of triangular flow v_3 for direct hadrons from soft component only (a), from hadrons produced in soft processes only (b) and from hadrons produced in both soft and hard processes in 20-30% centrality bin in Au+Au collisions at $\sqrt{s_{\mathrm{NN}}} = 200$ GeV [54]. Bottom row shows ratio with respect to $p + \bar{p}$, $(v_3/n_q)/(v_2^{p+\bar{p}}/3)$.
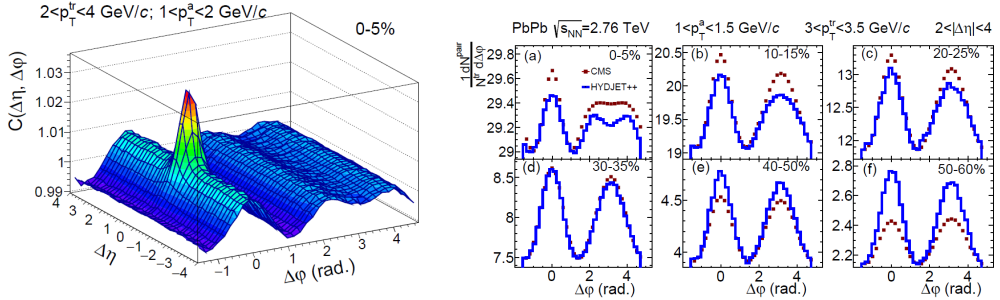
Figure 3.4: The two-particle angular correlation function $C(\Delta\eta, \Delta\varphi)$ modeled by the HYDJET++ using both elliptic and triangular flow in Pb+Pb collisions at $\sqrt{s_{\mathrm{NN}}} = 2.76$ TeV in the most central collisions (left). In the right graph, $\Delta\varphi$ dependence is shown in $2 < |\Delta\eta| < 4$ region together with CMS experimental data for six centrality bins 0-5%, 10-15%, 20-25%, 30-35%, 40-50% and 50-60%. Both graphs are taken from Ref. [119].

Possibility to turn on and off spatial and velocity modulation in the HYDJET++ allows one to study influence of geometric (spatial) and dynamical (momentum)

anisotropies on the development of the flow harmonics and femtoscopic radii[6]. For both elliptic and triangular harmonic it has been found that in Pb+Pb collisions at energy $\sqrt{s_{NN}} = 2.76$ TeV their shape is governed by dynamical anisotropies, however, for correct description geometric anisotropies are needed too. Effect of resonance decays has also been studied. It turns out that decays of resonances provide significant increase of the emitting areas. Effect of resonance decays in pion emission function can be seen in Fig. 3.5.
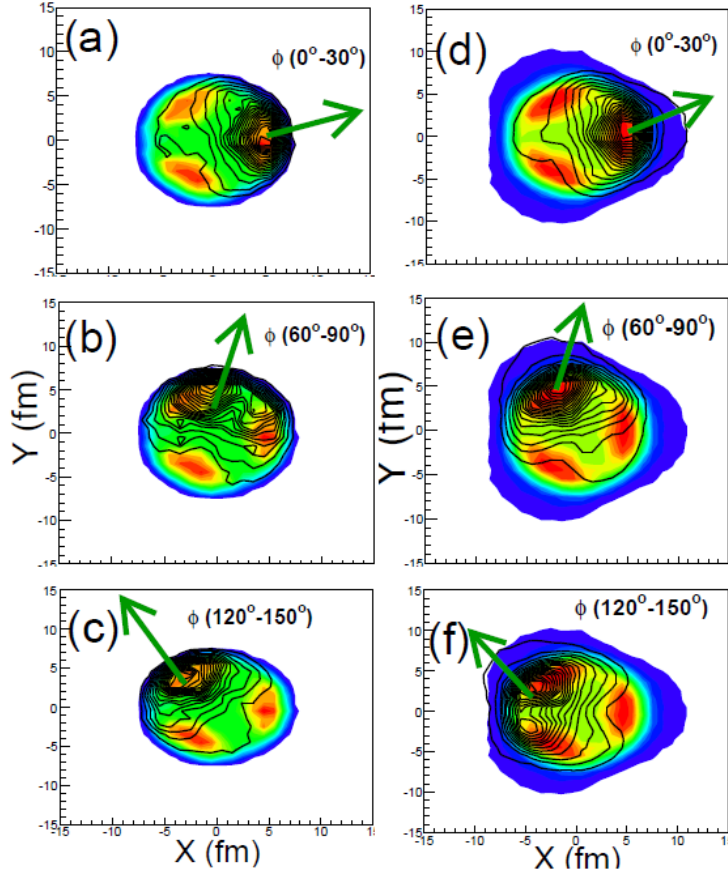
Figure 3.5: The HYDJET++ simulated pion emission function before (left column) and after (right column) decays of resonances in the transverse plane where only dynamical triangular anisotropy is considered. Simulation has been performed for Pb+Pb collisions at $\sqrt{s_{NN}} = 2.76$ TeV with centrality 20–30%. Colors correspond to the density of emitted pions and lines to the densities of pions emitted at the denoted angles. Figure is taken from Ref. [110].

Moreover, charm and beauty particles can be studied by the HYDJET++. It has been shown in Ref. [120] that HYDJET++ can describe p_T distributions of yield and elliptic flow of D^0, $D^\pm$, $D^{*\pm}$ and J/ψ at two different energies $\sqrt{s_{NN}} = 200$ GeV and $\sqrt{s_{NN}} = 2.76$ TeV corresponding to RHIC and LHC energies, respectively. Transverse momentum spectra of $D^\pm$, $D^{*\pm}$ and D^0 mesons can be seen in Fig. 3.6

---

[6]Femtoscopy is a technique of measuring short-range two-particle correlations as a function of relative momentum. Using 3-dimensional correlation analysis allows one to study $R_{out}, R_{side}, R_{long}$ parameters from which spatial and time information of the emitting source can be inferred [16].

and Fig. 3.7a shows $J/\psi(p_T)$ yield dependence at $\sqrt{s_{NN}} = 2.76$ TeV energy. In the $J/\psi(p_T)$ distribution, two HYDJET++ simulation lines represent two different thermal freeze-out temperatures used. It has been found that at RHIC energy thermal freeze-out of charm mesons occurs earlier than the thermal freeze-out of light hadrons while at LHC energy thermal freeze-out of D mesons happens at the same temperature as that for light mesons and only J/ψ freezes-out early. The difference can be explained by cross section of D mesons which becomes comparable to that of light mesons at LHC energy.

The most recent studies focus on B mesons in Pb+Pb collisions at energy $\sqrt{s_{NN}} = 5.02$ TeV and their energy losses in medium and forward-backward correlations. The HYDJET++ simulations imply that the energy losses of b quarks in matter completely dominate over the nuclear shadowing contribution for $p_T > 30$ GeV/c while for $p_T \sim 10$ GeV/c these effects are comparable (Fig. 3.7b). Radiative and collisional losses are found to be comparable to each other for B mesons. On the other hand, suppression of light hadrons occurs mainly due to radiative energy losses. The forward-backward pseudorapidity correlation of the average multiplicity of particles can also be described by HYDJET++ in Pb+Pb collisions at $\sqrt{s_{NN}} = 2.76$ TeV energy [121]. Hard jet component is observed to dominate over the soft one.
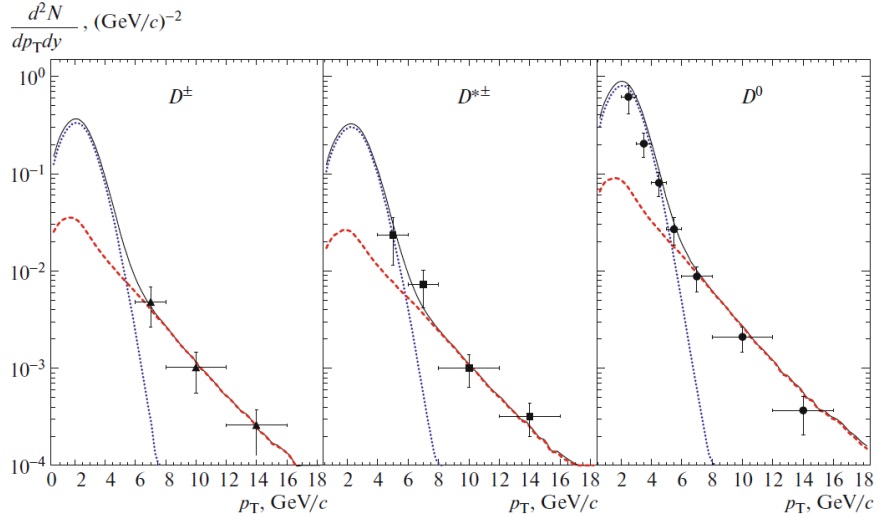
Figure 3.6: The HYDJET++ transverse-momentum distributions of $D^{\pm}$, $D^{*\pm}$ and D^0 mesons in the 0-20% most central Pb+Pb collisions at $\sqrt{s_{NN}} = 2.76$ TeV energy for the rapidity range $|y| < 0.5$ compared to the ALICE experimental data (solid points). Simulation parameters of inclusive hadrons have been used. Blue dotted curve and red dashed curve are soft and hard HYDJET++ components, respectively. Figure is taken from Ref. [120].

The HYDJET++ model is supposed to be used for high energies $\sqrt{s_{NN}} \gtrsim 10$ GeV simulations due to the local equilibrium assumption, however, it has been shown that p_T spectra of charged particles can be well simulated even for intermediate energies $\sqrt{s_{NN}} = 7.7$ GeV and $\sqrt{s_{NN}} = 11.5$ GeV in Au+Au collisions at the STAR experiment. The $\sqrt{s_{NN}} = 7.7$ GeV case can be seen in Fig. 3.8. Therefore description

$\dfrac{d^2N}{dp_T dy}$, $(\text{GeV}/c)^{-2}$

p_T, GeV/c

(a)

R_{AA}

p_T, GeV/c

(b)
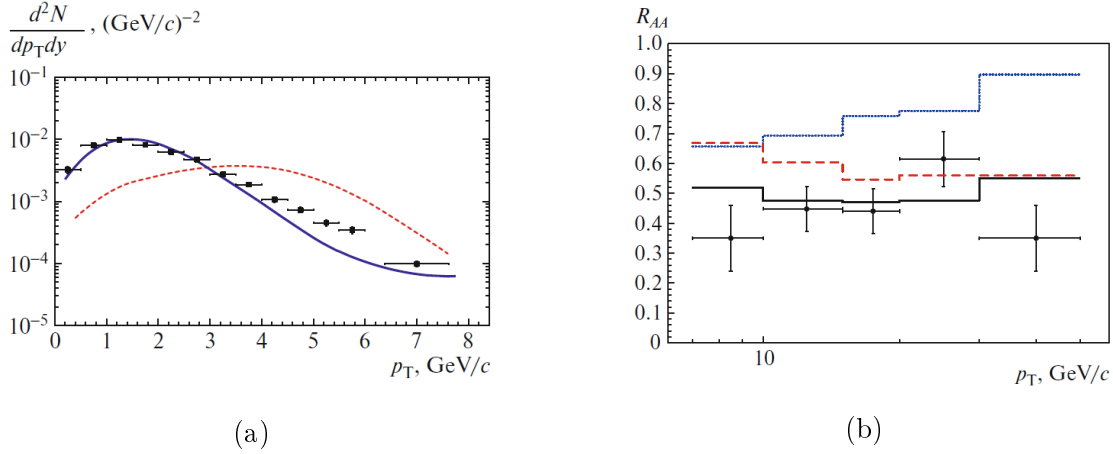
Figure 3.7: (a) J/ψ yield p_T distribution in 0-20% centrality interval of Pb+Pb collisions at the energy $\sqrt{s_{\text{NN}}} = 2.76$ TeV for the rapidity range $2.5 < y < 4$ compared to ALICE experimental data (solid points). The red dashed curve has been obtained with light meson freeze-out parameters while the blue solid curve with early thermal freeze-out ones [120]. (b) The HYDJET++ simulated nuclear modification factor R_{AA} dependence on p_T for charged B mesons in Pb+Pb collisions at energy $\sqrt{s_{\text{NN}}} = 5.02$ TeV for the rapidity range $|y| < 2.4$ [122]. Points are the CMS experimental data and histograms are the HYDJET++ simulation results. The solid histogram takes into account both nuclear shadowing and energy losses, the dashed histogram only energy losses and the dotted histogram only nuclear shadowing.

of charged particles spectra might be possible even at lower energies which will be achieved in Nuclotron-based Ion Collider fAcility (NICA) in Russia with planned $\sqrt{s_{\text{NN}}} = 4 - 11$ GeV energy range [123].
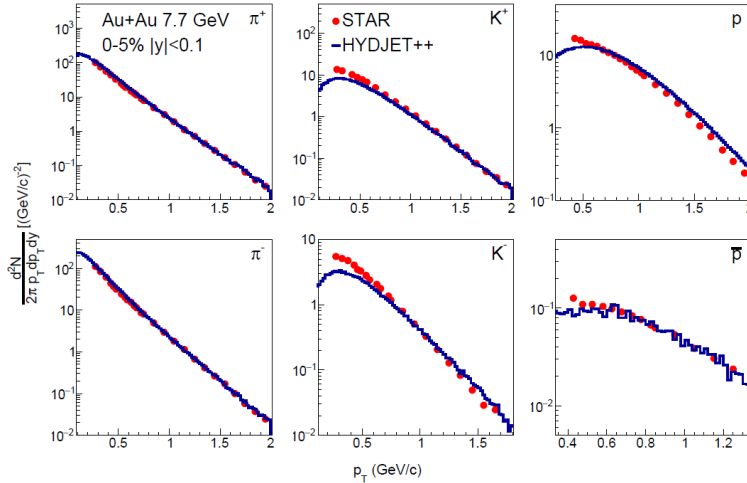
Figure 3.8: Comparison of the HYDJET++ simulated mid-rapidity $|y| < 0.1$ p_T spectra of $\pi^+, \pi^-, K^+, K^-, p$ and $\bar{p}$ in Au+Au collisions at $\sqrt{s_{\text{NN}}} = 7.7$ GeV to STAR experimental data in 0-5% centrality region. Figure is taken from [124].

In summary, HYDJET++ can describe remarkably well many distributions of var-

ious particles as well as differentiate contributing effects. In this thesis, results of charged hadrons and charm mesons at the highest RHIC and LHC energies have been reproduced and extended by previously not studied energy $\sqrt{s_{\mathrm{NN}}} = 5.02$ TeV in Pb+Pb collisions.

Chapter 4

Simulation of Au+Au and Pb+Pb Collisions

In this chapter, author's HYDJET++ simulation results[1] of Au+Au collisions at $\sqrt{s_{\mathrm{NN}}} = 200$ GeV and Pb+Pb collisions at $\sqrt{s_{\mathrm{NN}}} = 2.76$ and 5.02 TeV are presented. Simulation at energies $\sqrt{s_{\mathrm{NN}}} = 200$ GeV and $\sqrt{s_{\mathrm{NN}}} = 2.76$ TeV is an update of previous results and is performed as validation of the used HYDJET++ 2.4 version. Results of the Pb+Pb collisions at $\sqrt{s_{\mathrm{NN}}} = 5.02$ TeV for charged and charm particles are computed here for the first time. Significant part of this work has been conducted during author's exchange stay at the University in Oslo where author benefited from personal communication with one of the HYDJET++ model contributor, Prof. Larissa Bravina, who is simultaneously author's supervisor.

The HYDJET++ simulator is controlled by the input parameters which are stored in RunInputHydjet file. Every version of the HYDJET++ comes with already tuned or suggested sets of parameters for specific collision energies. In the case of 2.4 version it is Au+Au collisions at $\sqrt{s_{\mathrm{NN}}} = 200$ GeV, Pb+Pb collisions at $\sqrt{s_{\mathrm{NN}}} = 2.76$ and Pb+Pb collisions at $\sqrt{s_{\mathrm{NN}}} = 5.02$ TeV. First two of them have already been tuned to inclusive charged hadrons[2] experimental data $h^{\pm}$ while the last one for the highest energy uses just extrapolated parameters from the two previous ones. Overview of all the parameters can be found in the HYDJET++ documentation [88]. It has been found that the most influential parameters for the production of different species of the particles are:

- temperature at chemical freeze-out T_{ch},

- temperature at thermal freeze-out T_{th},

- minimal p_T of parton-parton scattering in PYTHIA event $p_{T,min}$,

- initial QGP temperature for central Pb+Pb collisions in midrapidity T_0.

---

[1]All graphs shown in this chapter except of Fig. 4.9 have been produced solely by the author of this thesis.

[2]Inclusive charged hadrons $h^{\pm}$ are $\pi^{\pm}$, $K^{\pm}$, protons p and antiprotons $\bar{p}$.

- maximal longitudinal fluid flow rapidity at thermal freeze-out η_{max},

- maximal transverse fluid flow rapidity at thermal freeze-out for central collisions ρ_{max} and

- charmness enhancement factor γ_c.

When $\gamma_c = -1$ is set, γ_c is calculated from charm balance equation. This option has not been used for charm particle spectra. For all other physical parameters their default value has been used if not stated otherwise[3].

The HYDJET++ simulation tool is freely accessible via internet [125] in an archive format. In order to run the HYDJET++ one needs C++ and Fortran compilers and CERN ROOT libraries. Simulation procedure starts by setting the input parameters in the RunInputHydjet and modifying RunHadronSource.cxx file for a ROOT tree output or RunHadronSourceHisto.cxx file for a ROOT histogram output. In the RunHadronSource.cxx and RunHadronSourceHisto.cxx the user chooses the saved data and both of the files need to be compiled and run separately.

All the computational simulations have been performed on the high-performance computing cluster Saga provided by the Norwegian e-infrastructure for Research & Education UNINETT Sigma2 [126]. Saga has got 9824 available computational cores and computation time has to be requested. The HYDJET++ computation time differs for different set of parameters. Simulation times needed to simulate 100 000 events are listed in Tab. 4.1 together with $p_{T,min}$ parameter which separates soft (fast) and hard (slow) part of the simulation. Demands on the computation time rise with the increasing collision energy $\sqrt{s_{NN}}$, decreasing $p_{T,min}$ and with more central collisions. Because the slow jet part dominates above the $p_{T,min}$ threshold, acquiring high statistics in high p_T region is time demanding.

The numbers of simulated events used for all the studied distributions in Au+Au collisions at $\sqrt{s_{NN}} = 200$ GeV and Pb+Pb collisions at $\sqrt{s_{NN}} = 2.76$ and 5.02 TeV are listed in Tab. A.1, B.1 and C.1 in the appendices A, B and C, respectively. The numbers of simulated events are uniformly distributed in the shown centrality intervals.

4.1   Au+Au at $\sqrt{s_{NN}} = 200$ GeV

It has been shown in previous studies [127] that for the Au+Au collisions at $\sqrt{s_{NN}} = 200$ GeV charm D mesons and charmonia follow the same evolution pattern and can be reproduced with the same set of parameters which are different from the ones used for inclusive charged hadrons $h^{\pm}$. Particularly, the thermal freeze-out temperature for charm mesons $T_{th}^{c} = 0.165$ GeV is different from that of charged hadrons $T_{th}^{h^{\pm}} = 0.1$ GeV. The same behavior is reproduced in this thesis. Simulation of charged hadrons has been done using the tuned set of parameters for Au+Au collisions at

---

[3]Note that in the default settings parameters needed for charm production (thermal charm production and full particle history from PYTHIA) are turned off.

$\sqrt{s_{NN}}$ [TeV]	particle set	$p_{T,min}$ [GeV/c]	centrality range	t [h]
0.2	$h^{\pm}$	3.55	0-40%	41
0.2	$D, J/\psi$	3.55	0-40%	34
2.76	$h^{\pm}, D$	8.2	0-40%	91
2.76	J/ψ	3	0-40%	1755
5.02	$h^{\pm}, D$	10	0-50%	109
5.02	J/ψ	5	0-20%	1720

Table 4.1: Overview of the simulation duration t for 100 000 events processed on one core for different setups. For each collision energy $\sqrt{s_{NN}}$, particle set, simulation parameter $p_{T,min}$ and simulation centrality range is shown.

system	Au+Au		Pb+Pb			
$\sqrt{s_{NN}}$ [TeV]	0.2		2.76		5.02	
particle set	$h^{\pm}$	$D, J/\psi$	$h^{\pm}, D$	J/ψ	$h^{\pm}, D$	J/ψ
T_{ch} [GeV]	0.165	0.165	0.165	0.165	0.165	0.165
T_{th} [GeV]	0.1	0.165	0.105	0.165	0.105	0.165
$p_{T,min}$ [GeV/c]	3.55	3.55	8.2	3	10	5
T_0 [GeV]	0.3	0.3	1	1	1.1	1.1
η_{max}	3	1.1	4.5	2.3	4.5	2.3
ρ_{max}	1.1	0.5	1.265	0.6	1.35	0.6
γ_c	-1	7	11.5	11.5	15	15

Table 4.2: List of the HYDJET++ parameters used in Au+Au collisions at $\sqrt{s_{NN}} = 200$ GeV and in Pb+Pb collisions at $\sqrt{s_{NN}} = 2.76$ and 5.02 TeV for charged hadrons $h^{\pm}$ and charm hadrons J/ψ and D.

$\sqrt{s_{NN}} = 200$ GeV delivered with the HYDJET++ distribution. Parameters for the charm particles have been taken from Ref. [127]. Summary of the most important parameters with the used values can be seen in Tab. 4.2. The section is divided into two subsections according to the used set of parameters followed by discussion of the results.

4.1.1 $h^{\pm}$ Distributions

For charged hadrons, yield, pseudorapidity η and elliptic flow v_2 transverse momentum p_T distributions have been studied. The reproduced transverse momentum p_T and pseudorapidity η spectra of charged hadrons for the Au+Au collisions at $\sqrt{s_{NN}} = 200$ GeV for different centralities can be seen in Fig. 4.1. The simulation result is compared to the experimental data from STAR and BRAHMS experiments. Parameters for charged hadrons $h^{\pm}$ from Tab. 4.2 have been used.

Simulated elliptic flow v_2 of charged hadrons in the Au+Au collisions at $\sqrt{s_{NN}} = 200$

GeV is shown in Fig. 4.2. Special sets[4] of $\delta = 0.15$, $\varepsilon = 0.07$ parameters for 0-10% centrality region and $\delta = 0.28$, $\varepsilon = 0.11$ parameters for 10-20% centrality region involving v_2 simulation have been used. However, both sets overestimate the data by a factor of two and to underline this overestimation the scaling by the factor of 0.5 has been used in the graphs. This has been found out to be the HYDJET++ 2.4 version problem. The same distributions have been accurately simulated by the HYDJET++ 2.1 version with $\delta = 0.15$, $\varepsilon = 0.07$ parameters for 0-10% centrality region and $\delta = 0.23$, $\varepsilon = 0.10$ parameters for 10-20% centrality region and the distributions are shown in Fig. 4.3. Since this problem occurs only in v_2 distributions at $\sqrt{s_{\mathrm{NN}}} = 200$ GeV for charged particles and does not affect any other distributions, no deeper analysis of the origin of the problem has been conducted and authors of the model have been informed.
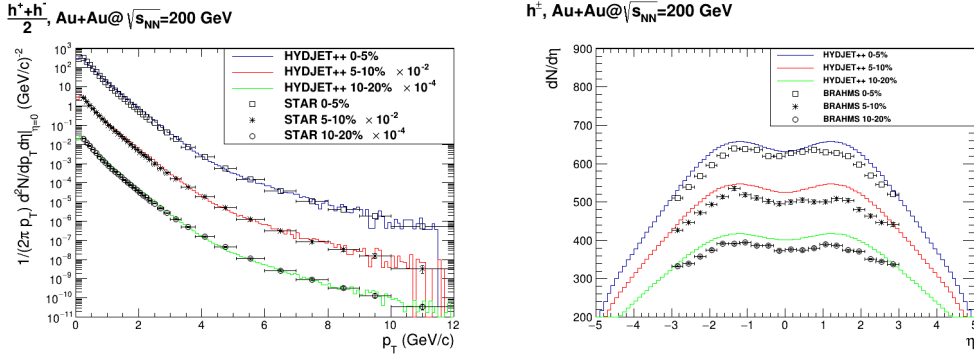
Figure 4.1: THIS WORK: The HYDJET++ simulated transverse momentum p_T (left) and pseudorapidity η (right) histogram distributions of charged hadrons $h^{\pm}$ in Au+Au collisions at $\sqrt{s_{\mathrm{NN}}} = 200$ GeV for three different centralities compared to the STAR [128] and BRAHMS [129] experimental data.
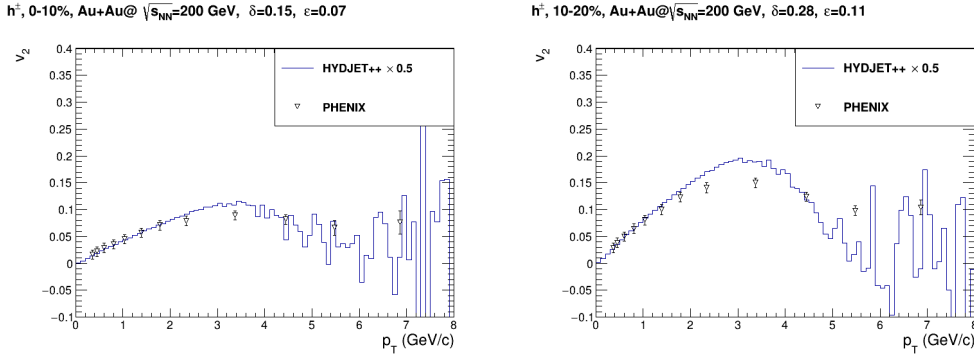
Figure 4.2: THIS WORK: The HYDJET++ 2.4 version simulated elliptic flow v_2 histogram distributions for 0-10% (left) and 10-20% (right) centrality region of Au+Au collisions at $\sqrt{s_{\mathrm{NN}}} = 200$ GeV compared to the PHENIX experimental data [130]. Used δ and ε parameters are shown in the graph labels.

---

[4]The HYDJET++ default values are $\delta = 0.10$, $\varepsilon = 0.05$ for 0-5% centrality, $\delta = 0.24$, $\varepsilon = 0.10$ for 5-10% centrality and $\delta = 0.28$, $\varepsilon = 0.11$ for 10-20% centrality region.
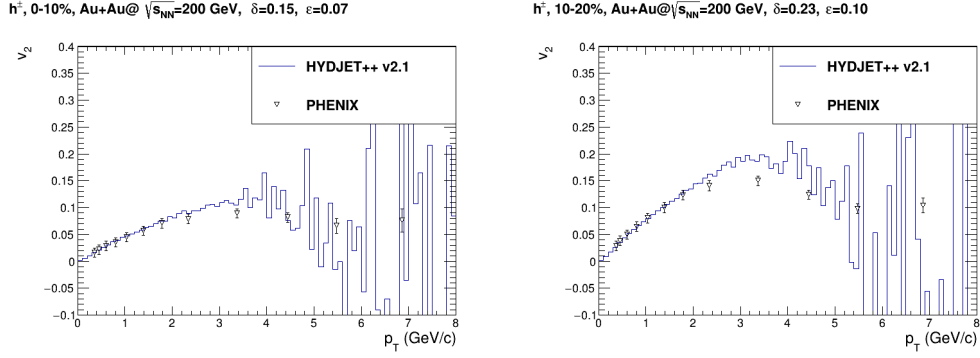
Figure 4.3: THIS WORK: The HYDJET++ 2.1 version simulated elliptic flow v_2 histogram distributions for 0-10% (left) and 10-20% (right) centrality region of Au+Au collisions at $\sqrt{s_{\mathrm{NN}}} = 200$ GeV compared to the PHENIX experimental data [130]. Used δ and ε parameters are shown in the graph labels.

4.1.2 J/ψ and D Meson Distributions

For simulation of J/ψ and D meson distributions, parameters for charm mesons shown in Tab. 4.2 have been used. In Fig. 4.4, the HYDJET++ transverse momentum distributions of D^0 and J/ψ mesons compared to the experimental data can be seen. In both graphs soft and hard part have been extracted. D^0 modification factor R_{AA} and elliptic flow v_2 shown in Fig. 4.5 together with experimental data have been studied for the first time. To compute the D^0 R_{AA}, number of the binary collisions $\langle N_{\mathrm{coll}} \rangle = 941.2 \pm 26.3$ and Levy fit p+p reference from [131] have been used. Uncertainties have not been calculated.

In case of D mesons, an issue in the efficiency calculation has been discovered in the STAR experimental data from 2010/11 [131] and therefore a corrected set of the data together with a completely new data from 2014 has been released in 2014 [132]. Used parameters have been tuned to the old data and the results are published in Ref. [120]. Here, comparison to the new data is offered. In order to match the data for D mesons and J/ψ p_T distributions simultaneously, impact of different values of the γ_c parameter is studied. Results for $\gamma_c = 6, 5, 4$ can be seen in Fig. 4.6, 4.7 and 4.8, respectively.

4.1.3   Discussion of Au+Au at $\sqrt{s_{\mathrm{NN}}} = 200$ GeV Results

The HYDJET++ simulation results for inclusive charged particles match the data in p_T distribution perfectly. Description of the data in pseudorapidity distribution is not as impressive as in p_T case but is good enough. It has been found that, even after setting δ and ε parameters manually, HYDJET++ 2.4 version can not correctly reproduce observed elliptic flow and overestimates the data by the factor of two. This issue does not occur in HYDJET++ 2.1 version and tuning of the azimuthal anisotropy parameter in HYDJET++ 2.4 version for $\sqrt{s_{\mathrm{NN}}} = 200$ GeV energy is needed. This effect has not been observed at higher energies discussed in next chapters and no tuning attempt has been done in this thesis.
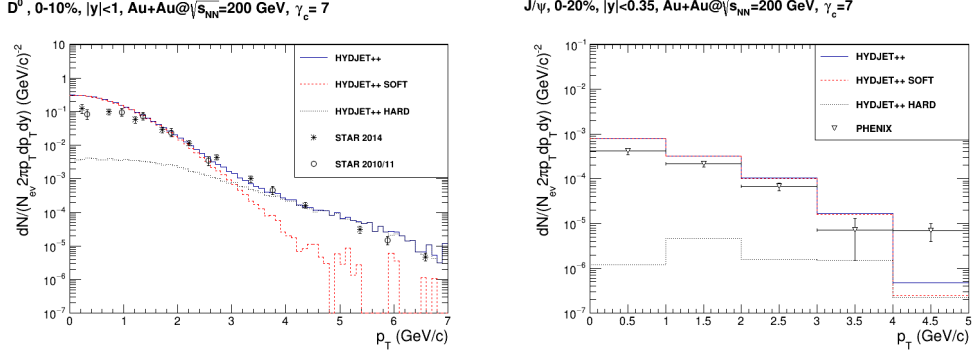
Figure 4.4: THIS WORK: Comparison of the HYDJET++ simulated histograms of transverse momentum distribution p_T for D^0 (left) and J/ψ (right) mesons to the STAR [132] and PHENIX [133] data in Au+Au collisions at $\sqrt{s_{\mathrm{NN}}} = 200$ GeV. Centrality region 0-10% and 0-20% of the most central collisions have been used for D^0 and J/ψ, respectively. Soft and hard component have been extracted from HYDJET++.
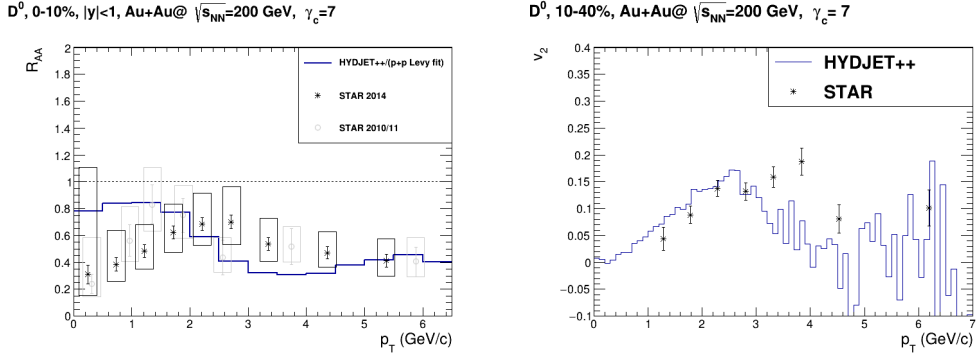
Figure 4.5: THIS WORK: Comparison of the HYDJET++ simulated histograms of nuclear modification factor R_{AA} (left) and elliptic flow v_2 (right) for D^0 mesons to the STAR R_{AA} [132] and v_2 [134] data in Au+Au collisions at $\sqrt{s_{\mathrm{NN}}} = 200$ GeV. Centrality region 0-10% and 10-40% of the most central collisions have been used for R_{AA} and v_2, respectively.

As mentioned above, the HYDJET++ D^0 p_T distribution has been compared to the new D^0 meson STAR data [132] for the first time in this thesis and overestimation of the data is observed in $p_T \lesssim 1.5$ GeV/c region. This directly leads to overestimation of D^0 R_{AA} in low p_T region in Fig. 4.5. It is observed that description of the D^0 elliptic flow is valid only for $p_T \leq 3$ GeV/c.

The HYDJET++ description of J/ψ transverse momentum distribution in Fig. 4.4 has been done with the same HYDJET++ parameters as for D^0. Clear overestimation of the experimental data can be seen in $p_T \leq 4$ GeV/c region. However, the same parameters have been used for very precise description of J/ψ transverse momentum distribution in one of the previous studies [127] which can be seen in Fig. 4.9. This results in Ref. [127] has been produced with the HYDJET++ 2.1 version.
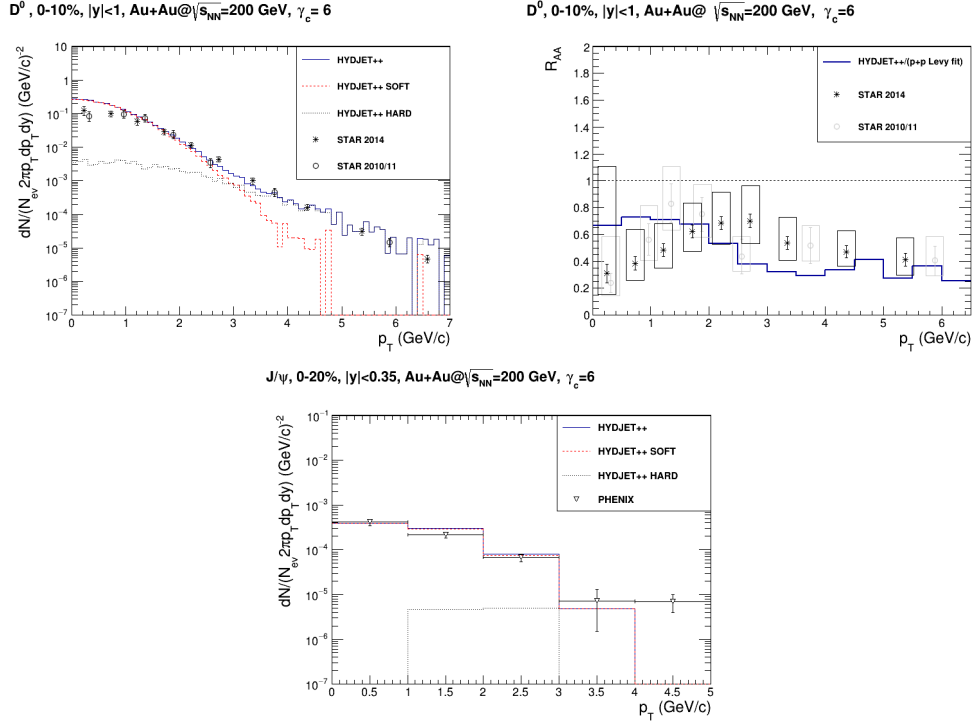
Figure 4.6: THIS WORK: The same D^0 and J/ψ meson distributions as in Fig. 4.4 and Fig. 4.5 with modified $\gamma_c = 6$ parameter.
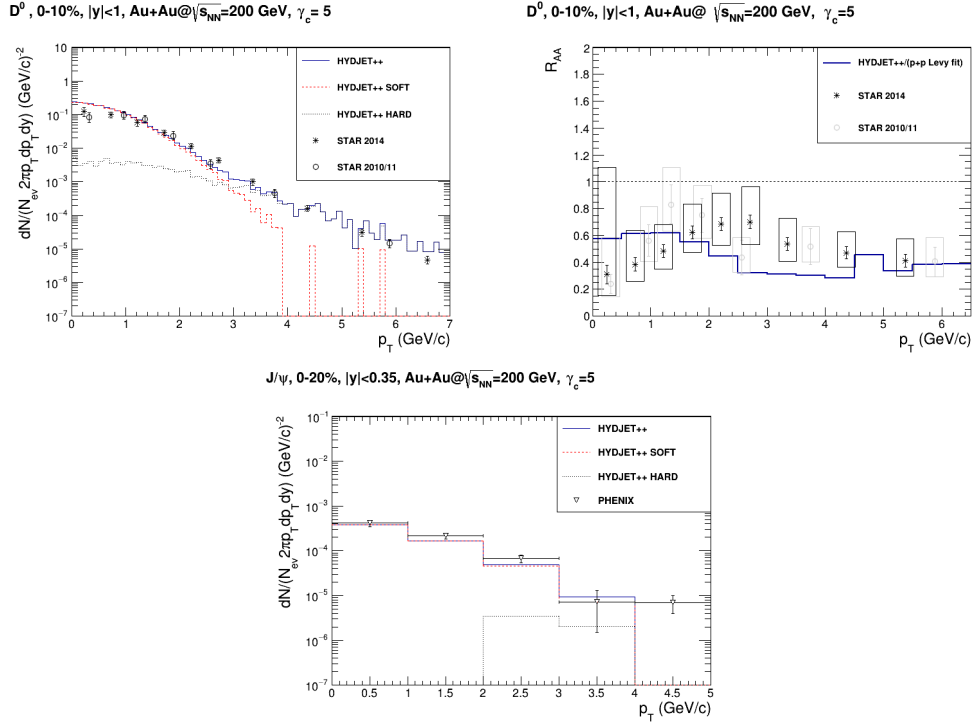
Figure 4.7: THIS WORK: The same D^0 and J/ψ meson distributions as in Fig. 4.4 and Fig. 4.5 with modified $\gamma_c = 5$ parameter.
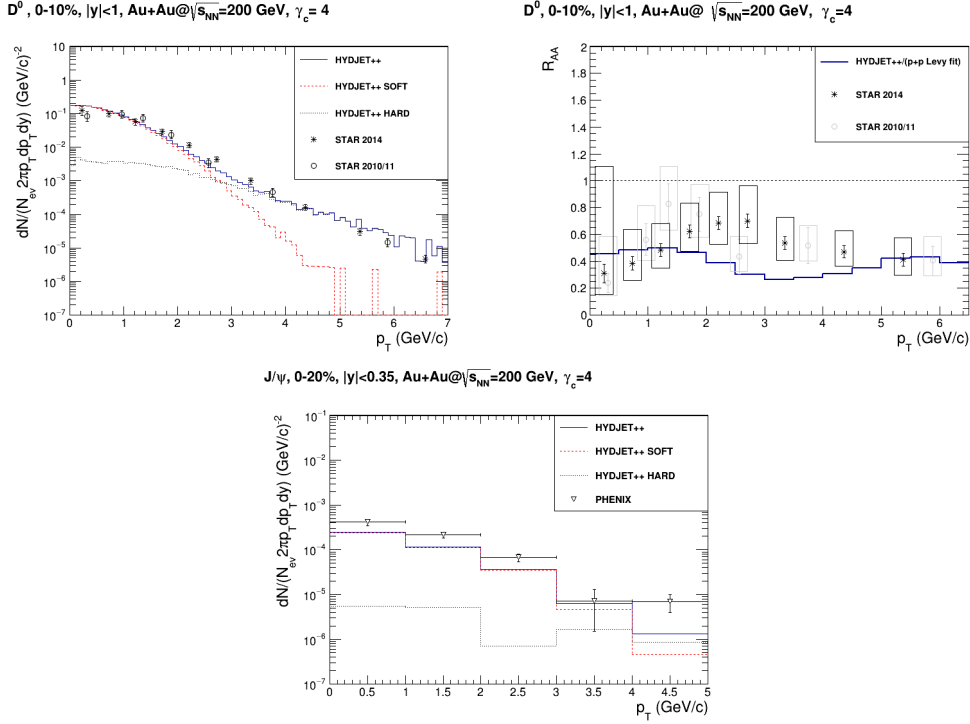
Figure 4.8: THIS WORK: The same D^0 and J/ψ meson distributions as in Fig. 4.4 and Fig. 4.5 with modified $\gamma_c = 4$ parameter.

In order to describe D^0 and J/ψ experimental data better, lowering γ_c parameter has been suggested. It can be seen in Fig. 4.6 and 4.7 that better description of experimental results of J/ψ p_T distribution has been achieved with $\gamma_c = 6$ and $\gamma_c = 5$ while $\gamma_c = 4$ underestimates the data in all the p_T range (Fig. 4.8). However, using $\gamma_c = 6$ or 5 does not lead to the desired goal of correct simultaneous description of both spectra in all the studied p_T range. The HYDJET++ overestimates the D^0 p_T distribution in $p_T \lesssim 1.5$ GeV/c region in all the four studied cases.

It can be concluded that the HYDJET++ 2.1 version differs from the 2.4 version and careful tuning of the parameters for the HYDJET++ 2.4 version in Au+Au collisions at $\sqrt{s_{NN}} = 200$ GeV is needed to reproduce the experimental data better. The tuning has not been performed in the thesis. Despite that, the HYDJET++ 2.4 simulation results agree with previous results that the model matches the data best when the thermal freeze-out temperature T_{th} is the same for D and J/ψ mesons and different for charged hadrons $h^\pm$ in Au+Au collisions at $\sqrt{s_{NN}} = 200$ GeV.

4.2   Pb+Pb at $\sqrt{s_{NN}} = 2.76$ TeV

It has been shown that, unlike Au+Au collisions at $\sqrt{s_{NN}} = 200$ GeV, in Pb+Pb collisions at $\sqrt{s_{NN}} = 2.76$ TeV experimental results can be reproduced with HYD-JET++ tool by using one set of parameters for charged hadrons $h^\pm$ and D mesons and different set for J/ψ quarkonium [135]. Both sets of the used simulation parameters are listed in Tab. 4.2. Observed change of the thermal freeze-out temperature
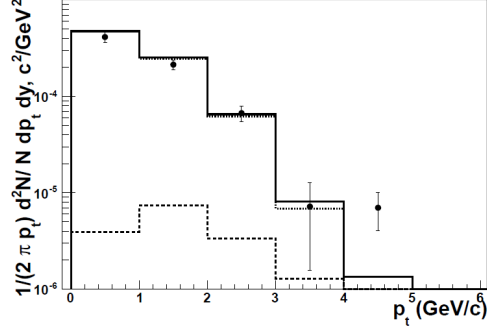
Figure 4.9: J/ψ transverse momentum distribution taken from Ref. [127].

of the D mesons can be explained by cross section of the D mesons becoming comparable to that of light mesons at LHC energy while interaction cross section of the J/ψ mesons remains significantly smaller than that of the D mesons. Charm enhancement factor $\gamma_c = 11.5$ is used for D mesons as well as for J/ψ. The section is divided into two subsections according to the used set of parameters followed by discussion of the results.

4.2.1 $h^\pm$ and D Meson Distributions

In this section, the HYDJET++ simulated p_T distribution results of charged particles $h^\pm$ have been studied for yield and flow coefficients v_2, v_3, v_4, v_5, that of the D^0 meson for yield and elliptic flow, that of the D^+ meson for yield and that of the $D^\pm$ for v_2 observable.
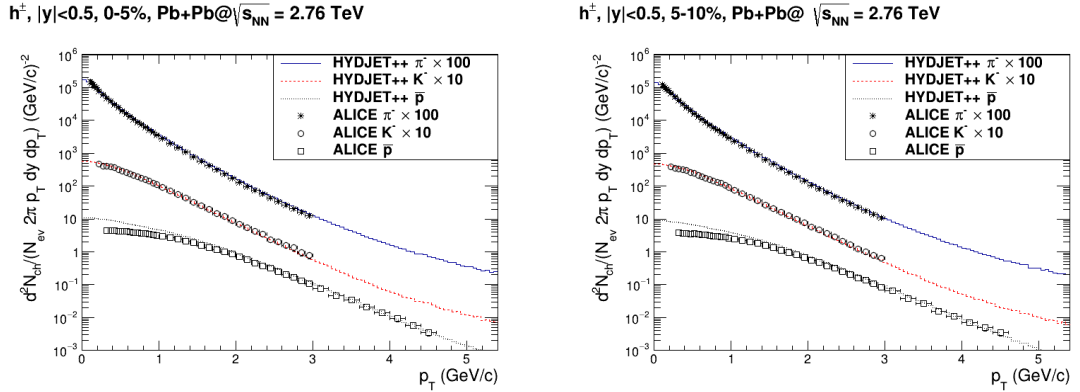
Figure 4.10: THIS WORK: Comparison of the HYDJET++ π^-, K^- and antiproton $\bar{p}$ transverse momentum p_T histograms for the Pb+Pb collisions at $\sqrt{s_{\mathrm{NN}}} = 2.76$ TeV with the ALICE experimental data [136] in 0-5% and 5-10% centrality bins.

The HYDJET++ transverse momentum results for various centralities[5] with rapidity cut $|y| < 0.5$ of π^-, K^- and antiproton $\bar{p}$ particles can be found in Fig. B.1 in appendix B together with the ALICE experimental data [136]. Flow v_2, v_3, v_4, v_5

_____

[5]0-5%, 5-10%, 10-20%, 20-30%, 30-40%, 40-50% centrality bins have been studied.

p_T distributions of $h^\pm$ in 10-20%, 20-30%, 30-40%, 40-50% centrality bins can be found in Fig. B.2 and B.3. The most central distributions 0-5% and 5-10% of the yield distributions and 5-10% centrality v_2, v_3, v_4, v_5 p_T distributions are shown in Fig. 4.10 and 4.11, respectively. Simulation results of collective flow coefficients have been compared to the ATLAS [137] data. In the collective flow graphs, the flow coefficients have been computed in two ways. In the first method, the flow coefficients v_2, v_4, v_5 are calculated with respect to the elliptic flow true reaction plane generated by HYDJET++ and triangular flow has got its own true reaction plane, while in the second method, the reaction plane for every coefficient is calculated as in experiment. This implies that the description of v_2 and v_3 with respect to the HYDJET++ reaction plane is accurate while v_4 and v_5 is inaccurate because of the lack of the intrinsic reaction planes. When using the reaction plane calculated as in the experiment, all flow coefficients are calculated with respect to their own reaction plane. Experimental procedure of the reaction plane computation follows in the next paragraph.
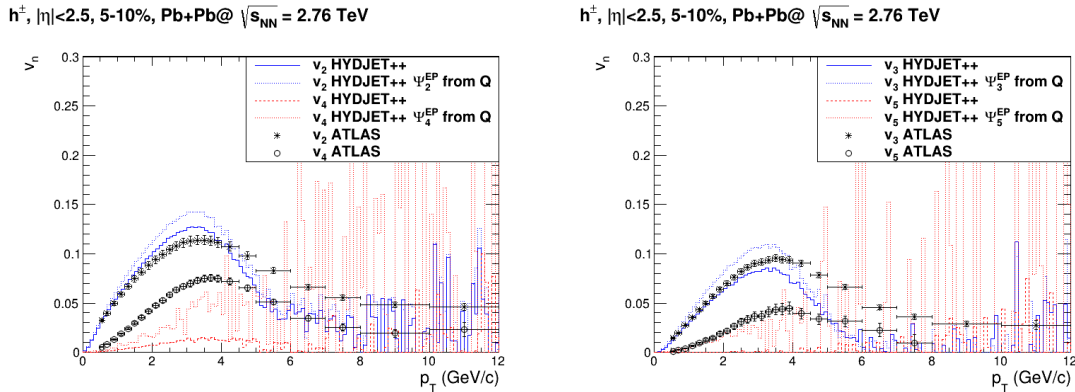
Figure 4.11: THIS WORK: Comparison of the HYDJET++ simulated flow coefficients v_2, v_4 (left) and v_3, v_5 (right) p_T distribution histograms of all the charged hadrons $h^\pm$ for the Pb+Pb collisions at $\sqrt{s_{\mathrm{NN}}} = 2.76$ TeV with the ATLAS experimental data [137] in 5-10% centrality bin. Computation has been done with respect to the HYDJET++ true reaction plane (solid and dashed lines) and with respect to the estimated reaction plane from the event plane using $\vec{Q}_n$ (dotted lines).

In an experiment, the true reaction plane has to be estimated by the event plane. The event plane angle of the nth-order, Ψ_n, is defined as the direction of the flow vector [137]

$$\vec{Q}_n = (Q_{x,n}, Q_{y,n}) = \left(\Sigma E_T \cos n\phi, \Sigma E_T \sin n\phi\right), \tag{4.1}$$

$$\tan n\Psi_n = \frac{Q_{y,n}}{Q_{x,n}}, \tag{4.2}$$

where $E_T = \sqrt{p_T^2 + m^2}$ is the transverse energy, ϕ is the measured particle angle and the sum ranges over all the particles. The coefficient v_n is calculated by correlating

the tracks with the event plane angle Ψ_n and is corrected for resolution by the two-subevents method

$$v_n\{\text{EP}\} = \frac{v_n^{\text{obs}}}{\text{Res}\{n\Psi_n\}} = \frac{\langle \cos n(\phi - \Psi_n)\rangle}{\sqrt{\langle \cos n(\Psi_n^{\text{P}} - \Psi_n^{\text{N}})\rangle}}, \tag{4.3}$$

where $n\Psi_n^{\text{P}}$ is angle of $\vec{Q}_n^{\text{P}}$ for tracks with $\eta > 0$ and $n\Psi_n^{\text{N}}$ that for tracks with $\eta < 0$ and the $\langle \ldots \rangle$ brackets denote average over all the events.

The HYDJET++ simulated p_T distributions of D^0 and D^+ yields in 0-10% and 30-50% can be found in Fig. 4.12 and 4.13, respectively. Elliptic flow p_T distributions of D^0 in 0-10%, 10-30%, 30-50% centrality bins and $D^\pm$ in 30-50% centrality bin are shown in Fig. 4.14 and 4.15, respectively. The D meson HYDJET++ histograms are compared to the ALICE [138, 139] experimental data.
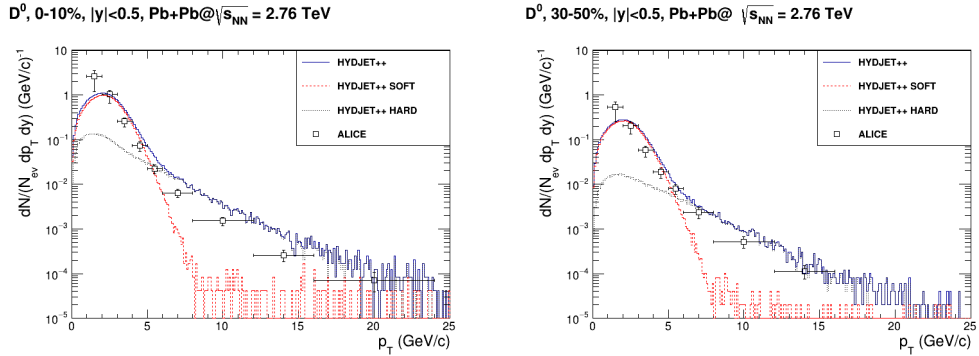
Figure 4.12: THIS WORK: Comparison of the HYDJET++ simulated p_T histograms of the D^0 meson yield N to the ALICE experimental data [138] in Pb+Pb collisions at $\sqrt{s_{\text{NN}}} = 2.76$ TeV for centralities 0-10% (left) and 30-50% (right). Soft and hard HYDJET++ component have been extracted.
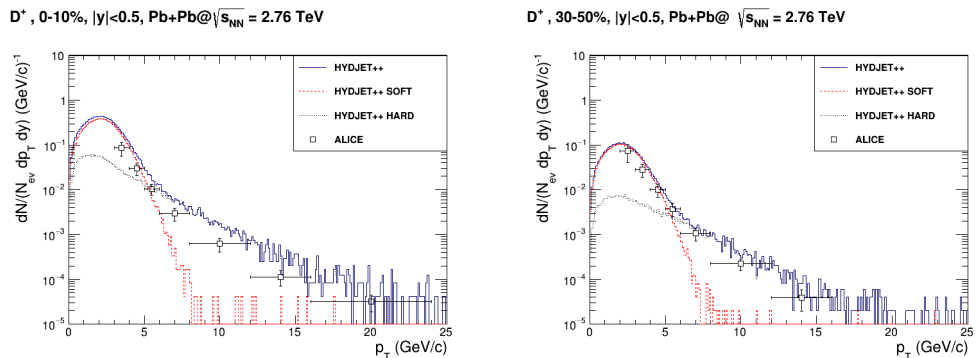
Figure 4.13: THIS WORK: Comparison of the HYDJET++ simulated p_T histograms of D^+ meson yield N to ALICE experimental data [138] in Pb+Pb collisions at $\sqrt{s_{\text{NN}}} = 2.76$ TeV for centralities 0-10% (left) and 30-50% (right). Soft and hard HYDJET++ component have been extracted.
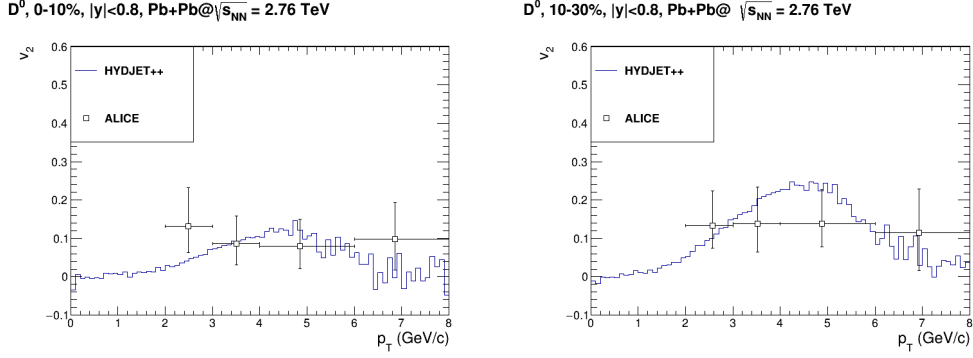
Figure 4.14: THIS WORK: Comparison of the HYDJET++ simulated p_T histograms of the D^0 elliptic flow v_2 to the ALICE experimental data [139] in Pb+Pb collisions at $\sqrt{s_{\mathrm{NN}}} = 2.76$ TeV for centralities 0-10% (left) and 10-30% (right).
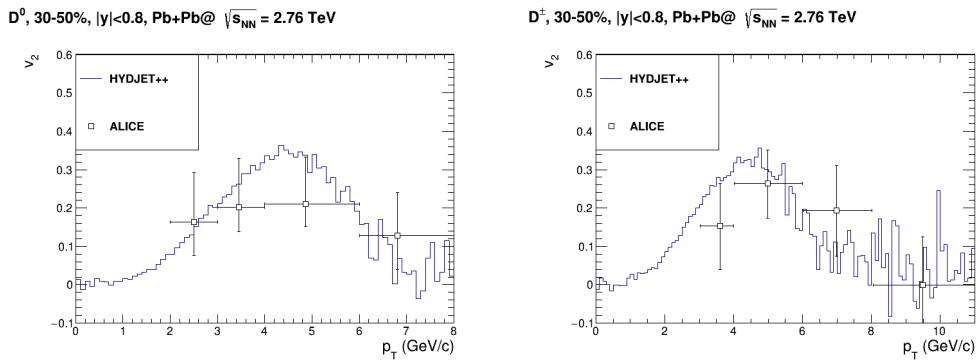
Figure 4.15: THIS WORK: Comparison of the HYDJET++ simulated p_T histograms of the D^0 (left) and the $D^\pm$ (right) elliptic flow v_2 to the ALICE experimental data [139] in Pb+Pb collisions at $\sqrt{s_{\mathrm{NN}}} = 2.76$ TeV for 30-50% centrality region.

4.2.2 J/ψ Distributions

The HYDJET++ simulated p_T distribution of the J/ψ quarkonium in 0-20% and 20-40% centrality regions with $2.5 < y < 4$ rapidity cut together with the ALICE experimental data [140] can be seen in Fig. 4.16. In Fig. 4.17, elliptic flow of J/ψ in 20-40% centrality bin with the same rapidity cut is shown. Note that the corresponding parameters from Tab. 4.2 have been used.

4.2.3 Discussion of Pb+Pb at $\sqrt{s_{\mathrm{NN}}} = 2.76$ TeV Results

The HYDJET++ simulation results of the charged hadrons $h^\pm$ yield follow the experimental data within the uncertainties in all the five centrality ranges except of the $\bar{p}$ which is overestimated by the model in most of the centralities in $p_T < 1$ GeV/c region. In the elliptic flow histograms, regardless the centrality, HYDJET++ accurately describes the data in $p_T < 2$ GeV/c region, then overestimates the data in $2 < p_T < 4.5$ GeV/c and around $p_T \sim 4.5$ GeV/c, where hard jet part starts to be
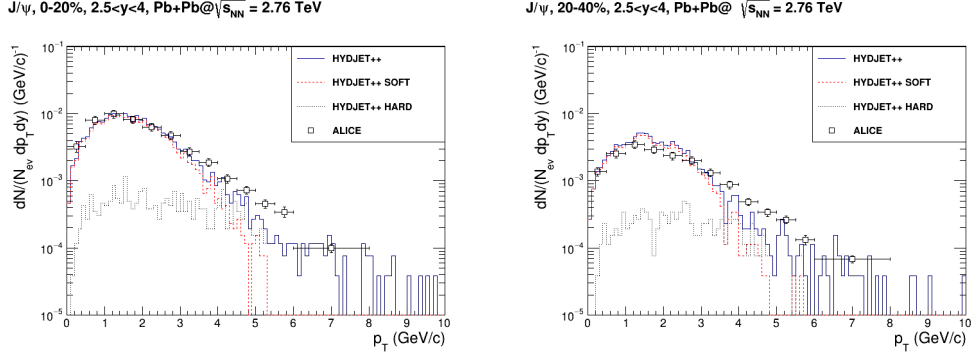
Figure 4.16: THIS WORK: Comparison of the HYDJET++ simulated p_T histograms of the J/ψ quarkonium yield N to the ALICE experimental data [140] in Pb+Pb collisions at $\sqrt{s_{NN}} = 2.76$ TeV. Centrality regions 0-20% (left) and 20-40% (right) with $2.5 < y < 4$ rapidity cuts have been studied and the soft and hard HYDJET++ components have been extracted.
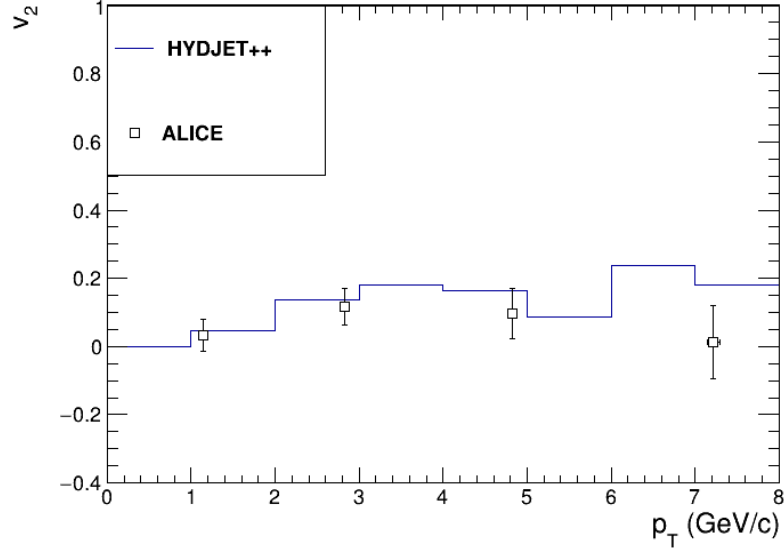
Figure 4.17: THIS WORK: Comparison of the HYDJET++ simulated p_T histograms of the J/ψ quarkonium elliptic flow v_2 and the ALICE experimental data [141] in Pb+Pb collisions at $\sqrt{s_{NN}} = 2.76$ TeV. Centrality region 20-40% with $2.5 < y < 4$ rapidity cut has been studied.

dominant, significantly underestimates the data. No significant difference between the results obtained from the true reaction plane and the estimated reaction plane from $\vec{Q}$ has been observed. In case of the triangular flow v_3, the true reaction plane histograms match the data better. Results of the v_4 obtained from the estimated reaction plane using $\vec{Q}$ match the data better than the ones obtained with respect to the true v_2 reaction plane. This is natural because of the lacking intrinsic v_4 reaction plane in HYDJET++. Interestingly, this is not the case in 40-50% centrality bin. Here, correlation between v_2 and v_4 reaction planes is observed which is supported

by theory at high p_T, $v_4 \sim \frac{1}{2}v_2^2$ [142]. Last, v_5 computed with respect to the the true v_2 reaction plane is observed to be zero and the data can be described by the model up to $p_T < 4$ GeV/c only by the estimated reaction plane method. Zero v_5 is caused by the randomly oriented true v_3 reaction plane and the fact that v_5 is proportional to the product of v_2 and v_3, $v_5 \propto v_2 v_3$. In all graphs, significant fluctuation in high $p_T \gtrsim 8$ GeV/c occurs because of the lack of the statistics.

The D^0, D^+ and J/ψ mesons transverse momentum distributions generated by the HYDJET++ match the experimental data very well in wide range of centralities. Shape of the simulated D^0 and $D^\pm$ elliptic flow v_2 suggests nontrivial dependence of v_2 on p_T with a significant increase at $p_T \sim 4$ GeV/c and roughly matches the magnitude of the experimental data. However, the experimental points include large uncertainties and no clear conclusion about the model precision can be made. Also slight overestimation of the J/ψ distribution in 20-40% centrality region has been observed.

The shown results perfectly agree with the results published in the previous study [135]. It has been confirmed that in Pb+Pb collisions at $\sqrt{s_{NN}} = 2.76$ TeV the thermal freeze-out temperature T_{th} is the same for the charged hadrons $h^\pm$ and the D mesons and different for the J/ψ quarkonia. The fact that D mesons do not thermalize at the same temperature as they do in case of the Au+Au collisions at $\sqrt{s_{NN}} = 200$ GeV is attributed to the D meson interaction cross section which is very close to the interaction cross section of the light hadrons while the J/ψ interaction cross section remains much smaller [135].

4.3   Pb+Pb at $\sqrt{s_{NN}} = 5.02$ TeV

In this section, completely new simulation results of the charged and charm particle distributions in Pb+Pb collisions at $\sqrt{s_{NN}} = 5.02$ TeV are presented. Based on the results from Pb+Pb collisions at $\sqrt{s_{NN}} = 2.76$ TeV, it is expected that there is also one set of HYDJET++ parameters for the charged hadron $h^\pm$ distributions and the D mesons and another set of parameters for description of the J/ψ quarkonia behavior in Pb+Pb collisions at $\sqrt{s_{NN}} = 5.02$ TeV. For simulation of charged hadrons and D mesons, extrapolated parameters for Pb+Pb collisions at $\sqrt{s_{NN}} = 5.02$ TeV energy delivered with the HYDJET++ production have been used. Parameters used for the J/ψ simulation have been chosen in accordance with $\sqrt{s_{NN}} = 2.76$ TeV energy and $p_{T,min} = 5$ GeV/c is overtaken from the previous study of B mesons [122]. Charm enhancement factor γ_c has been firstly tuned to the J/ψ meson distribution and then used for simulation of the D mesons. Summary of the used parameters is shown in Tab. 4.2.

4.3.1 $h^\pm$ and D Meson Distributions

The HYDJET++ simulated yield p_T and η distributions and collective flow coefficients v_2, v_3, v_4, v_5 p_T distributions of the charged particles $h^\pm$, yield p_T dependence

of D^0 and D^+ as well as their R_{AA} and D^0 elliptic flow p_T distributions in wide centrality range have been studied. Parameters for $h^\pm$ and D mesons from the Tab. 4.2 have been used for the simulations. Parameter γ_c has been tuned to the J/ψ distributions first.
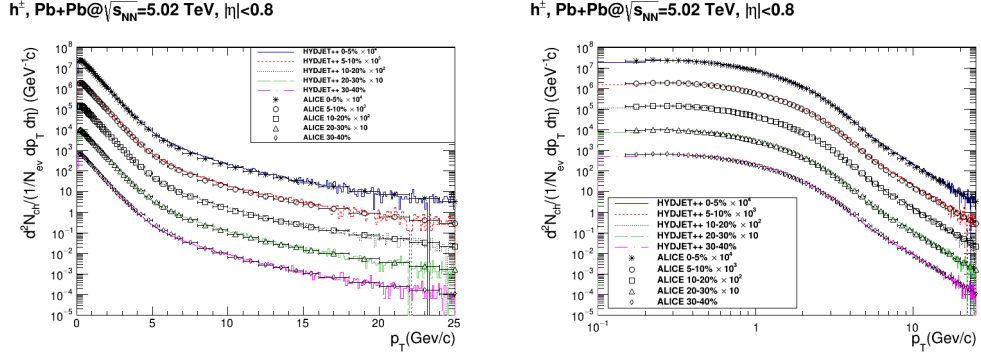
Figure 4.18: THIS WORK: Comparison of the HYDJET++ p_T distribution histograms of yield of all charged hadrons $h^\pm$ for Pb+Pb collisions at $\sqrt{s_{NN}} = 5.02$ TeV with the ALICE experimental data [143] in 0-5%, 5-10%, 10-20%, 20-30%, 30-40% centrality bins. In the right graph, logarithmic scale of the x axis has been used. Cut $|\eta| < 0.8$ has also been applied.

The HYDJET++ simulated p_T distributions of charged hadrons $h^\pm$ yield for 0-5%, 5-10%, 10-20%, 20-30%, 30-40% centralities under pseudorapidity condition $|\eta| < 0.8$ compared to the ALICE data [143] can be seen in Fig. 4.18. Pseudorapidity η dependence of the charged particles can be seen in Fig. C.1 in appendix C.

Collective flow coefficients of the charged hadrons have been studied by the HYDJET++ true event plane method and by the scalar product method (SP) from the experimental analysis. In the scalar product method, positive and negative η regions are differentiated and two flow vectors $\vec{Q}_n^{\mathrm{P}}$ and $\vec{Q}_n^{\mathrm{N}}$ for $\eta > 0$ and $\eta < 0$ tracks are respectively introduced. The $\vec{Q}_n$ vector is defined by the same formula as in the experimental event plane method in Eq. (4.1) while the sum runs over either $\eta > 0$ or $\eta < 0$ tracks. Scalar product collective flow is computed by matching particle vector $\vec{q}_n = (\cos n\phi, \sin n\phi)$ with $\eta > 0$ to the flow vector $\vec{Q}^{\mathrm{N}}$ and event plane angle Ψ_n^{N} with $\eta < 0$ and vice versa according to the formula [144]

$$v_n\{\mathrm{SP}\} = \frac{\langle |\vec{q}_n||\vec{Q}_n^{\mathrm{N|P}}| \cos n(\phi - \Psi_n^{\mathrm{N|P}}) \rangle}{\sqrt{\langle |\vec{Q}_n^{\mathrm{N}}||\vec{Q}_n^{\mathrm{P}}| \cos n(\Psi_n^{\mathrm{P}} - \Psi_n^{\mathrm{N}}) \rangle}}, \qquad (4.4)$$

where the $\langle \ldots \rangle$ brackets denote average over all the events. Results obtained by the true HYDJET++ event plane method for the elliptic and triangular flow in two centrality bins 0-5% and 20-30% can be seen in Fig. 4.19 and 4.20. In all graphs soft and hard HYDJET++ component have been separated. In Fig. C.2 and C.3 in appendix C, scalar product collective flow distributions $v_2\{\mathrm{SP}\}$, $v_3\{\mathrm{SP}\}$, $v_4\{\mathrm{SP}\}$, $v_5\{\mathrm{SP}\}$ have been compared to the ATLAS experimental data [144] in four centrality bins 10-20%, 20-30%, 30-40% and 40-50%. Histograms are scaled by the number of

events in the particular HYDJET++ component and therefore the showed "HARD" and "SOFT" parts do not sum to the final flow[6].
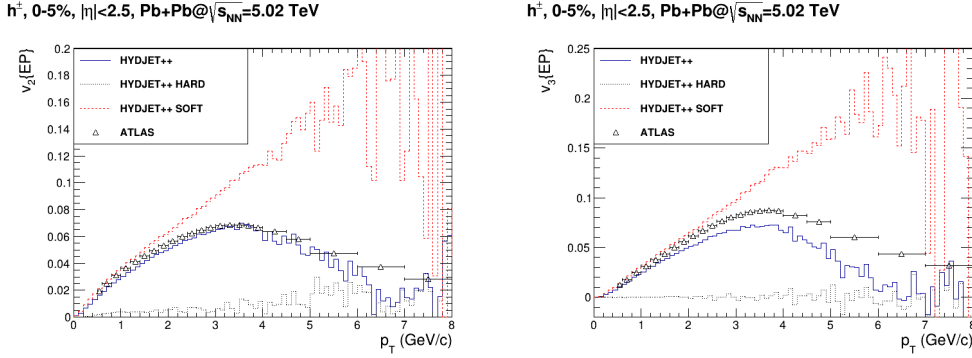
Figure 4.19: THIS WORK: Comparison of the HYDJET++ true reaction plane elliptic v_2 (left) and triangular v_3 (left) flow p_T distribution histograms of all the charged hadrons $h^\pm$ for Pb+Pb collisions at $\sqrt{s_{NN}} = 5.02$ TeV with the ATLAS experimental data [144] in 0-5% centrality bin. Pseudorapidity cut $|\eta| < 2.5$ has been applied and soft and hard component of the HYDJET++ have been extracted.
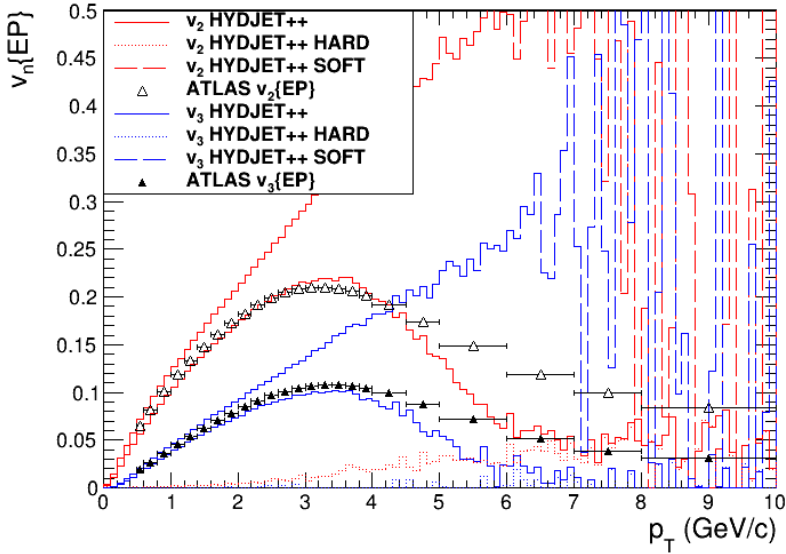
Figure 4.20: THIS WORK: Comparison of the HYDJET++ true reaction plane elliptic v_2 and triangular v_3 flow p_T distribution histograms of all the charged hadrons $h^\pm$ for Pb+Pb collisions at $\sqrt{s_{NN}} = 5.02$ TeV with the ATLAS experimental data [144] in 20-30% centrality bin. Pseudorapidity cut $|\eta| < 2.5$ has been applied and soft and hard component of the HYDJET++ have been extracted.

The HYDJET++ simulated D^0 and D^+ meson yield histograms for two centrality bins $0-10\%$ and $30-50\%$ compared to the ALICE experimental data [145] are shown

---

[6] $\frac{\sum^N a^i}{N} + \frac{\sum^M b^i}{M} \neq \frac{\sum^N a^i + \sum^M b^i}{N+M}$

in Fig. 4.21 and 4.22. The soft and hard HYDJET++ parts have been separated and $|y| < 0.5$ rapidity cut has been applied. For all the four distributions the nuclear modification factor R_{AA} has also been computed and can be seen in Fig. C.4 and C.5. The nuclear overlap function values $\langle T_{AA} \rangle = 23.07 \pm 0.44$ (mb)$^{-1}$ for 0-10% centrality interval and $\langle T_{AA} \rangle = 3.90 \pm 0.11$ (mb)$^{-1}$ for 30-50% centrality interval [145] have been used. FONLL framework[7] reference D meson cross sections from p+p collisions σ^{pp} have been used [146, 147, 148, 149]. Uncertainty band has been computed from $\langle T_{AA} \rangle$ and σ^{pp} uncertainties where uncertainties from scales, masses and PDFs have been considered.

The D^0 elliptic and triangular flow p_T distributions for 0-10%, 10-30% and 30-50% centrality bins compared to the CMS data [150] can be seen in Fig. C.6 in appendix C. Rapidity cut $|y| < 1$ and the HYDJET++ true reaction plane have been used.
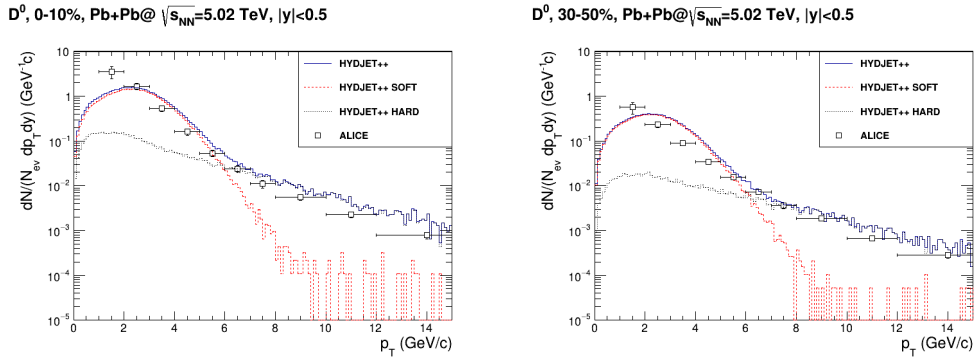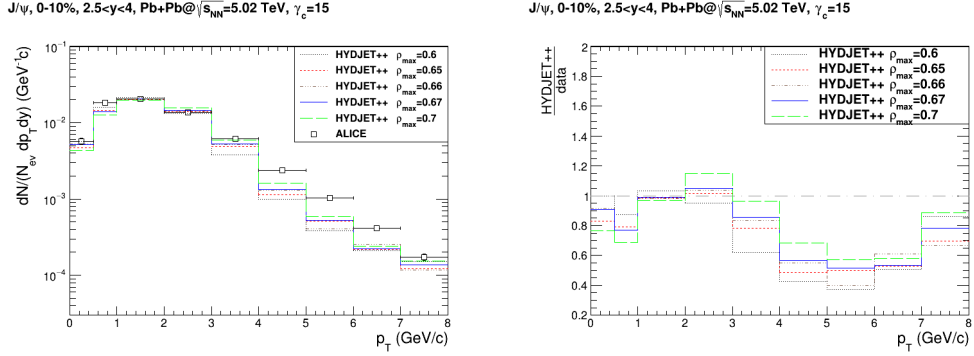

Figure 4.21: THIS WORK: Comparison of the HYDJET++ simulated p_T distribution histograms of the D^0 meson yield to the ALICE experimental data [145] in Pb+Pb collisions at $\sqrt{s_{\mathrm{NN}}} = 5.02$ TeV in 0-10% (left) and 30-50% (right) centrality regions. Rapidity cuts $|y| < 0.5$ has been applied and the soft and hard HYDJET++ components have been extracted.

4.3.2 J/ψ Distributions

The J/ψ meson distributions in Pb+Pb collisions at $\sqrt{s_{\mathrm{NN}}} = 5.02$ TeV energy have been studied here for the first time and parameters suitable for the satisfying description of the experimental data had to be found first. Because the collision energy increased only by a factor of two, parameters for the J/ψ description at $\sqrt{s_{\mathrm{NN}}} = 2.76$ TeV were used as the starting point. Tuning has been performed on the most central collisions. It has been found that the J/ψ yield p_T simulated distributions fit the distribution maximum in 0-10% centrality region well when $\gamma_c = 15$ is used, as is shown in Fig. 4.23. The possibility to compensate the clear underestimation of the data in $p_T \sim 5$ GeV/c region caused by junction between the

---

[7]The FONLL framework matches fixed next-to-leading order (NLO) QCD with all-order resummation to next-to-leading log (NLL) accuracy in the limit where the transverse momentum of a heavy quark is much larger than its mass. FONLL calculation can predict bottom and charm production data [146].
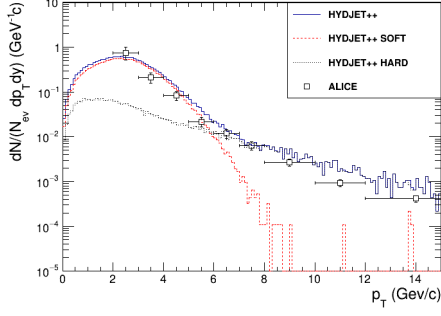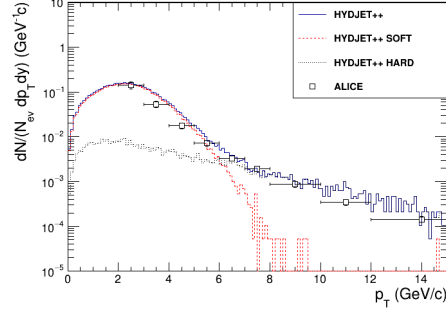
Figure 4.22: THIS WORK: Comparison of the HYDJET++ simulated p_T distribution histograms of D^0 meson yield to the ALICE experimental data [145] in Pb+Pb collisions at $\sqrt{s_{\mathrm{NN}}} = 5.02$ TeV in 0-10% (left) and 30-50% (right) centrality regions. Rapidity cuts $|y| < 0.5$ has been applied and the soft and hard HYDJET++ components have been extracted.

soft and hard parts by changing the maximal transverse flow rapidity ρ_{max} parameter has been thoroughly investigated.
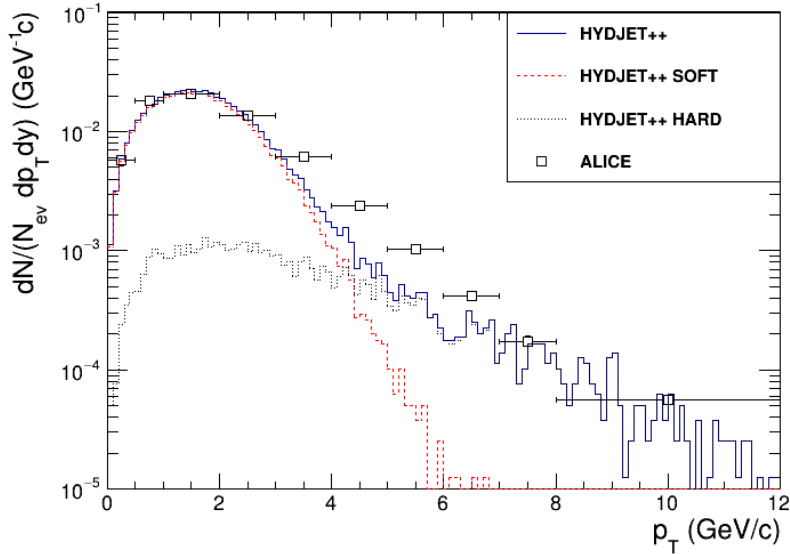
Figure 4.23: THIS WORK: Comparison of the HYDJET++ simulated p_T distribution histograms of the J/ψ meson yield to the ALICE experimental data [151] in Pb+Pb collisions at $\sqrt{s_{\mathrm{NN}}} = 5.02$ TeV in 0-10% centrality region. Forward rapidity cut $2.5 < y < 4$ has been applied and the soft and hard HYDJET++ component have been extracted.

In the left Fig. 4.24, yield distribution of the J/ψ is presented for different $\rho_{max} = 0.6, 0.65, 0.66, 0.67, 0.7$ values with binning matching the experimental data. Because of the long simulation time, only limited number of events has been generated for this comparison (see Tab. C.1) and statistical fluctuations may play an important role in

$p_T > 5$ GeV/c. It can be seen that increase of the ρ_{max} leads to a better description of the experimental data in $p_T \sim 5$ GeV/c region and a worse description in $p_{<1}$ GeV/c. In order to evaluate the precision, difference of the HYDJET++ simulation and the experimental data $\frac{\text{HYDJET++}}{\text{data}}$, has been evaluated and can be seen in right Fig. 4.24.

Figure 4.24: THIS WORK: Comparison of the HYDJET++ simulated p_T distribution histograms of the J/ψ meson yield to the ALICE experimental data [151] in Pb+Pb collisions at $\sqrt{s_{NN}} = 5.02$ TeV in the 0-10% centrality region. Histograms for different ρ_{max} values are shown. In the right graph relative difference between the model and the data is studied.

Commonly used method to express a model precision is the Pearson's $\chi^2 = \sum_0^{p_T} \frac{(\text{HYDJET++}-\text{data})^2}{\text{HYDJET++}}$ statistic for Poisson distributions [81] and it is plotted in Fig. 4.25. The distribution shows that in $p_T < 3$ GeV/c region the most suitable ρ_{max} parameter is $\rho_{max} = 0.6$ and for the $p_T > 3$ region it is $\rho_{max} = 0.67$.

The same distributions have been studied in 10-20% centrality bin and the results can be seen in Fig. C.7 and C.8 in appendix C. In the J/ψ yield p_T distribution, the HYDJET++ overestimates the data peak at $p_T = 1.5$ GeV/c. The χ^2 distribution does not show one single dominant ρ_{max} value for all the p_T bins. In the studied $0 < p_T < 8$ GeV/c interval, $rho_{max} = 0.67$ performs the best.

Based on the 0-10% bin, two candidates $\rho_{max} = 0.6$ and $\rho_{max} = 0.67$ have been studied further in the elliptic and triangular flow distributions of J/ψ in 0-10% and 10-30% centrality regions. For this purpose, eight times more events have been simulated with the $\rho_{max} = 0.67$ option.

Elliptic and triangular flow of the J/ψ quarkonium in 0-10% and 10-30% centrality ranges can be seen in Fig. 4.26 and 4.27. Two dependencies for $\rho_{max} = 0.6$ and 0.67 are shown. It is observed that both distributions are almost identical and describe the data rather well up to $p_T < 6$ GeV/c.

Finally, J/ψ yield studied in three centrality bins 0-10%, 10-20% and 20-30% and R_{AA} distributions generated with $\rho_{max} = 0.6$ can be seen in Fig. 4.23, 4.28 and 4.29. The same distributions for the $\rho_{max} = 0.67$ option are shown in Fig. 4.30 and 4.31. In the J/ψ R_{AA} computation, the nuclear overlap function $\langle T_{AA} \rangle = 18.83 \pm 5.29$ (mb)$^{-1}$ for 0-20% centrality interval has been used [153]. Reference of the p+p
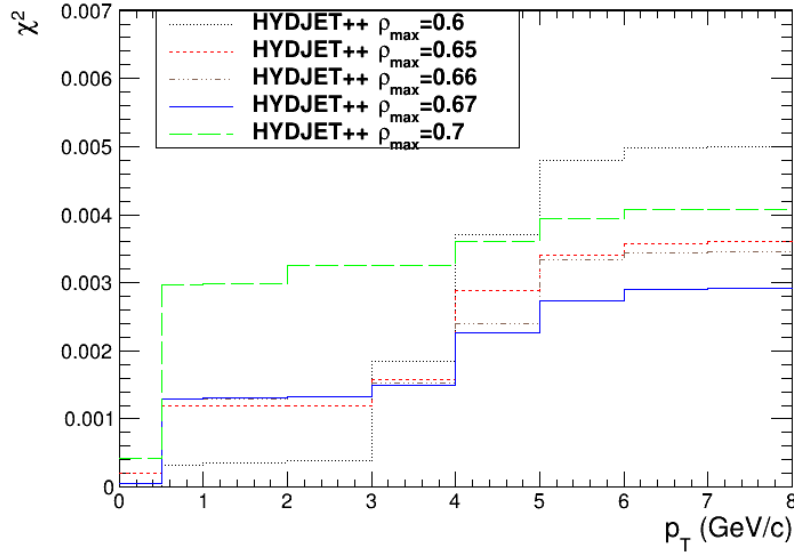
Figure 4.25: THIS WORK: Precision evaluation of the HYDJET++ simulation with five different ρ_{max} values in Pb+Pb collisions at $\sqrt{s_{NN}} = 5.02$ TeV in the 0-10% centrality region using χ^2 distribution.
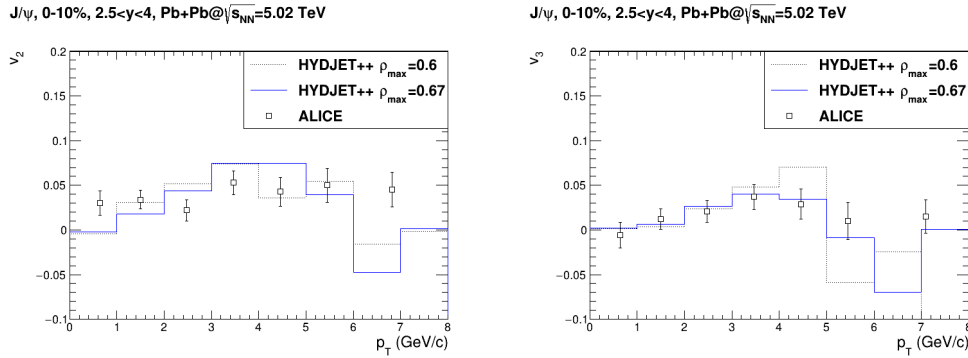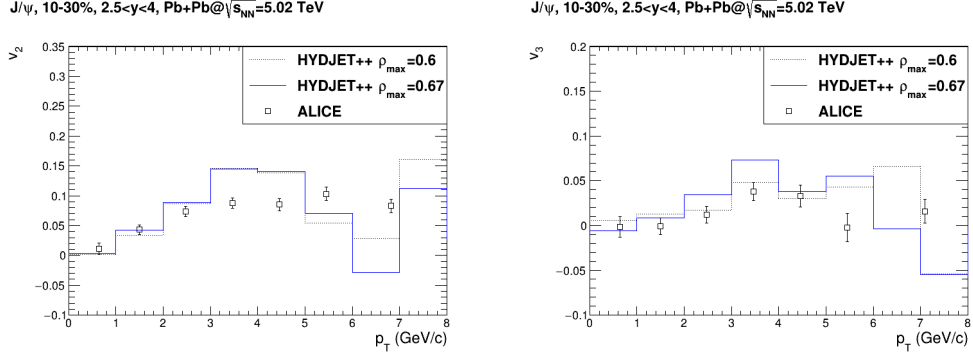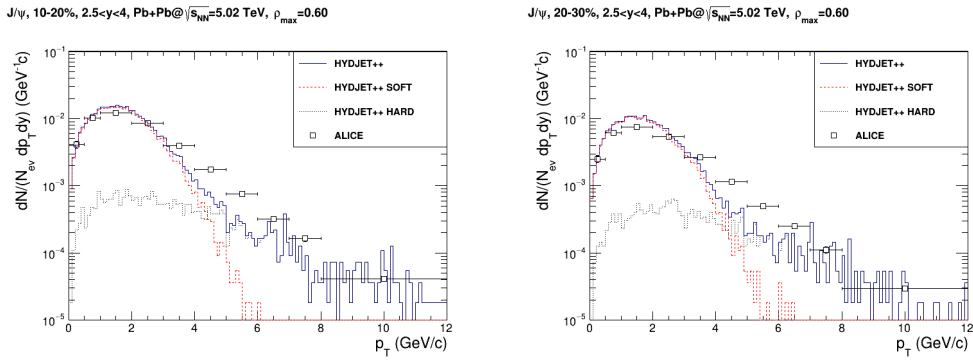

Figure 4.26: THIS WORK: Comparison of the HYDJET++ simulated p_T distribution histograms of the J/ψ meson elliptic (left) and triangular (right) flow to the ALICE experimental data [152] in Pb+Pb collisions at $\sqrt{s_{NN}} = 5.02$ TeV in the 0-10% centrality region. Histograms for different ρ_{max} values are shown.

collisions has been taken from Ref. [154]. Uncertainty band has been computed from uncertainties of the $\langle T_{AA} \rangle$ and p+p collisions.

4.3.3 Discussion of Pb+Pb at $\sqrt{s_{NN}} = 5.02$ TeV Results

In the charged particle yield p_T and η distributions, remarkable agreement between the HYDJET++ model and experimental data has been observed over wide range of transverse momentum and pseudorapidity units. Elliptic and triangular flow event plane distributions can be described well by the HYDJET++ model up to $p_T < 5$

Figure 4.27: THIS WORK: Comparison of the HYDJET++ simulated p_T distribution histograms of the J/ψ meson elliptic (left) and triangular (right) flow to the ALICE experimental data [152] in Pb+Pb collisions at $\sqrt{s_{NN}} = 5.02$ TeV in the 10-30% centrality region. Histograms for different ρ_{max} values are shown.

Figure 4.28: THIS WORK: Comparison of the HYDJET++ simulated p_T distribution histograms of J/ψ meson yield to the ALICE experimental data [151] in Pb+Pb collisions at $\sqrt{s_{NN}} = 5.02$ TeV in 10-20% (left) and 20-30% (right) centrality region. Forward rapidity cut $2.5 < y < 4$ has been applied and soft blast wave and hard jet component have been extracted from HYDJET++.
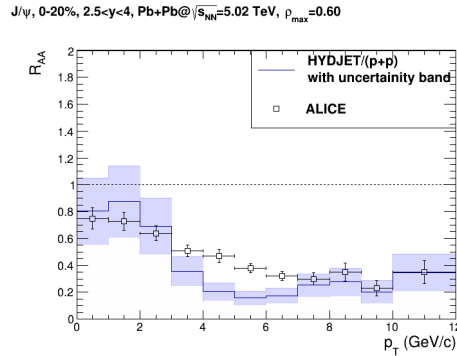
Figure 4.29: THIS WORK: Comparison of the HYDJET++ simulated J/ψ nuclear modification factor R_{AA} to the ALICE experimental data [151] in Pb+Pb collisions at $\sqrt{s_{NN}} = 5.02$ TeV in 0-20% centrality collisions. Forward rapidity cut $2.5 < y < 4$ has been applied.
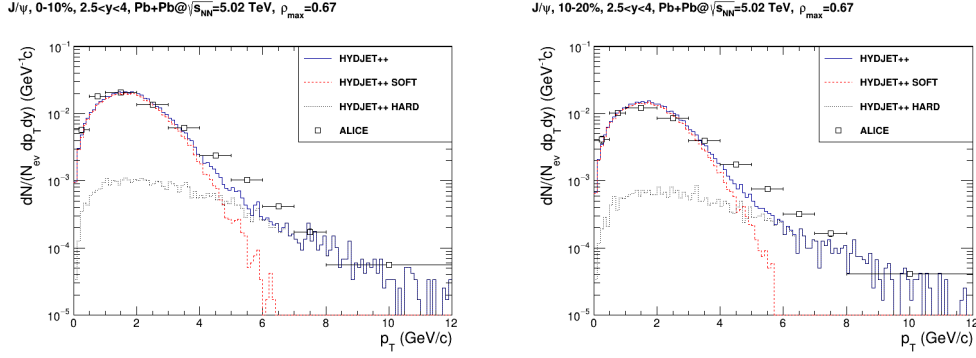
Figure 4.30: THIS WORK: Comparison of the HYDJET++ simulated p_T distribution histograms of J/ψ meson yield with $\rho_{max} = 0.67$ option to the ALICE experimental data [151] in Pb+Pb collisions at $\sqrt{s_{NN}} = 5.02$ TeV in 0-10% (left) and 10-20% (right) centrality region. Forward rapidity cut $2.5 < y < 4$ has been applied and soft and hard HYDJET++ components have been extracted.
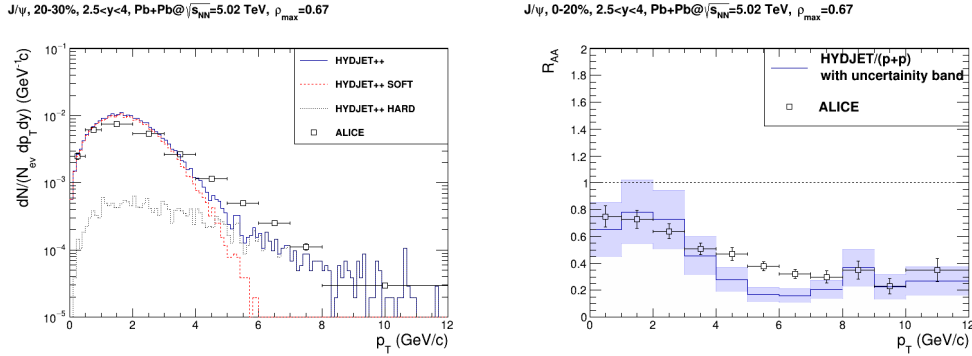
Figure 4.31: THIS WORK: Comparison of the HYDJET++ simulated p_T distribution histograms of J/ψ meson yield in 20-30% centrality (left) and nuclear modification factor R_{AA} in 0-20% centrality to the ALICE experimental data [151] in Pb+Pb collisions at $\sqrt{s_{NN}} = 5.02$ TeV. Option with $\rho_{max} = 0.67$ and forward rapidity cut $2.5 < y < 4$ has been applied and also soft and hard HYDJET++ components have been extracted.

GeV/c in 0-5% and 20-30% centrality intervals. Underestimation of the data in larger p_T might result from HYDJET++ jet component which dominates in region $p_T > 5$ GeV/c.

Elliptic and triangular flow scalar product distributions show the very same behavior. Moreover, the model overestimates the data in $p_T = 3 - 4$ GeV/c region in the more peripheral collisions. Similar effect has been observed at the $\sqrt{s_{NN}} = 2.76$ TeV energy and can be attributed to the lower precision of the HYDJET++ model in peripheral collisions. Also in the quadrangular and pentagonal flow, similarity to the lower collision energy can be observed. With the rising centrality v_4 fits the data better while v_5 is satisfyingly accurate in all the studied centrality regions. However, in both distributions large fluctuations occur in high $p_T > 6$ region due to the lack of statistics.

The D^0 and D^+ yield p_T distributions can be described well by the chosen HYD-JET++ set of parameters with $\gamma_c = 15$ in both central and peripheral collisions in $2 < p_T < 14$ GeV/c region. The only deviation from the experimental data is observed in the D^0 in 30-50% centrality range in $2 < p_T < 6$ GeV where the HYDJET++ overestimates the data. Next, it can be seen that the D^0 nuclear modification factor R_{AA} computed by the HYDJET++ agrees with the experimental data in wide $6 < p_T < 20$ GeV/c range in both central and peripheral collisions where the jet HYDJET++ part dominates. The data mismatch of the simulation in the $p_T < 6$ GeV is clearly visible in the R_{AA}. The HYDJET++ R_{AA} of the D^+ underestimates the data roughly by a factor of two in central collisions and by a factor of 2.5 in peripheral collisions. Nonetheless, qualitative p_T dependence agrees with that of the data in $4 < p_T < 20$ GeV/c range. Moreover, from the observed slight overestimation of the D^+ yield distributions one would expect overestimation also in R_{AA}. This may be explained by a difference in the used p+p reference data which might be different from that used for the experimental data.

In case of the elliptic and triangular flow of the D^0 mesons, the HYDJET++ fits the data much worse than at the $\sqrt{s_{\mathrm{NN}}} = 2.76$ TeV energy. While in the 0-10% centrality bin the magnitude of the simulated distributions matches the magnitude of the data within the data uncertainties, in the more peripheral collisions a clear mismatch between the data and the simulation can be seen. The HYDJET++ simulation reproduces the rise of v_2 and v_3 with the peak around $p_T \sim 5$ GeV/c but the data hint the peak around $p_t \sim 3$ GeV/c. It can be stated that HYDJET++ can not reproduce the elliptic and triangular flow of the D^0 mesons in peripheral collisions in intermediate $4 < p_T < 6$ GeV/c range with the chosen set of parameters and a finer tuning is be needed.

The J/ψ distributions have been studied here for the first time. It has been found that the charm scaling factor $\gamma_c = 15$ has to be set to accurately describe the magnitude of the peak in J/ψ yield p_T distribution in 0-10% centrality region. From 10-20% and 20-30% centrality studies can be seen that $\gamma_c = 15$ overestimates the spectra at $p_T \sim 2$ GeV/c and γ_c has to be adjusted for every centrality region to match the data. Similar effect has been observed at $\sqrt{s_{\mathrm{NN}}} = 2.76$ TeV energy.

In the J/ψ yield p_T dependencies, a clear underestimation of the experimental data in the $4 < p_T < 7$ GeV/c region is observed. This is caused by junction of the soft and hard part of the simulated HYDJET++ distribution. Possibility to compensate this effect by rising the maximal transverse flow rapidity at the thermal freeze-out ρ_{max} parameter has been studied. It appears that using $\rho_{max} = 0.67$ slightly neutralizes the mismatch in the $4 < p_T < 7$ GeV/c area while it pronounces the mismatch in $p_T < 1$ GeV/c region. Using $\rho_{max} = 0.6$ offers better description of the data in $p_T < 3$ GeV/c region while $\rho_{max} = 0.67$ in the $3 < p_T < 8$ GeV/c region. However, this result is based on a limited number of simulated events because of the computational time demandingness and statistical fluctuations may not be negligible in the $p_T > 5$ GeV/c region.

From the J/ψ yield distributions the nuclear modification factor R_{AA} has also been computed in 0-20% centrality region for both $\rho_{max} = 0.6$ and 0.67 options. Behavior observed in the yield distributions is preserved and no significant difference between

the two ρ_{max} options is observed. Underestimation of the data is seen in the interme-
diate $4 < p_T < 7$ GeV/c region and in both low $p_T < 3$ GeV/c and high $8 < p_T < 12$
GeV/c regions the experimental data are described within the uncertainties by the
model.

The elliptic and triangular flow of J/ψ in 0-10% and 10-30% centrality region can
be described very well by the HYDJET++ model up to $p_T < 6$ GeV/c and no
significant impact of the ρ_{max} parameter on the distributions has been observed.

From the presented results it can be concluded that the charged particles $h^{\pm}$ and
D^0 mesons follow the same freeze-out pattern in Pb+Pb collisions at $\sqrt{s_{\mathrm{NN}}} = 5.02$
TeV as in Pb+Pb collisions at $\sqrt{s_{\mathrm{NN}}} = 2.76$ TeV. Correct description of the D and
J/ψ mesons p_T distributions has been achieved by tuning the γ_c parameter. The
J/ψ elliptic and triangular distributions can be desribed well by the HYDJET++
regardless the maximal transverse flow rapidity at the thermal freeze-out $\rho_{max} =$
0.6 or 0.67 parameter. However, the elliptic and triangular flow of the D^0 meson
could not be described in peripheral collisions in the intermediate p_T range by the
HYDJET++ with the chosen set of parameters.

Conclusion

At sufficiently high temperature, lattice QCD calculations predict creation of deconfined phase of the nuclear matter, quark-gluon plasma, where quarks and gluons can move freely within the medium. Such conditions may arise in ultra-relativistic nuclear collisions. Signatures of the QGP can be observed for instance in modification of a particle yield or in the collective flow effects. By comparison of the experimental data with the simulations of various physical models the true medium mechanism can be unveiled. One of the models is HYDJET++ which merges hydro-inspired blast wave model used for low transverse momentum particles with jet origin applied in high transverse momentum region.

In this thesis, a detailed study of the HYDJET++ 2.4 performance has been conducted in Au+Au collisions at $\sqrt{s_{NN}} = 200$ GeV and in Pb+Pb collisions at $\sqrt{s_{NN}} = 2.76$ and 5.02 TeV. Charged hadrons $h^{\pm}$ (comprising pions $\pi^{\pm}$, kaons $K^{\pm}$, protons and antiprotons), D mesons and J/ψ quarkonia yield and collective flow p_T distributions have been studied with focus on the particle thermalization. Results of the Pb+Pb collisions at $\sqrt{s_{NN}} = 5.02$ TeV are computed here for the first time.

It has been found that in Au+Au collisions at $\sqrt{s_{NN}} = 200$ GeV the thermal freeze-out temperature of the D mesons $T_{th} = 0.165$ GeV is the same as that for J/ψ mesons while charged particles thermalize at $T_{th} = 0.1$ GeV. Inability of the HYDJET++ 2.4 version to correctly describe the elliptic flow of the charged particles with the simulation parameters tuned to the 2.1 version has been observed. Even though there is a fair agreement between the HYDJET++ 2.4 and the experimental data in all other distributions when $\gamma_c = 6$ charm enhancement factor is used, new tuning of the parameters is needed for the 2.4 version. This tuning has not been conducted in this thesis and authors of the model have been informed.

In Pb+Pb collisions at $\sqrt{s_{NN}} = 2.76$ TeV energy, the D mesons thermalize at different freeze-out temperature $T_{th} = 0.105$ GeV than in Au+Au collisions at $\sqrt{s_{NN}} = 200$ GeV. Their thermalization occurs at the same temperature as for the charged hadrons which suggests that their interaction cross sections are very close to each other at the $\sqrt{s_{NN}} = 2.76$ TeV energy. With set of the used parameters, the HYDJET++ can describe well all the studied $h^{\pm}, D, J/\psi$ yield p_T distributions and v_2, v_3, v_4, v_5 of charged hadrons in wide 5-50% centrality range. The HYDJET++ D meson elliptic flow agrees with the experimental data due to large uncertainties.

The charged particle and charm meson HYDJET++ distributions in Pb+Pb collisions at $\sqrt{s_{NN}} = 5.02$ TeV have been studied for the first time in this thesis. It has been found that using the set of extrapolated parameters from the $\sqrt{s_{NN}} = 2.76$ TeV

energy reproduces the charged hadron spectra remarkably well over large 10-50% centrality range except of the quadrangular flow p_T distribution. Charm enhancement factor $\gamma_c = 15$ has been tuned on the J/ψ yield distribution and used also for the D meson distributions. Agreement between the experimental data and the HYDJET++ model is seen in the D meson yield graphs, however, elliptic and triangular flow of the D mesons could not be reproduced by the extrapolated parameters in peripheral collisions. Except of the $p_{T,min}$ threshold, all the parameters have been preserved from $\sqrt{s_{\mathrm{NN}}} = 2.76$ TeV energy for the J/ψ distributions and satisfactory description of all the data has been achieved in the most central collisions in the low $p_T < 3$ GeV/c. In the less central collisions, mismatch between the HYDJET++ and the experimental data has been observed in J/ψ yield distributions where tuning the γ_c parameter to every single centrality bin is needed to match the data. No significant improvement has been observed for the maximal transverse flow rapidity at thermal freeze-out $\rho_{max} = 0.67$ parameter value.

To conclude, the HYDJET++ model simulations agree well with the experimental data in wide energy range and the charm production in the most central Pb+Pb collisions at $\sqrt{s_{\mathrm{NN}}} = 5.02$ TeV is found to behave according to the same mechanisms as at the $\sqrt{s_{\mathrm{NN}}} = 2.76$ TeV energy.

Bibliography

[1] D. Galbraith and C. Burgard. Standard model diagram, Last visit April 14, 2021. URL: `http://davidgalbraith.org/portfolio/ux-standard-model-of-the-standard-model/`.

[2] E. V. Shuryak. Quantum chromodynamics and the theory of superdense matter. *Phys. Rep.*, 61(2):71, 1980. `doi:https://doi.org/10.1016/0370-1573(80)90105-2`.

[3] S. Weinberg. *The first three minutes : a modern view of the origin of the universe.* Basic Books, New York, 1993.

[4] D. Perkins. *Introduction to High Energy Physics.* Cambridge: Cambridge University Press, 4 edition, 2000. `doi:doi:10.1017/CBO9780511809040`.

[5] R. Hagedorn. *On the Hadronic Mass Spectrum*, pages 223–228. Springer International Publishing, Cham, 2016. `doi:10.1007/978-3-319-17545-4_20`.

[6] P. Steinbrecher. The QCD crossover at zero and non-zero baryon densities from Lattice QCD. *Nucl. Phys. A*, 982:847, Feb 2019. `doi:10.1016/j.nuclphysa.2018.08.025`.

[7] G. Cook and R. H. Dickerson. Understanding the chemical potential. *Am. J. Phys.*, 63(8):737, August 1995. `doi:10.1119/1.17844`.

[8] K. Rajagopal. Mapping the QCD phase diagram. *Nucl. Phys. A*, 661(1-4):150, Dec 1999. `doi:10.1016/s0375-9474(99)85017-9`.

[9] H.-T. Ding. New developments in lattice QCD on equilibrium physics and phase diagram. *Nucl. Phys. A*, 1005:121940, 2021. `doi:https://doi.org/10.1016/j.nuclphysa.2020.121940`.

[10] U. Heinz et al. Exploring the properties of the phases of QCD matter - research opportunities and priorities for the next decade, 2015. `arXiv:1501.06477`.

[11] CERN. The Large Hadron Collider. URL: `https://home.cern/science/accelerators/large-hadron-collider`.

[12] Brookhaven National Laboratory. The Relativistic Heavy Ion Collider. URL: `https://www.bnl.gov/rhic/`.

[13] GSI Helmholtz Centre for Heavy Ion Research. Facility for Antiproton and Ion Research in Europe. URL: `https://fair-center.eu/`.

[14] T. Ablyazimov et al. Challenges in QCD matter physics – The scientific programme of the Compressed Baryonic Matter experiment at FAIR. *Eur. Phys. J. A*, 53(3):60, Mar 2017. `doi:10.1140/epja/i2017-12248-y`.

[15] K. Johnson. The M.I.T. Bag Model. *Acta Phys. Polon. B*, 6:865, 1975.

[16] C.-Y. Wong. *Introduction to High-Energy Heavy-Ion Collisions*. WORLD SCIENTIFIC, Sep 1994. `doi:10.1142/1128`.

[17] K. Krane. *Introductory Nucl. Phys.* Wiley, New York, 1988.

[18] F. Gelis et al. The Color Glass Condensate. *Annual Review of Nuclear and Particle Science*, 60(1):463, Nov 2010. `doi:10.1146/annurev.nucl.010909.083629`.

[19] P. Braun-Munzinger et al. *Particle Production in Heavy Ion Collisions*, pages 491–599. World Scientific Publishing Co. Pte. Ltd, 2004. `doi:10.1142/9789812795533_0008`.

[20] J. Adams et al. Experimental and theoretical challenges in the search for the quark–gluon plasma: The STAR Collaboration's critical assessment of the evidence from RHIC collisions. *Nucl. Phys. A*, 757(1-2):102, Aug 2005. `doi:10.1016/j.nuclphysa.2005.03.085`.

[21] P. Huovinen. Chemical freeze-out temperature in the hydrodynamical description of Au+Au collisions at $\sqrt{s_{\mathrm{NN}}} = 200$ GeV. *Eur. Phys. J. A*, 37(1):121, Jul 2008. `doi:10.1140/epja/i2007-10611-3`.

[22] H.-L. Lao et al. Kinetic freeze-out temperatures in central and peripheral collisions: which one is larger? *Nucl. Sci. Tech.*, 29(6):82, Apr 2018. `doi:10.1007/s41365-018-0425-x`.

[23] Deckard. Evolution of collisions and QGP. [online], Last visit January 25, 2021. URL: `https://particlesandfriends.wordpress.com/2016/10/14/evolution-of-collisions-and-qgp/`.

[24] L. D. Landau and E. M. Lifschits. *The Classical Theory of Fields*, volume 2 of *Course of Theoretical Physics*. Pergamon Press, Oxford, 1975.

[25] L. P. Csernai. *Introduction to relativistic heavy ion collisions*. Wiley, Chichester New York, 1994.

[26] T. Hirano et al. Hydrodynamics and Flow. *Lecture Notes in Physics*, page 139–178, 2009. `doi:10.1007/978-3-642-02286-9_4`.

[27] S. Weinberg. *Gravitation and Cosmology: Principles and Applications of the General Theory of Relativity*. Wiley, New York, 1972.

[28] R. Vogt. *Ultrarelativistic heavy-ion collisions*. Elsevier, Oxford, 2007.

[29] T. Hirano. Hydrodynamic approaches to relativistic heavy ion collisions. *Acta Phys. Polon. B*, 36:187, 2005.

[30] F. Cooper et al. Landau's hydrodynamic model of particle production and electron-positron annihilation into hadrons. *Phys. Rev. D*, 11:192, Jan 1975. `doi:10.1103/PhysRevD.11.192`.

[31] A. Jaiswal and V. Roy. Relativistic hydrodynamics in heavy-ion collisions: general aspects and recent developments. *Adv. High Energy Phys.*, 2016:9623034, 2016. `doi:10.1155/2016/9623034`.

[32] C. Ding et al. Hydrodynamic description of D meson production in high-energy heavy-ion collisions. Jan 2021. `arXiv:2101.02356`.

[33] R. J. Glauber. *Lectures in Theoretical Physics*. New York: Interscience, 1959.

[34] M. L. Miller et al. Glauber Modeling in High-Energy Nuclear Collisions. *Annu. Rev. Nucl. Part. Sci.*, 57(1):205, Nov 2007. `doi:10.1146/annurev.nucl.57.090506.123020`.

[35] A. Toia. Participants and spectators at the heavy-ion fireball, Last visited April 15, 2021. URL: `https://cerncourier.com/a/participants-and-spectators-at-the-heavy-ion-fireball/`.

[36] S. Sarkar et al., editor. *The physics of the quark-gluon plasma*, volume 785. 2010. `doi:10.1007/978-3-642-02286-9`.

[37] J. Rafelski et al. Strangeness Production in the Quark-Gluon Plasma. *Phys. Rev. Lett.*, 48:1066, Apr 1982. `doi:10.1103/PhysRevLett.48.1066`.

[38] P. Koch et al. From strangeness enhancement to quark–gluon plasma discovery. *Int. J. Mod. Phys. A*, 32(31):1730024, 2017. `doi:10.1142/S0217751X17300241`.

[39] U. W. Heinz and M. Jacob. Evidence for a new state of matter: An Assessment of the results from the CERN lead beam program. Jan 2000.

[40] B. I. Abelev et al. Enhanced strange baryon production in Au+Au collisions compared to p+p at $\sqrt{s_{NN}} = 200$ GeV. *Phys. Rev. C*, 77(4):044908, Apr 2008. `doi:10.1103/physrevc.77.044908`.

[41] E. Andersen et al. Strangeness enhancement at mid-rapidity in Pb+Pb collisions at 158 AGeV/c. *Phys. Lett. B*, 449:401, 1999. `doi:10.1016/S0370-2693(99)00140-9`.

[42] F. Antinori et al. Hyperon yields in Pb+Pb collisions from NA57 experiment. *Nucl. Phys. A*, 715:140, 2003. `doi:10.1016/S0375-9474(02)01422-7`.

[43] J. Adam et al. Enhanced production of multi-strange hadrons in high-multiplicity proton–proton collisions. *Nat. Phys.*, 13(6):535, Apr 2017. `doi:10.1038/nphys4111`.

[44] V. Khachatryan et al. Charged-particle nuclear modification factors in PbPb and pPb collisions at $\sqrt{s_{NN}} = 5.02$ TeV. *J. High Energy Phys.*, 2017(4):39, Apr 2017. `doi:10.1007/J.HighEnergyPhys.04(2017)039`.

[45] B. Abelev et al. Transverse Momentum Distribution and Nuclear Modification Factor of Charged Particles in p+Pb Collisions at $\sqrt{s_{NN}} = 5.02$ TeV. *Phys. Rev. Lett.*, 110(8):082302, Feb 2013. `doi:10.1103/physrevlett.110.082302`.

[46] R. Snellings. Elliptic flow: a brief review. *New J. Phys.*, 13(5):055008, May 2011. `doi:10.1088/1367-2630/13/5/055008`.

[47] A. Bilandzic. *Anisotropic flow measurements in ALICE at the large hadron collider*. PhD thesis, Utrecht U., 2012.

[48] A. M. Poskanzer and S. A. Voloshin. Methods for analyzing anisotropic flow in relativistic nuclear collisions. *Phys. Rev. C*, 58(3):1671, Sep 1998. `doi:10.1103/physrevc.58.1671`.

[49] P. F. Kolb and U. W. Heinz. Hydrodynamic description of ultrarelativistic heavy ion collisions. page 634, May 2003. `arXiv:nucl-th/0305084`.

[50] B. V. Jacak and B. Muller. The exploration of hot nuclear matter. *Science*, 337:310, 2012. `doi:10.1126/science.1215901`.

[51] Md. Nasim et al. Energy dependence of elliptic flow from heavy-ion collision models. *Phys. Rev. C*, 82(5):054908, November 2010. `doi:10.1103/physrevc.82.054908`.

[52] A. Adare et al. Scaling properties of azimuthal anisotropy in Au+Au and Cu+Cu collisions at $\sqrt{s_{NN}} = 200$ GeV. *Phys. Rev. Lett.*, 98:162301, 2007. `doi:10.1103/PhysRevLett.98.162301`.

[53] B. B. Abelev et al. Elliptic flow of identified hadrons in Pb-Pb collisions at $\sqrt{s_{NN}} = 2.76$ TeV. *J. High Energy Phys.*, 06:190, 2015. `doi:10.1007/J.HighEnergyPhys.06(2015)190`.

[54] G. Eyyubova et al. Jets and decays of resonances: Two mechanisms responsible for reduction of elliptic flow at the CERN Large Hadron Collider (LHC) and restoration of constituent quark scaling. *Phys. Rev. C*, 80(6), Dec 2009. `doi:10.1103/physrevc.80.064907`.

[55] S. A. Voloshin. Anisotropic flow at RHIC: constituent quark scaling. *J. Phys. Conf. Ser.*, 9:276, Jan 2005. `doi:10.1088/1742-6596/9/1/052`.

[56] V. Khachatryan et al. Evidence for collectivity in pp collisions at the LHC. *Phys. Lett. B*, 765:193, Feb 2017. `doi:10.1016/j.physletb.2016.12.009`.

[57] V. Khachatryan et al. Long-range two-particle correlations of strange hadrons with charged particles in pPb and PbPb collisions at LHC energies. *Phys. Lett. B*, 742:200, 2015. `doi:10.1016/j.physletb.2015.01.034`.

[58] H. Niemi et al. Influence of a temperature-dependent shear viscosity on the azimuthal asymmetries of transverse momentum spectra in ultrarelativistic heavy-ion collisions. *Phys. Rev. C*, 86:014909, Jul 2012. `doi:10.1103/physrevc.86.014909`.

[59] P. K. Kovtun et al. Viscosity in strongly interacting quantum field theories from black hole physics. *Phys. Rev. Lett.*, 94(11):111601, Mar 2005. `doi:10.1103/physrevlett.94.111601`.

[60] C. Gale et al. Event-by-Event Anisotropic Flow in Heavy-ion Collisions from Combined Yang-Mills and Viscous Fluid Dynamics. *Phys. Rev. Lett.*, 110(1):012302, Jan 2013. `doi:10.1103/physrevlett.110.012302`.

[61] M. Haas et al. Gluon spectral functions and transport coefficients in yang-mills theory. *Phys. Rev. D*, 90(9):091501, Nov 2014. `doi:10.1103/physrevd.90.091501`.

[62] M. Dobbs and J. B. Hansen. The HepMC C++ Monte Carlo event record for High Energy Physics. *Comput. Phys. Commun.*, 134:41, 2001. `doi:10.1016/S0010-4655(00)00189-2`.

[63] Yu. L. Dokshitzer and D. E. Kharzeev. Heavy-quark colorimetry of QCD matter. *Phys. Lett. B*, 519(3-4):199, Nov 2001. `doi:10.1016/s0370-2693(01)01130-3`.

[64] A. Adare et al. Suppression pattern of neutral pions at high transverse momentum in Au+Au collisions at $\sqrt{s_{\mathrm{NN}}} = 200$ GeV and constraints on medium transport coefficients. *Phys. Rev. Lett.*, 101:232301, 2008. `doi:10.1103/PhysRevLett.101.232301`.

[65] A. Adare et al. Inclusive cross-section and double helicity asymmetry for π^0 production in p+p collisions at $\sqrt{s} = 200$ GeV: Implications for the polarized gluon distribution in the proton. *Phys. Rev. D*, 76:051106, 2007. `doi:10.1103/PhysRevD.76.051106`.

[66] J. Adams et al. Evidence from d+Au measurements for final state suppression of high p_T hadrons in Au+Au collisions at RHIC. *Phys. Rev. Lett.*, 91:072304, 2003. `doi:10.1103/PhysRevLett.91.072304`.

[67] W. Li. Collective flow from aa, pa to pp collisions – toward a unified paradigm. *Nucl. Phys. A*, 967:59, 2017. `doi:https://doi.org/10.1016/j.nuclphysa.2017.05.011`.

[68] S. Chatrchyan et al. Studies of azimuthal dihadron correlations in ultra-central PbPb collisions at $\sqrt{s_{\mathrm{NN}}} =$ 2.76 TeV. *J. High Energy Phys.*, 2014(2):88, Feb 2014. `doi:10.1007/J.HighEnergyPhys.02(2014)088`.

[69] G. Aad et al. Observation of Long-Range Elliptic Azimuthal Anisotropies in $\sqrt{s} = 13$ and 2.76 TeV pp Collisions with the ATLAS Detector. *Phys. Rev. Lett.*, 116(17):172301, Apr 2016. `doi:10.1103/physrevlett.116.172301`.

[70] G. Aad et al. Observation of Associated Near-Side and Away-Side Long-Range Correlations in $\sqrt{s_{\mathrm{NN}}} = 5.02$ TeV Proton-Lead Collisions with the ATLAS Detector. *Phys. Rev. Lett.*, 110(18):182302, May 2013. `doi:10.1103/physrevlett.110.182302`.

[71] S. Chatrchyan et al. Centrality dependence of dihadron correlations and azimuthal anisotropy harmonics in PbPb collisions at $\sqrt{s_{\mathrm{NN}}} = 2.76$ TeV. *Eur. Phys. J. C*, 72(5), May 2012. `doi:10.1140/epjc/s10052-012-2012-3`.

[72] M. Aaboud et al. Measurement of the nuclear modification factor for inclusive jets in Pb+Pb collisions at $\sqrt{s_{\mathrm{NN}}} = 5.02$ TeV with the ATLAS detector. *Phys. Lett. B*, 790:108–128, Mar 2019. `doi:10.1016/j.physletb.2018.10.076`.

[73] B. Trzeciak. Quenching of heavy and light flavour jets: Experimental overview. Quark Matter 2019, 2019. URL: `https://indi.to/ZZ5bs`.

[74] T. Matsui and H. Satz. J/ψ Suppression by Quark-Gluon Plasma Formation. *Phys. Lett. B*, 178:416, 1986. `doi:10.1016/0370-2693(86)91404-8`.

[75] H. Satz. Colour deconfinement and quarkonium binding. *J. Phys. G: Nucl. Part. Phys.*, 32(3):R25, Feb 2006. `doi:10.1088/0954-3899/32/3/R01`.

[76] S. Digal et al. Quarkonium feed down and sequential suppression. *Phys. Rev. D*, 64:094015, 2001. `doi:10.1103/PhysRevD.64.094015`.

[77] L. Kluberg and H. Satz. *Color Deconfinement and Charmonium Production in Nuclear Collisions*. 2010. `doi:10.1007/978-3-642-01539-7_13`.

[78] A. M. Sirunyan et al. Measurement of nuclear modification factors of $\Upsilon(1S)$, $\Upsilon(2S)$, and $\Upsilon(3S)$ mesons in PbPb collisions at $\sqrt{s_{\mathrm{NN}}} = 5.02$ TeV. *Phys. Lett. B*, 790:270, Mar 2019. `doi:10.1016/j.physletb.2019.01.006`.

[79] J. Adam et al. Measurement of inclusive J/ψ suppression in Au+Au collisions at $sqrts_{\mathrm{NN}} = 200$ GeV through the dimuon channel at STAR. *Phys. Lett. B*, 797:134917, Oct 2019. `doi:10.1016/j.physletb.2019.134917`.

[80] P. Faccioli et al. Study of ψ' and χ_c decays as feed-down sources of J/ψ hadroproduction. *J. High Energy Phys.*, 10:004, 2008. `doi:10.1088/1126-6708/2008/10/004`.

[81] K. A. Olive et al. Review of Particle Physics. *Chin. Phys. C*, 38:090001, 2014. `doi:10.1088/1674-1137/38/9/090001`.

[82] A. Andronic et al. Heavy-flavour and quarkonium production in the LHC era: from proton–proton to heavy-ion collisions. *Eur. Phys. J. C*, 76(3):107, 2016. `doi:10.1140/epjc/s10052-015-3819-5`.

[83] K. J. Eskola et al. EPS09: A New Generation of NLO and LO Nuclear Parton Distribution Functions. *J. High Energy Phys.*, 04:065, 2009. `doi:10.1088/1126-6708/2009/04/065`.

[84] A. H. Rezaeian and Z. Lu. Cronin effect for protons and pions in high-energy pA collisions. *Nucl. Phys. A*, 826:198, 2009. `doi:10.1016/j.nuclphysa.2009.05.073`.

[85] R. Wang et al. Global study of nuclear modifications on parton distribution functions. *Nucl. Phys. B*, 920:1, 2017. `doi:10.1016/j.nuclphysb.2017.04.008`.

[86] J. P. Blaizot et al. High-energy pA collisions in the color glass condensate approach. 1. Gluon production and the Cronin effect. *Nucl. Phys. A*, 743:13, 2004. `doi:10.1016/j.nuclphysa.2004.07.005`.

[87] R. Vogt. Cold Nuclear Matter Effects on Open and Hidden Heavy Flavor Production at the LHC. In *7th International Workshop on Charm Physics*, 8 2015.

[88] I. P. Lokhtin et al. Heavy ion event generator hydjet++ (HYDrodynamics plus JETs). *Comput. Phys. Commun.*, 180(5):779, May 2009. `doi:10.1016/j.cpc.2008.11.015`.

[89] R. Brun and F. Rademakers. Root - an object oriented data analysis framework. URL: `http://root.cern.ch/`.

[90] T. Sjöstrand et al. Pythia 6.4 physics and manual. *J. High Energy Phys.*, 2006(05):26, May 2006. `doi:10.1088/1126-6708/2006/05/026`.

[91] R. Baier et al. Angular dependence of the radiative gluon spectrum and the energy loss of hard jets in QCD media. *Phys. Rev. C*, 60(6):064902, Nov 1999. `doi:10.1103/physrevc.60.064902`.

[92] R. Baier et al. Angular dependence of the radiative gluon spectrum. *Phys. Rev. C*, 64(5):057902, Oct 2001. `doi:10.1103/physrevc.64.057902`.

[93] M. Gyulassy and X. Wang. Multiple collisions and induced gluon bremsstrahlung in QCD. *Nucl. Phys. B*, 420(3):583, Jun 1994. `doi:10.1016/0550-3213(94)90079-5`.

[94] L. D. Landau and I. Pomeranchuk. Limits of applicability of the theory of bremsstrahlung electrons and pair production at high-energies. *Dokl. Akad. Nauk Ser. Fiz.*, 92:535, 1953.

[95] A. B. Migdal. Bremsstrahlung and pair production in condensed media at high energies. *Phys. Rev.*, 103:1811,1820, Sep 1956. `doi:10.1103/PhysRev.103.1811`.

[96] J. D. Bjorken. Highly Relativistic Nucleus-Nucleus Collisions: The Central Rapidity Region. *Phys. Rev. D*, 27:140, 1983. `doi:10.1103/PhysRevD.27.140`.

[97] I. P. Lokhtin and A. M. Snigirev. Angular structure of energy losses of hard jet in dense QCD-matter. *Phys. Lett. B*, 440(1-2):163, Nov 1998. `doi:10.1016/s0370-2693(98)01089-2`.

[98] I. P. Lokhtin. Pyquen event generator. URL: http://cern.ch/lokhtin/pyquen.

[99] B. Andersson. *The Lund model*, volume 7. Cambridge University Press, 7 2005.

[100] K. Tywoniuk et al. Gluon shadowing in the Glauber–Gribov model at HERA. *Phys. Lett. B*, 657(4-5):170, Dec 2007. doi:10.1016/j.physletb.2007.09.065.

[101] E. Braaten and M. H. Thoma. Energy loss of a heavy fermion in a hot QED plasma. *Phys. Rev. D*, 44:1298–1310, Aug 1991. doi:10.1103/PhysRevD.44.1298.

[102] I. P. Lokhtin and A. M. Snigirev. Nuclear geometry of jet quenching. *Eur. Phys. J. C*, 16(3):527, Sep 2000. doi:10.1007/s100520000437.

[103] N. S. Amelin et al. Fast hadron freeze-out generator. *Phys. Rev. C*, 74(6), Dec 2006. doi:10.1103/physrevc.74.064901.

[104] N. S. Amelin et al. Fast hadron freeze-out generator. ii. noncentral collisions. *Phys. Rev. C*, 77:014903, Jan 2008. doi:10.1103/PhysRevC.77.014903.

[105] F. Retière and M. A. Lisa. Observable implications of geometrical and dynamical aspects of freeze-out in heavy ion collisions. *Phys. Rev. C*, 70(4), Oct 2004. doi:10.1103/physrevc.70.044907.

[106] J. Rafelski. Strange anti-baryons from quark - gluon plasma. *Phys. Lett. B*, 262:333, 1991. doi:10.1016/0370-2693(91)91576-H.

[107] G. D Yen et al. Excluded volume hadron gas model for particle number ratios in A+A collisions. *Phys. Rev. C*, 56(4):2210, Oct 1997. doi:10.1103/physrevc.56.2210.

[108] S. R. De Groot. *Relativistic Kinetic Theory. Principles and Applications*. 1980.

[109] Yu. M. Sinyukov et al. The Analysis Of Hadron Matter Properties In Heavy Ion Collisions. *Nukleonika*, 43(3):369, 1998.

[110] L. V. Bravina et al. Dynamical vs. geometric anisotropy in relativistic heavy-ion collisions: Which one prevails? *Eur. Phys. J. A*, 53(11), Nov 2017. doi:10.1140/epja/i2017-12420-5.

[111] U. A. Wiedemann. Two-particle interferometry for noncentral heavy-ion collisions. *Phys. Rev. C*, 57(1):266, Jan 1998. doi:10.1103/physrevc.57.266.

[112] A. Andronic et al. Statistical hadronization of charm in heavy-ion collisions at SPS, RHIC and LHC. *Phys. Lett. B*, 571(1-2):36, Oct 2003. doi:10.1016/j.physletb.2003.07.066.

[113] J. von Neumann. Various Techniques Used in Connection with Random Digits. In *Monte Carlo Method*, volume 12 of *National Bureau of Standards Applied Mathematics Series*, chapter 13, page 36. US Government Printing Office, Washington, DC, 1951.

[114] G. Torrieri et al. SHARE: Statistical hadronization with resonances. *Comput. Phys. Commun.*, 167(3):229, May 2005. `doi:10.1016/j.cpc.2005.01.004`.

[115] I. P. Lokhtin et al. Hadron spectra, flow and correlations in pbpb collisions at the LHC: interplay between soft and hard physics. *Eur. Phys. J. C*, 72(6), Jun 2012. `doi:10.1140/epjc/s10052-012-2045-7`.

[116] J. Crkovská et al. Influence of jets and decays of resonances on the triangular flow in ultrarelativistic heavy-ion collisions. *Phys. Rev. C*, 95(1), Jan 2017. `doi:10.1103/physrevc.95.014910`.

[117] L. V. Bravina et al. Higher harmonics of azimuthal anisotropy in relativistic heavy-ion collisions in HYDJET++ model. *Eur. Phys. J. C*, 74(3), Mar 2014. `doi:10.1140/epjc/s10052-014-2807-5`.

[118] L. V. Bravina et al. Hexagonal flow v_6 as a superposition of elliptic v_2 and triangular v_3 flows. *Phys. Rev. C*, 89(2), Feb 2014. `doi:10.1103/physrevc.89.024909`.

[119] G. Eyyubova et al. Angular dihadron correlations as an interplay between elliptic and triangular flows. *Phys. Rev. C*, 91(6), Jun 2015. `doi:10.1103/physrevc.91.064907`.

[120] I. P. Lokhtin et al. On the possibility of thermalization of heavy mesons in ultrarelativistic nuclear collisions. *J. Exp. Theor. Phys.*, 124(2):244, Feb 2017. `doi:10.1134/S1063776117010149`.

[121] E. E. Zabrodin et al. Mechanisms of Forward–Backward Correlations in the Multiplicity of Particles in Ultrarelativistic Heavy-Ion Collisions. *J. Exp. Theor. Phys.*, 130(5):660, May 2020. `doi:10.1134/S1063776120040093`.

[122] I. P. Lokhtin and A. A. Sidorova. Mechanisms of B Meson Suppression in Ultrarelativistic Heavy Ion Collisions. *J. Exp. Theor. Phys.*, 128(4):586–591, 2019. `doi:10.1134/S1063776119020225`.

[123] N. S. Geraksiev. The Nuclotron-based Ion Collider Facility Project. The Physics Programme for the Multi-Purpose Detector. *J. Phys. Conf. Ser.*, 1023(1):012030, 2018. `doi:10.1088/1742-6596/1023/1/012030`.

[124] A. V. Belyaev et al. 12 years of HYDJET++ generator: history and the latest results. *J. Phys. Conf. Ser.*, 1690(1):012117, 2020. `doi:10.1088/1742-6596/1690/1/012117`.

[125] I. Lokhtin. HYDJET++ event generator. URL: `http://lokhtin.web.cern.ch/lokhtin/hydjet++/`.

[126] UNINETT Sigma2. The Norwegian e-infrastructure for Research and Education. URL: https://www.sigma2.no/.

[127] I. P. Lokhtin et al. Modeling the jet quenching, thermal resonance production and hydrodynamical flow in relativistic heavy ion collisions. *J. Phys. Conf. Ser.*, 270:012060, Jan 2011. `doi:10.1088/1742-6596/270/1/012060`.

[128] J. Adams et al. Transverse-Momentum and Collision-Energy Dependence of High-pT Hadron Suppression in Au+Au Collisions at Ultrarelativistic Energies. *Phys. Rev. Lett.*, 91(17), Oct 2003. `doi:10.1103/physrevlett.91.172302`.

[129] I. G. Bearden et al. Pseudorapidity distributions of charged particles from Au+Au collisions at the maximum RHIC energy. *Phys. Rev. Lett.*, 88:202301, 2002. `doi:10.1103/PhysRevLett.88.202301`.

[130] A. Adare et al. Systematic Study of Azimuthal Anisotropy in Cu+Cu and Au+Au Collisions at $\sqrt{s_{NN}} = 62.4$ and 200 GeV. *Phys. Rev. C*, 92(3):034913, 2015. `doi:10.1103/PhysRevC.92.034913`.

[131] L. Adamczyk et al. Observation of D^0 Meson Nuclear Modifications in Au+Au Collisions at $\sqrt{s_{NN}} = 200$ GeV. *Phys. Rev. Lett.*, 113(14), Sep 2014. `doi:10.1103/physrevlett.113.142301`.

[132] J. Adam et al. Centrality and transverse momentum dependence of D^0 meson production at mid-rapidity in Au+Au collisions at $\sqrt{s_{NN}} = 200$ GeV. *Phys. Rev. C*, 99(3):034908, 2019. `doi:10.1103/PhysRevC.99.034908`.

[133] A. Adare et al. J/ψ Production vs Centrality, Transverse Momentum, and Rapidity in Au+Au Collisions at $\sqrt{s_{NN}} = 200$ GeV. *Phys. Rev. Lett.*, 98:232301, 2007. `doi:10.1103/PhysRevLett.98.232301`.

[134] L. Adamczyk et al. Measurement of D^0 Azimuthal Anisotropy at Midrapidity in Au+Au Collisions at $\sqrt{s_{NN}}$=200 GeV. *Phys. Rev. Lett.*, 118(21):212301, 2017. `doi:10.1103/PhysRevLett.118.212301`.

[135] I. P. Lokhtin et al. Charmed meson and charmonium production in PbPb collisions at the LHC. *J. Phys. G: Nucl. Part. Phys.*, 43(12):125104, Nov 2016. `doi:10.1088/0954-3899/43/12/125104`.

[136] B. Abelev et al. Centrality dependence of π, K, p production in Pb-Pb collisions at $\sqrt{s_{NN}} = 2.76$ TeV. *Phys. Rev. C*, 88:044910, 2013. `doi:10.1103/PhysRevC.88.044910`.

[137] G. Aad et al. Measurement of the azimuthal anisotropy for charged particle production in $\sqrt{s_{NN}} = 2.76$ TeV lead-lead collisions with the ATLAS detector. *Phys. Rev. C*, 86:014907, 2012. `doi:10.1103/PhysRevC.86.014907`.

[138] J. Adam et al. Transverse momentum dependence of D-meson production in Pb-Pb collisions at $\sqrt{s_{NN}} = 2.76$ TeV. *J. High Energy Phys.*, 03:081, 2016. `doi:10.1007/J.HighEnergyPhys.03(2016)081`.

[139] B. B. Abelev et al. Azimuthal anisotropy of D meson production in Pb-Pb collisions at $\sqrt{s_{\mathrm{NN}}}$ = 2.76 TeV. *Phys. Rev. C*, 90(3):034904, 2014. `doi: 10.1103/PhysRevC.90.034904`.

[140] J. Adam et al. Differential studies of inclusive J/ψ and ψ(2S) production at forward rapidity in Pb-Pb collisions at $\sqrt{s_{\mathrm{NN}}}$ = 2.76 TeV. *J. High Energy Phys.*, 05:179, 2016. `doi:10.1007/J.HighEnergyPhys.05(2016)179`.

[141] E. Abbas et al. J/ψ Elliptic Flow in Pb-Pb Collisions at $\sqrt{s_{\mathrm{NN}}}$ = 2.76 TeV. *Phys. Rev. Lett.*, 111:162301, 2013. `doi:10.1103/PhysRevLett.111.162301`.

[142] N. Borghini and J.-Y. Ollitrault. Momentum spectra, anisotropic flow, and ideal fluids. *Phys. Lett. B*, 642(3):227, Nov 2006. `doi:10.1016/j.physletb.2006.09.062`.

[143] S. Acharya et al. Transverse momentum spectra and nuclear modification factors of charged particles in pp, p-Pb and Pb-Pb collisions at the LHC. *J. High Energy Phys.*, 11:013, 2018. `doi:10.1007/J.HighEnergyPhys.11(2018)013`.

[144] M. Aaboud et al. Measurement of the azimuthal anisotropy of charged particles produced in $\sqrt{s_{\mathrm{NN}}}$ = 5.02 TeV Pb+Pb collisions with the ATLAS detector. *Eur. Phys. J. C*, 78(12):997, 2018. `doi:10.1140/epjc/s10052-018-6468-7`.

[145] S. Acharya et al. Measurement of D^0, D^+, D^{*+} and D_s^+ production in Pb-Pb collisions at $\sqrt{s_{\mathrm{NN}}}$ = 5.02 TeV. *J. High Energy Phys.*, 10:174, 2018. `doi: 10.1007/J.HighEnergyPhys.10(2018)174`.

[146] M. Cacciari et al. Theoretical predictions for charm and bottom production at the LHC. *J. High Energy Phys.*, 2012(10), Oct 2012. `doi:10.1007/J.HighEnergyPhys.10(2012)137`.

[147] M. Cacciari et al. Gluon PDF constraints from the ratio of forward heavy quark production at the LHC at $\sqrt{S}$ = 7 and 13 TeV, 2015. `arXiv:1507.06197`.

[148] M. Cacciari et al. The p_T spectrum in heavy-flavour hadroproduction. *J. High Energy Phys.*, 1998(05):007, May 1998. `doi:10.1088/1126-6708/1998/05/007`.

[149] M. Cacciari et al. The p_t spectrum in heavy-flavour photoproduction. *J. High Energy Phys.*, 2001(03):006, Mar 2001. `doi:10.1088/1126-6708/2001/03/006`.

[150] A. M. Sirunyan et al. Measurement of prompt D^0 meson azimuthal anisotropy in Pb-Pb collisions at $\sqrt{s_{NN}}$ = 5.02 TeV. *Phys. Rev. Lett.*, 120(20):202301, 2018. `doi:10.1103/PhysRevLett.120.202301`.

[151] S. Acharya et al. Studies of J/ψ production at forward rapidity in Pb–Pb collisions at $\sqrt{s_{\mathrm{NN}}}$ = 5.02 TeV. *J. High Energy Phys.*, 2020(2):41, Feb 2020. `doi:10.1007/J.HighEnergyPhys.02(2020)041`.

[152] S. Acharya et al. J/ψ elliptic and triangular flow in Pb-Pb collisions at $\sqrt{s_{\mathrm{NN}}}$ = 5.02 TeV. *J. High Energy Phys.*, 2020(10), Oct 2020. `doi:10.1007/J.HighEnergyPhys.10(2020)141`.

[153] ALICE Collaboration. Centrality determination in heavy ion collisions. Technical Report ALICE-PUBLIC-2018-011, Aug 2018.

[154] J. Adam et al. J/ψ suppression at forward rapidity in Pb-Pb collisions at $\sqrt{s_{\mathrm{NN}}} = \mathbf{5.02}$ TeV. *Phys. Lett. B*, 766:212, 2017. `doi:10.1016/j.physletb.2016.12.064`.

[155] J. Adam et al. Centrality dependence of the pseudorapidity density distribution for charged particles in Pb–Pb collisions at $\sqrt{s_{\mathrm{NN}}}$=5.02 TeV. *Phys. Lett. B*, 772:567, Sep 2017. `doi:10.1016/j.physletb.2017.07.017`.

Appendices

Appendix A

Au+Au at $\sqrt{s_{\mathrm{NN}}} = 200$ GeV

$\sqrt{s_{\mathrm{NN}}} = 200$ GeV

particle	distribution	γ_c	$N_{ev} \times 10^3$	centrality	figure
$h^\pm$	$dN/dp_T, dN/d\eta$	-1	800	0-20%	4.1
	v_2 HYDJET++ 2.4	-1	100	0-40%	4.2
	v_2 HYDJET++ 2.1	-1	54	0-20%	4.3
$D, J/\psi$	$dN/dp_T, v_2, R_{AA}$	7	450	0-40%	4.4, 4.5
	$dN/dp_T, R_{AA}$	6	80	0-40%	4.6
	$dN/dp_T, R_{AA}$	5	60	0-40%	4.7
	$dN/dp_T, R_{AA}$	4	250	0-40%	4.8

Table A.1: Summary of the number of simulated events, N_{ev}, in the used centrality bins for all the studied distributions in Au+Au collisions at $\sqrt{s_{\mathrm{NN}}} = 200$ GeV. Corresponding figures are listed too.

Appendix B

Pb+Pb at $\sqrt{s_{\text{NN}}} = 2.76$ TeV

$\sqrt{s_{\text{NN}}} = 2.76$ TeV				
particle	distribution	$N_{ev} \times 10^3$	centrality	figure
$h^{\pm}, D$	$dN/dp_T, v_n$	1 232	0-50%	B.1, B.2, B.3, 4.12, 4.13, 4.14, 4.15
J/ψ	$dN/dp_T, v_2$	435	0-50%	4.16, 4.17

Table B.1: Summary of the number of simulated events, N_{ev}, in the used centrality bins for all the studied distributions in Pb+Pb collisions at $\sqrt{s_{\text{NN}}} = 2.76$ TeV. Corresponding figures are listed too.
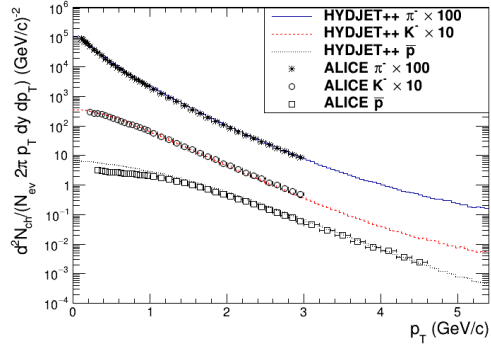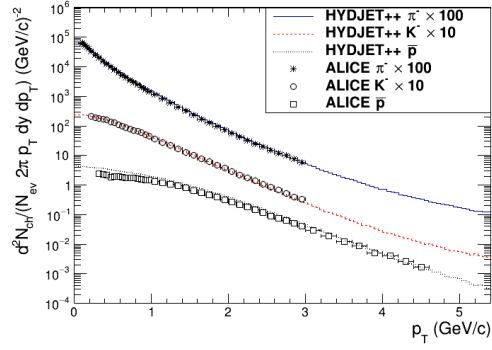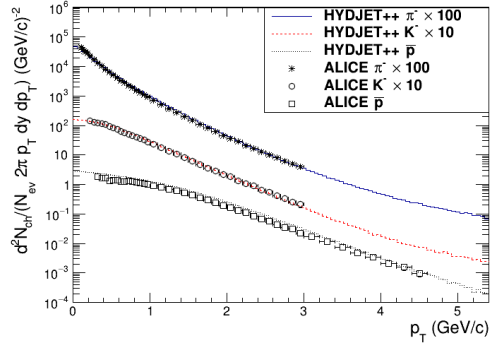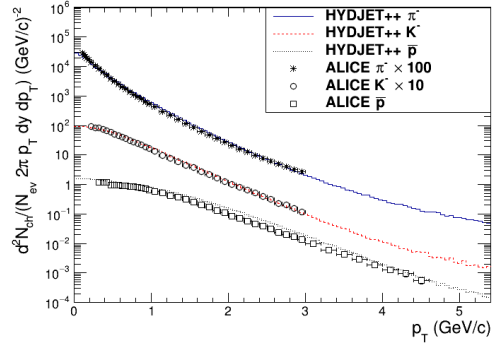
Figure B.1: THIS WORK: Comparison of the HYDJET++ π^-, K^- and antiproton $\bar{p}$ transverse momentum p_T histograms for the Pb+Pb collisions at $\sqrt{s_{\mathrm{NN}}} = 2.76$ TeV with the ALICE experimental data [136] in four centrality bins.
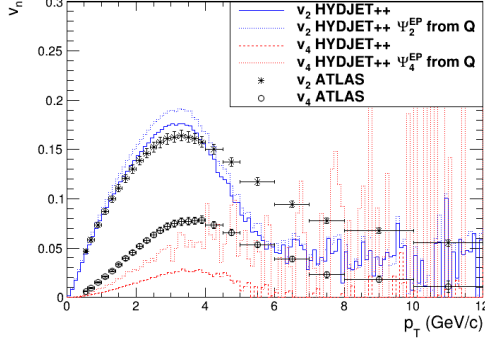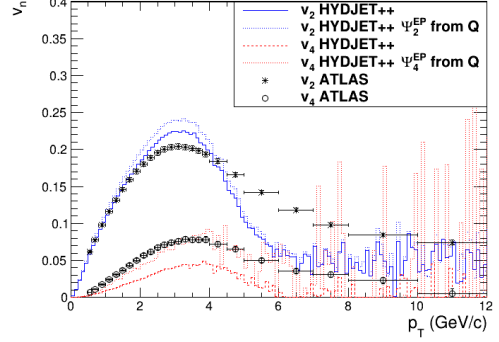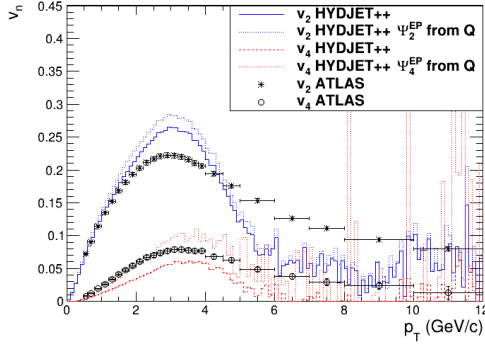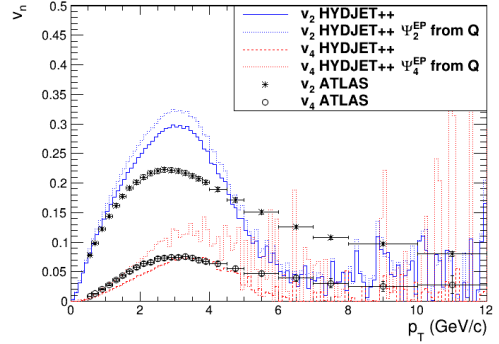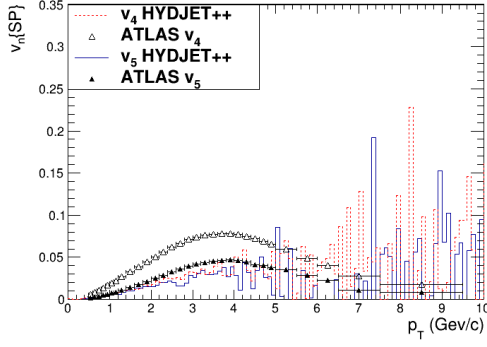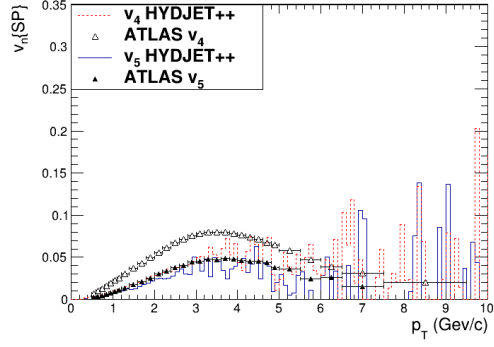
Figure B.2: THIS WORK: Comparison of the HYDJET++ simulated flow coefficients v_2, v_4 p_T distribution histograms of all the charged hadrons $h^{\pm}$ for the Pb+Pb collisions at $\sqrt{s_{\mathrm{NN}}} = 2.76$ TeV with the ATLAS experimental data [137] in four centrality bins. Computation has been done with respect to the HYDJET++ true reaction plane (solid and dashed lines) and with respect to the estimated reaction plane from the event plane using $\vec{Q}_n$ (dotted lines).
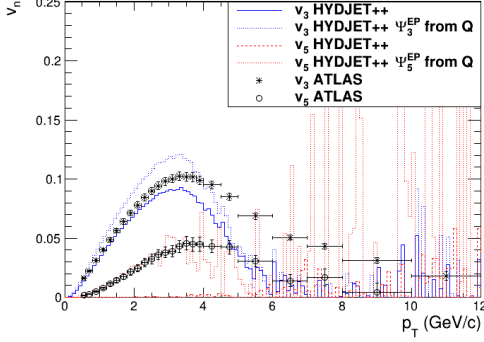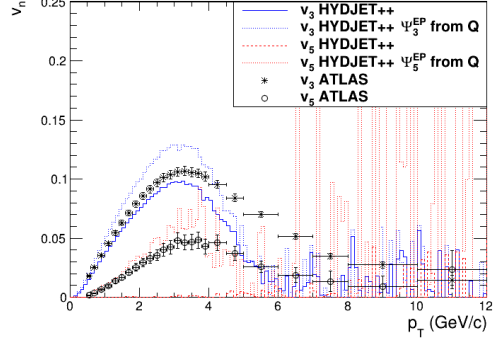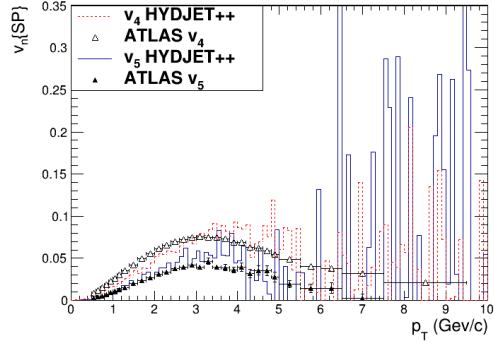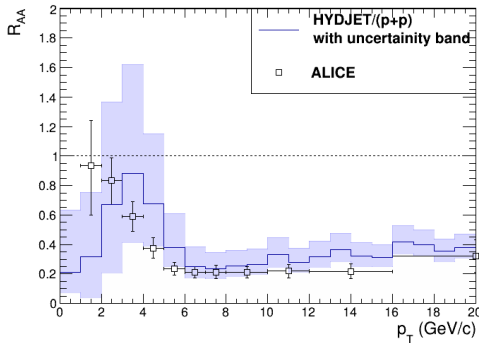
Figure B.3: THIS WORK: Comparison of the HYDJET++ simulated flow coefficients v_3, v_5 p_T distribution histograms of all the charged hadrons $h^\pm$ for the Pb+Pb collisions at $\sqrt{s_{\mathrm{NN}}} = 2.76$ TeV with the ATLAS experimental data [137] in four centrality bins. Computation has been done with respect to the HYDJET++ true reaction plane (solid and dashed lines) and with respect to the estimated reaction plane from the event plane using $\vec{Q}_n$ (dotted lines).

Appendix C

Pb+Pb at $\sqrt{s_{\mathrm{NN}}} = 5.02$ TeV

$\sqrt{s_{\mathrm{NN}}} = 5.02$ TeV

particle	distribution	ρ_{max}	$N_{ev} \times 10^3$	centrality	figure
$h^{\pm}, D$	$dN/dp_T, dN/d\eta,$ v_n, R_{AA}	1.35	473	0-50%	4.18, 4.19, 4.20, C.1, C.2, C.3, 4.21, 4.22, C.4, C.5, C.6
J/ψ	$dN/dp_T, v_n$	0.6	530	0-10%	4.23, 4.24, 4.26, 4.25
	dN/dp_T	0.6	720	10-30%	4.28, 4.27, 4.28, C.7, C.8
	R_{AA}	0.6	770	0-20%	4.29
	$dN/dp_T, v_n$	0.67	1600	0-20%	4.30, 4.26, 4.27
	$dN/dp_T, v_n$	0.67	700	20-30%	4.31 left, 4.27
	R_{AA}	0.67	320	0-20%	4.31 right
	dN/dp_T	0.65	380	0-20%	4.24, 4.25, C.7, C.8
	dN/dp_T	0.66	200	0-20%	4.24, 4.25, C.7, C.8
	dN/dp_T	0.67	240	0-20%	4.24, 4.25, C.7, C.8
	dN/dp_T	0.7	240	0-20%	4.24, 4.25, C.7, C.8

Table C.1: Summary of the number of simulated events, N_{ev}, in the used centrality bins for all the studied distributions in Pb+Pb collisions at $\sqrt{s_{\mathrm{NN}}} = 5.02$ TeV. Corresponding figures are listed too.
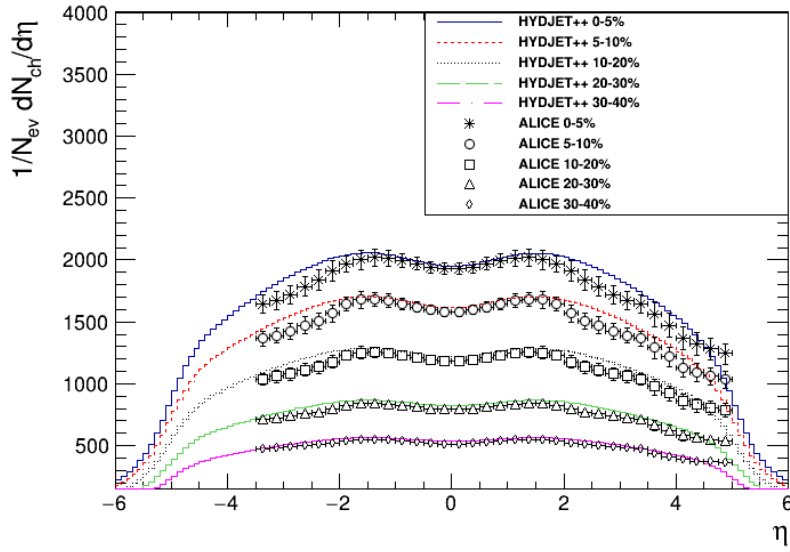
Figure C.1: THIS WORK: Comparison of the HYDJET++ η distribution histograms of all the charged hadrons $h^{\pm}$ for Pb+Pb collisions at $\sqrt{s_{\mathrm{NN}}} = 5.02$ TeV with the ALICE experimental data [155] in 0-5%, 5-10%, 10-20%, 20-30%, 30-40% centrality bins.
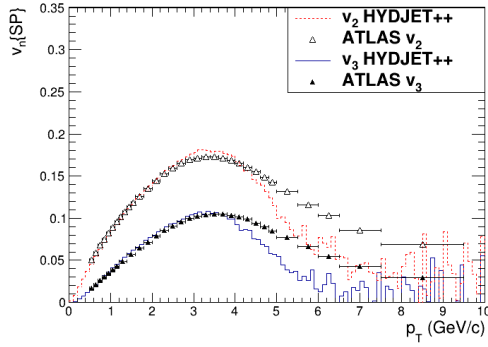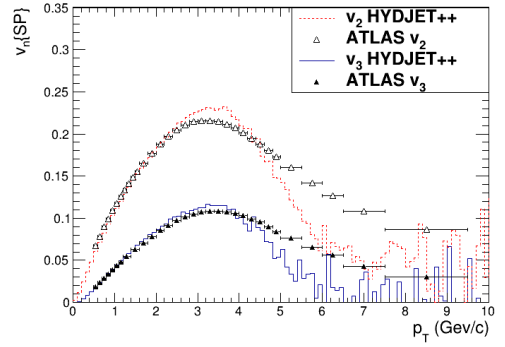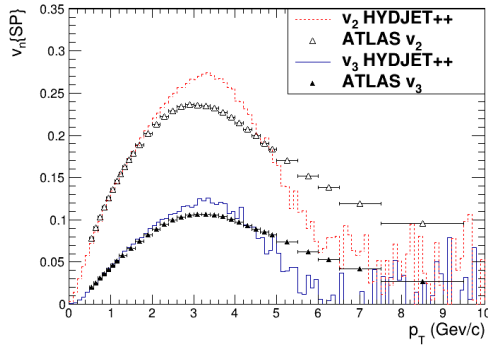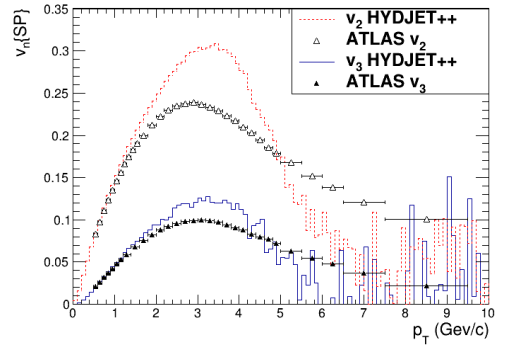
Figure C.2: THIS WORK: Comparison of the HYDJET++ simulated flow coefficients v_2, v_3 p_T distribution histograms of all charged hadrons $h^\pm$ for Pb+Pb collisions at $\sqrt{s_{\mathrm{NN}}} = 5.02$ TeV with ATLAS experimental data [144] in four centrality bins. Pseudorapidity $|\eta| < 2.5$ cut has been applied and computation has been done by the scalar product method.
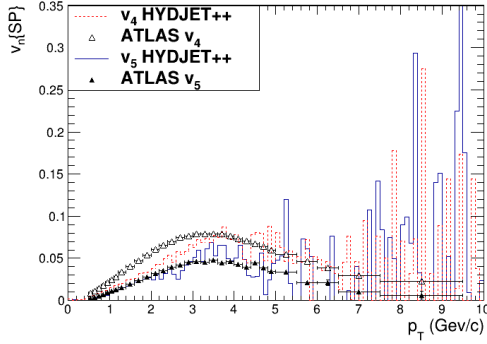
Figure C.3: THIS WORK: Comparison of the HYDJET++ simulated flow coefficients v_4, v_5 p_T distribution histograms of all charged hadrons $h^\pm$ for Pb+Pb collisions at $\sqrt{s_{NN}} = 5.02$ TeV with ATLAS experimental data [144] in four centrality bins. Pseudorapidity $|\eta| < 2.5$ cut has been applied and computation has been done by the scalar product method.

Figure C.4: THIS WORK: Comparison of the D^0 nuclear modification factor R_{AA} computed from the HYDJET++ simulation to the ALICE experimental data R_{AA} [145] in Pb+Pb collisions at $\sqrt{s_{NN}} = 5.02$ TeV in 0-10% (left) and 30-50% (right) centrality regions. Rapidity cut $|y| < 0.5$ has been applied.

106

D$^+$, 0-10%, |y|<0.5, Pb+Pb@$\sqrt{s_{NN}}$=5.02 TeV
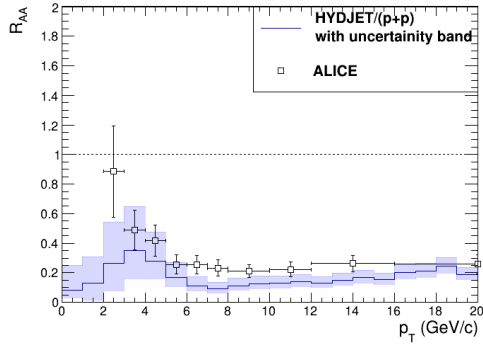
D$^+$, 30-50%, |y|<0.5, Pb+Pb@ $\sqrt{s_{NN}}$=5.02 TeV
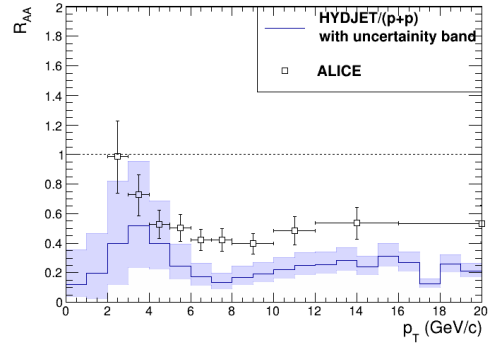
Figure C.5: THIS WORK: Comparison of the D^+ nuclear modification factor R_{AA} computed from the HYDJET++ simulation to the ALICE experimental data R_{AA} [145] in Pb+Pb collisions at $\sqrt{s_{\mathrm{NN}}} = 5.02$ TeV in 0-10% (left) and 30-50% (right) centrality regions. Rapidity cut $|y| < 0.5$ has been applied.
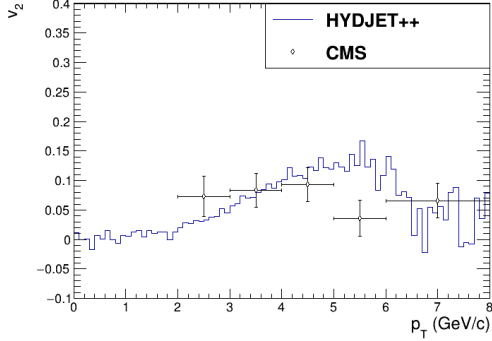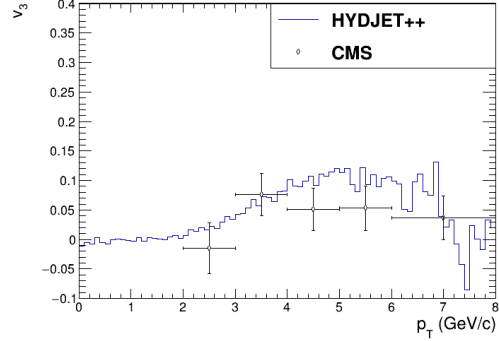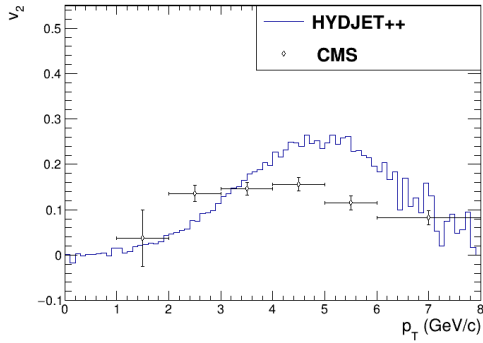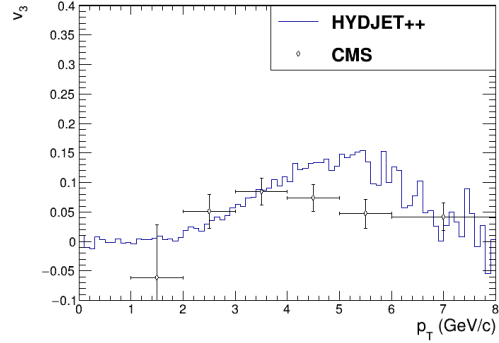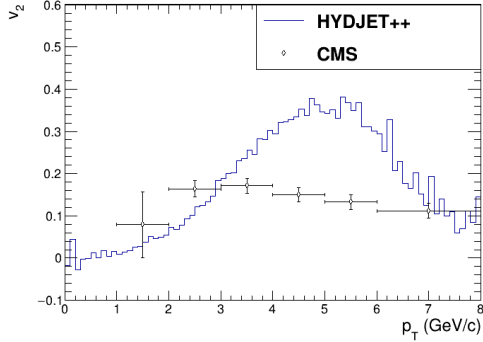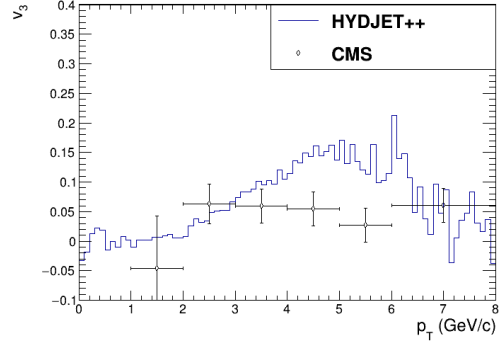
Figure C.6: THIS WORK: Comparison of the HYDJET++ simulated elliptic v_2 (left column) and triangular (right column) flow p_T distribution histograms of the D^0 mesons for Pb+Pb collisions at $\sqrt{s_{\mathrm{NN}}} = 5.02$ TeV to the CMS experimental data [150] in three centrality bins. Computation has been done with respect to the HYDJET++ true reaction plane.
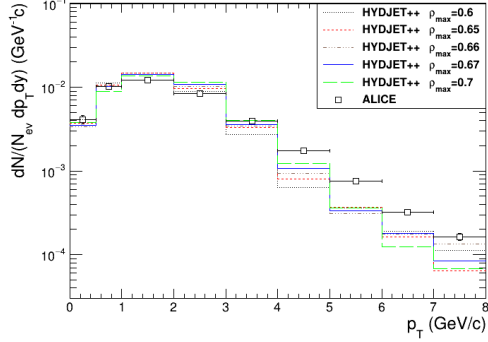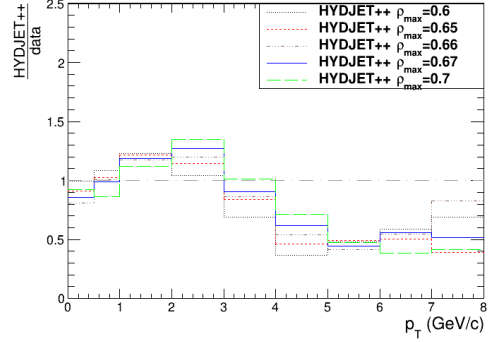
Figure C.7: THIS WORK: Comparison of the HYDJET++ simulated p_T distribution histograms of J/ψ meson yield to the ALICE experimental data [151] in Pb+Pb collisions at $\sqrt{s_{\mathrm{NN}}} = 5.02$ TeV in the 10-20% centrality region. Histograms for different ρ_{max} values are shown. In the right graph relative difference between the model and the data is studied.
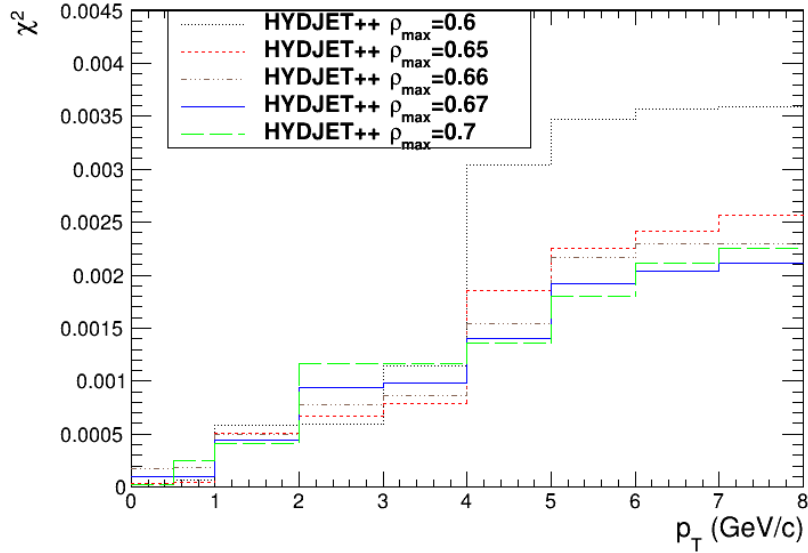

Figure C.8: THIS WORK: Precision evaluation of the HYDJET++ simulation with five different ρ_{max} values in Pb+Pb collisions at $\sqrt{s_{\mathrm{NN}}} = 5.02$ TeV in the 10-20% centrality region using χ^2 distribution.